Theses and Dissertations

12-2012

Modeling, Fabrication and Characterization of Scalable Electroless Gold Plated Nanostructures for Enhanced Surface Plasmon Resonance

Gyoung Gug Jang
University of Arkansas, Fayetteville

Modeling, Fabrication and Characterization of Scalable Electroless Gold Plated

Nanostructures for Enhanced Surface Plasmon Resonance

Modeling, Fabrication and Characterization of Scalable Electroless Gold Plated Nanostructures

for Enhanced Surface Plasmon Resonance

A dissertation submitted in partial fulfillment
of the requirements for the degree of
Doctor of Philosophy in Chemical Engineering

By

Gyoung Gug Jang

Seoul National University
Bachelor of Science in Natural Fiber, 2002
Seoul National University
Master of Science in Natural Fiber Science, 2004

December 2012
University of Arkansas

ABSTRACT

The scientific and industrial demand for controllable thin gold (Au) film and Au nanostructures is increasing in many fields including opto-electronics, photovoltaics, MEMS devices, diagnostics, bio-molecular sensors, spectro-/microscopic surfaces and probes. In this study, a novel continuous flow electroless (CF-EL) Au plating method is developed to fabricate uniform Au thin films in ambient condition. The enhanced local mass transfer rate and continuous deposition resulting from CF-EL plating improved physical uniformity of deposited Au films and thermally transformed nanoparticles (NPs). Au films and NPs exhibited improved optical photoluminescence (PL) and surface plasmon resonance (SPR), respectively, relative to batch immersion EL (BI-EL) plating. Suggested mass transfer models of Au mole deposition are consistent with optical feature of CF-EL and BI-EL films.

The prototype CF-EL plating system is upgraded an automated scalable CF-EL plating system with real-time transmission UV-vis (T-UV) spectroscopy which provides the advantage of CF-EL plating, such as more uniform surface morphology, and overcomes the disadvantages of conventional EL plating, such as no continuous process and low deposition rate, using continuous process and controllable deposition rate. Throughout this work, dynamic morphological and chemical transitions during redox-driven self-assembly of Ag and Au film on silica surfaces under kinetic and equilibrium conditions are distinguished by correlating real-time T-UV spectroscopy with X-ray photoelectron spectroscopy (XPS) and scanning electron microscopy (SEM) measurements. The characterization suggests that four previously unrecognized time-dependent physicochemical regimes occur during consecutive EL deposition of silver (Ag) and Au onto tin-sensitized silica surfaces: self-limiting Ag activation; transitory

Ag NP formation; transitional Au-Ag alloy formation during galvanic replacement of Ag by Au; and uniform morphology formation under controlled hydraulic conditions.

A method to achieve the time-resolved optical profile of EL Au plating was devised and provided a new transitional EL Au film growth model which validated mass transfer model prediction of the deposited thickness of ≤100 nm thin films. As a part of the project, validation of mass transfer model, a spectrophotometric method for quantitative analysis of metal ion is developed that improves the limit of detection comparable to conventional instrumental analysis.

The present work suggests that modeling, fabrication and characterization of this novel CF-EL plating method is performed to achieve an ultimate purpose: developing a reliable, inexpensive wet chemical process for controlled metal thin film and nanostructure fabrication.

This dissertation is approved for recommendation to the Graduate Council.

Dissertation Director:

_____
Dr. Donald Keith Roper

Dissertation Committee:

_____
Dr. Bob Beitle

_____
Dr. Shannon L. Servoss

_____
Dr. Rick Ulrich

_____
Dr. Surendra P. Singh

DISSERTATION DUPLICATION RELEASE

I hereby authorize the University of Arkansas Libraries to duplicate this dissertation when needed for research and/or scholarship.

Agreed

Gyoung Gug Jang

Refused

Gyoung Gug Jang

ACKNOWLEDGMENTS

I would like to give my thanks to all those who have encouraged and assisted me in this work. Without their kind support, I could not complete this work. First, I would like to thank my advisor, Dr. Donald Keith Roper for his wise advising and infinite help during my graduate work. I also thank my committee members, Dr. Bob Beitle, Dr. Shannon L. Servoss, Dr. Rick Ulrich, and Dr. Surendar Singh for their participation and support of my work.

I was happy to work with our group members, Dr. Wonmi Ahn, Phillip Blake, Aaron Russell, Braden Harbin, Laura Velasco and Drew Dejarnette. I have learned a lot of academic and technical knowledge while working with them.

Lastly, I dedicate this dissertation to my wife, Hyun-Ju Lee. Over the past eight years, she has been my mental mentor and unconditional supporter. I would not be where I am without her.

TABLE OF CONTENTS

LIST OF FIGURES

Figure 3.5. The automated CF-EL Au plating system with real-time T-UV spectroscopy. The upper diagram represents the cycle of EL plating with real-time monitoring. Inset is the cross section of flow cell with spectra system.

Figure 4.1.1. Microscopic/spectroscopic comparison between CF-EL nanostructure, A, and BI-EL, B. A, B and A', B' are AFM and SEM images, respectively. Cross-sectional diagram below AFM image represent the roughness of both films. The NPs in A' and B' are thermally transformed from deposited film structure. Insets are transmission (film) and extinction (NP) spectra.

Figure 4.1.2. Distributions of NP diameters acquired from SEM images of Au films annealed at 350˚C for 3hr, followed by annealing at 800˚C for 30 min. (A) Shows BI-EL 1 min, BI-EL 2 min, BI-EL 4 min, and CF-EL 800 (2+1 min) (B) Shows Ahn[19] (2 min), BI-EL 6 min and CF-EL 1000 (2+1 min).

Figure 4.1.3. Variation of optical features – PH (A,D), λ_{max} (B,E), and FWHM (C,F) -- with increasing time-integrated mass transport coefficient (M_{Au} /$A\varDelta C_{Au}$) from T-UV of thin Au films (A,B,C) and thermally-transformed Au NP (D,E,F). Data are for BI-EL (open squares), CF-EL (solid triangles) and Ahn[19] (open circle). Lines show linear least squares fit to BI-EL data. . The least squares fit for Fig 4.1.3.B excludes the BI-EL 1 min data point for λ_{max} which is not clearly distinguishable.

Figure 4.2.1. The basic procedure of determination of Au(I) content in TMB aqueous solution at high and low molar ratio of reductant HCHO and oxidant NBS. Au reducing reagent (AuRR) is a mixture of HCHO and Na_2SO_3.

Figure 4.2.2. The Au(I) is quantitatively detected by effect of TMB oxidation in various mole ratios of HCHO/NBS and its association with Au(I). The error bars represent the standard deviation of peak variation (n=8) after mixing from 30 min to 60 min. The inset figures are suggested mechanisms of Au(I) detection in the matrix of Au, HCHO, NBS (SucBr) and TMB. (Solid blue diamond, solid green triangle and solid red circle represent each calibration curves in Figure 2)

Figure 4.2.3. Balancing reduction potential improves the LOD of Au(I) determination. Comparison of calibration curves between Au(III) reference experimental result and re-oxidized Au(III) are well matched. The two Au(I) determination at low reluctant levels exhibit improved accuracy for detecting Au(I). The trend lines in inset are in the range of 0.00 - 0.1 mgL^{-1}

Figure 4.3.1. Real-time spectra monitored from Sn sensitization, through Ag activation, to Au reducing agent (HCHO) treatment at 3 ml/hr. (A) Ag reduction for 2 min (i.e. between 60 s and180 s), (B) HCHO reductant exposure for 23 sec (i.e. between 308 s and 331 s) (C) HCHO

reductant exposure for additional 2 min (i.e. between 331 s and 490 s) (4) Corresponding kinetic profile of % transmission at 425 nm (the Ag LSPR feature). Colored arrowheads on (D) shown when each spectra in (A-C) were taken.

Figure 4.3.2. SEM images of wideband light exposure effect to HCHO treated Ag film on silicate substrate: (A) dark condition (B) continuous light exposure.

Figure 4.3.3. (A) Time resolved transmission spectra during a whole procedure of CF-EL Au deposition; Sn sensitization, Ag activation, galvanic replacement of Ag by Au, and Au film growth. The Ag spectral transmission was captured after 2 min CF deposition. The Au plating was performed at a flowrate of 3 ml/hr for 5 min. (B) Blow-up of spectra for 0-70 sec (C) Corresponding plasmon peaks (Ag Valley, Au PL) shift and peak height profile during EL Au deposition. Optical feature may represent physical transitions: Ag NP formation (I), Au/Ag alloy formation (II), Au film formation (III), and uniform Au film growth (IV)

Figure 4.3.4. The XPS depth profiles of CF-3-10 for main chemical components: (A) Au4f7; (B) Ag3d; (C) Sn3d; (D) Si2p

Figure 4.3.5. Quantitative chemical component characterization of XPS depth profile of two different CF and BI deposited film for 5 and 10 min. Target chemical components are C1s, O1s, Ag3d, Au4f7, Sn3d3 and Si2P.

Figure 4.3.6. The physicochemical procedure of CF-EL Au deposition on silicate substrate: Sn sensitization, Ag activation on Sn, galvanic displacement of Ag by Au, Au film growth. Star marks(*) indicate revealed transitional physicochemical reactions from this work.

Figure 4.4.1. Cross-sectional SEM image of wide flow channel CF-EL films (CF$_w$) deposited with increasing flowrates from 2 mL/hr to 5 mL/hr for 10 min. (A) CFw-2-10, (B) CFw-3-10, (C) CFw-4-10, (D) CFw-5-10.

Figure 4.4.2. Measured (data points) and predicted (lines; film theory) thickness profile of EL Au deposition. (A) CF-EL deposited films with varying Reynolds numbers. (B) Comparison between BI and CF EL deposited films with varying time. The prediction was calculated based on a flowrate of 3 mL/hr and the flow cell dimension (0.08 x 0.2 x 3.2 cm^3)

Figure 4.4.3. Kinetic profiles of real-time Ag LSPR and Au PL transmission feature at 425 and 495 nm for CF and BI-EL Au deposition. Inset are transmission CF-EL spectra taken at times indicated by the black arrows in the main figure. Dotted and solid lines in inset identify 425 nm and 495 nm wavelength from which profiles in the main figure were derived. SEM images show representative EL metal film morphologies during three steps in EL Au plating: I. Ag cluster deposited film (-10 sec); II. HCHO-driven Ag NP formation (27 sec); III. EL Au deposited film (670 sec))

LIST OF TABLE

LIST OF ABBREVIATIONS

AFM	Atomic force microscopy
BI-EL	Batch immersion electroless
CF-EL	Continuous flow electroless
CVD	Chemical vapor deposition
D^3-H_2O	Distilled, deionized, degassed water
EBL	Electron beam lithography
EL	Electroless
EM	Electromagnetic
FWHM	Full width at half maximum
HCHO	Formaldehyde
ITO	Indium-tin-oxide
LOD	limit of detection
LSPR	Localized surface plasmon resonance
NBS	*N*-bromosuccinimide
NIR	Near infrared
NP	Nanoparticle
PL	Photoluminescence
PH	Peak height
PVD	Physical vapor deposition
QCM	Quartz crystal microbalance
SEM	Scanning electron microscopy
SPR	Surface plasmon resonance
TMB	3,3',5,5'-tetramethylbenzidine dihydrochloride

T-UV	transmission UV-vis
XPS	X-ray photoelectron spectroscopy
2D	Two dimensional

LIST OF SYMBOLS

A	Area of substrate [m^2]
A_c	Cross sectional area of flow channel [m^2]
a	finite half thickness of a parallelepiped medium
b	width [cm]
c_{As}	Concentration at the surface [$kmol/m^3$]
c_{A0}	Concentration in the bulk solution [$kmol/m^3$]
$\bar{c}_{Ax}$	the average concentration at a distance x along the flow channel [$kmol/m^3$]
ΔC	Concentration difference between metal ion in bulk solution and at the surface of substrate [g/m^3]
D_{AB}	Diffusivity of A ions in an B aqueous solution [m^2/s]
d_H	hydraulic diameter
h	flow thickness [cm]
F	Operational flow rate [cm^3/s]
L	Length of flow channel [cm]
k_f	Mass transfer rate at the surface [m/s]
k_m	Forward and reverse mass transfer rate from the outer compartment [m/s]
k_r	Mass transfer rate from the inner compartment [m/s]
M_A	Total number of transferred solute ions [kmol]
n_A	Instantaneous rate of molar transfer [kmol/s]

N	Number of immersion onto an open substrate
N_{Re}	Reynolds number
N_{sc}	Schmidt number
N_{sh}	Sherwood number
ρ	Density
t	Elapsed time [s]
w	Width of a confined cell [cm]
γ	Wall shear rate
ζ'	Composition based on Au_5Sn
δ	Composition AuSn

CHAPTER ORGANIZATION

This dissertation consists of five chapters. The first chapter introduces an overview of plasmonic metal nanostructure using conventional deposition and electroless plating. It discusses the overall goals and objectives of the project. In chapter two, the modeling of electroless Au deposition is described to provide unsteady (batch immersion) and steady flow enhanced (continuous flow) metal ion diffusion features during thin film formation. Several mass transfer models are suggested to predict the deposited amount and thickness. Chapter three highlights the fabrication of surface plasmon resonance (SPR) enhanced Au nanostructures via continuous flow (CF-EL) plating. Thin film, thermal transformed nanoparticle (NP) and regular NP array are fabricated by CF-EL plating and electron beam lithography. In Chapter four, four important characteristic achievement are described; 4.1 Characterization of uniformity enhanced EL Au film, 4.2 Quantitative detection of Au(I) concentration for EL Au deposition, 4.3 Metal disposition and dynamics during EL metal thin film synthesis, 4.4 Prediction of EL Au deposition on silicate surface at unsteady and steady condition. Chapter five concludes the dissertation and proposes suggestions and plans for future work.

OVERALL INTRODUCTION

Predictable deposition of uniform metal thin films with consistent physical and chemical features at ever-decreasing scales is vital in microelectronics, photovoltaics, photocatalytic coatings, and spectroscopic platforms. A desire to improve control over the kinetic and equilibrium processes governing the nanoscale structure of as-deposited film motivates improved understanding of film growth mechanisms at the atomic scale. Metal thin film deposition in aqueous solution by electroless (EL) plating has been utilized to fabricate microelectrodes, and electronics, catalyst because of the simplicity and utility of the operation. Although it requires no external source of current and no sophisticated equipment, EL plating can provide uniform surface coverage on multidimensional surfaces without the directional limitations encountered during sputtering or evaporation. But while kinetics and thermodynamics of metal thin film growth via vapor phase have been extensively studied as instrumental technologies which control extreme conditions (e.g. vacuum and high temperature) have advanced, the study of metal ion diffusion during thin film formation in aqueous phase has not been investigated from an atom-scale perspective since the 1990s due to diminished industrial and scientific demand resulting from limited scalability of bench bath systems. In particular, a fundamental mechanism describing EL metal thin film growth that allows its control at the nano-scale, including consideration of internal and interfacial substrate-film structures, remains underdeveloped due to a lack of time-resolved data collection and corresponding structural characterization.

Due to extensive demand for thin film applications in photovoltaic devices, photocatalytic coating, fuel cells, batteries, and electronics, "top-down" physical vapor deposition, chemical vapor deposition, and vacuum evaporation are being rapidly advanced to meet stringent requirements for more sophisticated engineered nano–and micro-structures.

However, top–down technologies are limited by essentially one–dimensional deposition, which prevents their application in structures that require uniform, multi-dimensional thin metal film formation such as through–holes for 3D integrated circuits and probe tip coatings. Top down deposition does not form stable, uniformly deposited ultrathin film structures on non–conductive substrates due to lattice mismatch between deposited metal and substrate. Recently EL gold (Au) deposition has been shown to overcome many limitations of conventional vapor deposition methods by allowing fabrication of size controllable Au nanoparticles (NPs) on nonconductive glass substrates, deposition on optical capillary internal walls, more uniform thin film and NPs, uniform spheroid Au NP arrays with and without thermal annealing, Au coated nanorods and 1–D nanostructure in porous templates. EL deposition of Au occurs through galvanic displacement of Ag which has been reduced onto tin (Sn)–sensitized ceramic or polymer substrates. Controlling kinetics of galvanic replacement reaction of Ag by Au allow synthesis of optically unique bimetallic nanostructure.

Metal thin film formation by physical vapor deposition has been described mechanistically as adsorption and diffusion of adatoms in non-equilibrium steps of nucleation, coalescence, and subsequent thickness growth driven by an external electron donor. Descriptive kinetic models illustrate deposition behavior at conditions of high gas pressure and temperature Due to atomic scale control of thin film microstructure and industrial demands for lowering processing temperature, vapor deposition often produce polycrystalline thin films. Polycrystalline film structure has been correlated to deposition parameters using temperature-dependent structure zone models. In-situ time-resolved micrographs corroborate kinetic simulations and corresponding film growth models. As a representative "bottom-up" method, electroplating is a well characterized method; however it usually produces non-uniform metal

thin films which are dependent on substrate geometry and plating conditions and requires conductive substrates such as Au, Ag, Cu, nickel, carbon steel and indium-tin-oxide. General reaction rate models for electroplating systems use current density to predict the final film thickness. However, it is difficult to control deposition rates for nano-scale deposition and uniform thin film coatings on three dimensional substrates due to edge effects, current variations associated with deposited film thickness, and variations in the electrodes with time.

In contrast to physical vapor deposition and electroplating, EL synthesis of metal films exposes a substrate to a series of solutions containing metal ions that may be covalently bound to the surface or to existing metals via redox reaction without application of external electrical energy. Depending on the source of donated electrons, film formation is mechanistically classified into 1) substrate dehydration and sensitization 2) metal catalyzed reduction 3) galvanic replacement reduction and 4) autocatalytic reduction. However, morphological and chemical transitions that accompany these consecutive mechanisms and their respective contributions to metal thin film growth on silica substrates remain unclear because time-resolved characterization of transitory physicochemical features has not been performed. In particular, the nature of interface between metal film and non-conductive glass substrate remains poorly characterized. Moreover, the kinetics of thin film growth and physicochemical transitions via reduction are still not well understood due to a lack of time-resolved characterization of the heterogeneous redox reactions involved. EL Au films grow via a complicated, multistep redox process influenced by metallic complexes and reductant ion diffusion to catalytic surfaces and subsequent reaction on these surfaces. Improved understanding of fundamentals of each of these influences in EL Au plating could allow prediction and control of EL Au plating and improve resulting physical and optical film characteristics.

Recently, an equilibrium metal deposition system referred to as continuous flow EL (CF–EL) Au plating was developed. This system allowed control of metal film growth rate at steady deposition conditions with a constant equilibrium driving force. CF-EL plating differs from metal deposition by conventional batch immersion EL processes in which a transient, decreasing thermodynamic force drives metal ions dissolved in a bulk medium to diffuse through a stagnant thin boundary layer toward a substrate onto which deposition occurs. Continuous depletion of metal ions from solution produces a time-dependent molecular diffusive flux. But in CF–EL plating, bulk metal ion solutions at constant composition flow continuously past a substrate, producing a larger, time-invariant metal deposition rate. This rate is due to a higher average steady concentration driving force across a narrower stagnant boundary layer adjacent to the surface. Continuous, enhanced deposition in CF-EL plating has been shown to improve physical uniformity of deposited Au films and thermally transformed NPs. However, EL Au plating is not adequately described by one-dimensional unimolecular diffusion due to the heterogeneous character of four constituent chemical reactions; Sn sensitization, Ag activation on Sn, galvanic displacement of Ag by Au, and Au deposition. Furthermore, few generally applicable or specific standards have been applied to ascribe morphologies (e.g. shape, thickness, continuity, overall uniformity at nanoscale) or chemical composition of EL deposited structures, or to provide control for commercialized continuous operation. Moreover, for EL plating, the rate-limiting step of thickness growth is the subject of controversy, because deposition rates are extremely sensitive to bath composition (including concentration) and operation conditions (temperature, mechanical stirring rate, etc.) Previous reports developing kinetic models for EL Au deposition lacked accompanying experimental validation for prediction of nano-scale thickness growth. Limited recent experiments by us with EL Au plating indicated that modifying mass transfer

rates can improve uniformity and optical properties of thin EL Au film characteristics.

In this work, dynamic physical and chemical disposition of Ag and Au during EL metal thin film growth at equilibrium hydraulic conditions will be evaluated in situ by real-time T-UV spectral measurement, time-resolved scanning electron microscopy (SEM) characterization and X-ray photoelectron spectroscopy (XPS) depth profiling. Such geometric- and dielectric-dependent optical features allow real-time T–UV spectral measurements to provide a fast, effective analytical method to evaluate surface morphology and chemistry during EL deposition of metal thin films. Also, the real-time T-UV spectra measurement correlated with photoluminescence (PL) of EL Au film evaluates the mass deposition rate of Au in EL thin films and validates a diffusion-limited model of mass transfer in EL plating. By performing experiments at constant hydraulic conditions, variations in composition of reagents and reductants are eliminated. Real-time PL and plasmon spectral characterization at constant hydraulic conditions allowed previously unrecognized time-dependent physicochemical transitory regimes of EL Au plating to be identified: self-limited Ag activation; Ag NP formation; Au-Ag alloy formation during galvanic displacement of Ag by Au. It distinguishes particular time frames for each regime, which allows the deposition rate of submicron scale Au thin films to be described using a diffusion-limited model of mass transfer. Use of in situ kinetic, rather than more common equilibrium transmission profiles allows time frames for complex heterogeneous chemical reactions and physical transformation during EL film formation to be distinguished. The description is validated using complementary measures of nanoscale thickness obtained using XPS and SEM. The resulting description for EL deposition allows precise prediction of deposited thickness for nano-scale films (≤ 100 nm) on scalable substrates.

CHAPTER 1

1. Plasmonic metal nanostructure using electroless plating

Plasmonic metal nanostructures such as thin metal films, nanoparticles (NP) and nanorods are important in developing opto-electronics, MEMS devices, photovoltaic solar cells, diagnostics, spectroscopic biosensors, and microscopic surfaces and probes. The advance research of the plasmonic nanostructures requires better control over the precise fabrication to maximize the interaction between photon and electron in less than 100 nm scales. Thus, understanding the fundamentals of metal deposition in atomic view is one of most essential steps to manipulate the precise structural dimensions. Also, classifying advantage and disadvantage of conventional fabrication methods is necessary to either optimize these processes for specific nanostructures such as NP arrays or develop a novel instrument. This chapter is organized as follows: Section 1.1 describes fundamental optical features of plasmonic structures such as thin film, a NP and ordered NP arrays as application of plasmonics. Section 1.2 summarizes conventional top-down and bottom-up fabrication methods for plasmonic metal structures with describing growth mechanism. Section 1.3 identifies present advantage and disadvantage of conventional fabrication method. Section 1.4 lists the motivation and objectives of the present work.

1.1 Fundamentals of plasmonic nanostructure

1.1.1 Surface plasmon resonance (SPR)

SPR is the coherent excitation of conduction electrons at the interface of a metal and a dielectric substrate caused by incident, resonant light in planar surface. Surface plasmons, or surface plasmon polaritons, are collective charge density oscillations that propagate in a direction parallel to the metal/dielectric interface when light is reflected at the metal interface under

resonant conditions.[1] Figure 1.1 shows a schematic of the SPR phenomenon in Au thin film. When a *p*-polarized incident light beam propagates through a higher refractive index medium (n_1) and meets an interface at a medium of lower refractive index (n_2), the incident light is totally reflected at the interface and, then, propagated back into the high refractive index medium. The evanescent field wave, E, decays exponentially from the interface.

However, when a thin noble metal layer with suitable thickness (~50 nm) is located between two media, E penetrates the metal layer and excites electromagnetic surface plasmon waves, k_{sp}, that propagate along the metal surface. When E is in resonance with k_{sp}, the surface plasmon wave will create an enhanced evanescent wave, or a surface plasmon. The resonance is a result of energy and momentum being transformed from incident photons into surface plasmons, and is sensitive to the refractive index of the medium on the opposite side of the film from the reflected light. Due to these optical features, SPR has been used to enhance the surface sensitivity of several spectroscopic measurements such as fluorescence, Raman scattering, and second harmonic generation. As their simplest approach, SPR reflectivity measurements are used as a platform of biomolecular sensors. Recent works report that the improved uniformity of deposited nanostructure can enhance SPR and surface enhanced Raman scattering.[2] Especially, uniformity enhanced EL Au films also can be used as the platform.

1.1.2   Localized Surface Plasmon Resonance (LSPR)

LSPRs are charge density oscillations confined to metallic NPs and metallic nanostructures.[3] Figure 1.2. shows the schematic of SPR in a nanosphere[3] and experimental spectra of LSPR from a random Au NP array. When resonant light irradiates a metallic NP, the conduction electrons in electron field excite and oscillate coherently due to displacement of
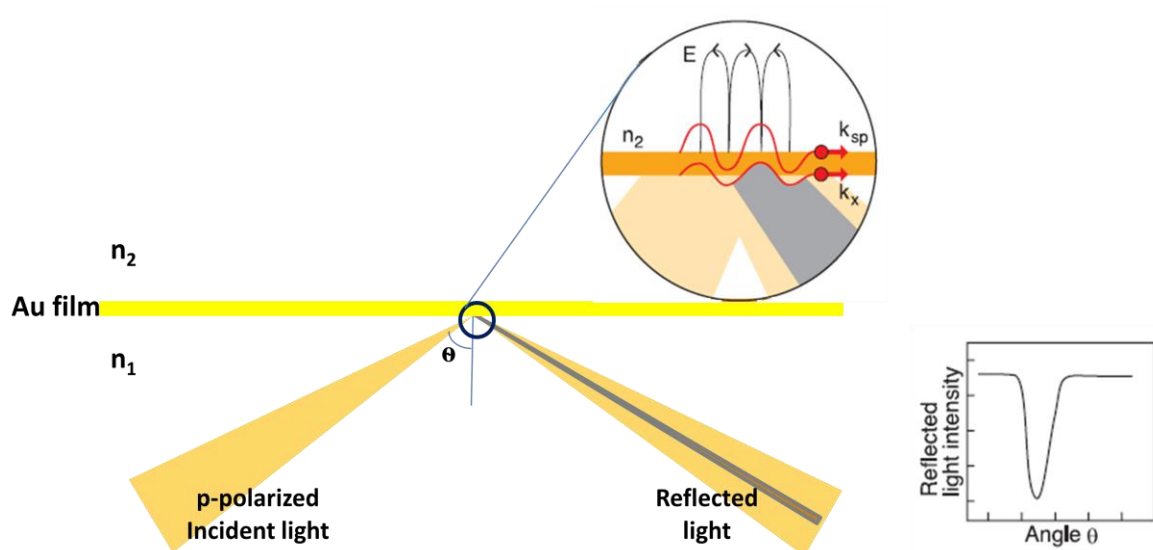
Figure 1.1. The mechanism of surface plasmon resonance in Au thin film.[1]
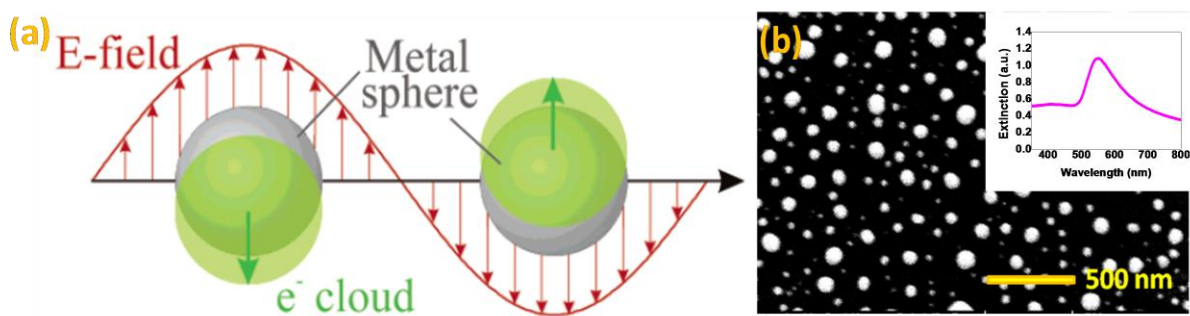
Figure 1.2. (a) Schematics of localized surface plasmon oscillation (adopted from Schatz[3]) (b) SEM image of thermally transformed NPs from EL Au film, Inset is extinction spectra of Au NP.

electron cloud and its restoring force. The resonance effect results in strong light scattering, the appearance of intense surface plasmon absorption bands, and an enhancement of the local electromagnetic fields. The optical features of the surface plasmon absorption band such as frequency, absorption maxima, and intensity are characteristic of the type of material and structural features such as the size, size distribution and shape of NPs. Also, the optical response is a strong function of the surrounding environments.

1.1.3 Enhanced synchronous SPR

Due to synchronous plasmon-photon coupling between scattering light and excited plasmon on NPs,[4,5] two dimensional (2D) regular NP arrays are important in bio-molecular sensing devices using surface enhanced Raman scattering[3] and LSPR,[6] integrated circuit waveguides,[7] photovoltatics,[8] and antennas. Particularly, tuning wavelength of SPR peak into the near infrared (NIR), around 650 - 900 nm, has drawn attention to improve detection efficiency of optical sensor because low scattering and absorption from intrinsic chromophore exhibit the highest tissue transmissivity in the NIR.[9]

The optical responses, intensity and wavelength, are tuned by adjusting particle size, shape, and inter-particle spacing between NPs in a 2D lattice. For example, Figure 1.3. shows how the electromagnetic coupling peak that originates from orientation of particles with respect to incident electromagnetic excitation is shifted by varying the interparticle spacing in a 2D square NP array.[5] But tuning the wavelength by adjusting particle size, shape, or inter-particle spacing requires expensive and laborious fabrication. Additionally, as shown in the Figure 1.3, only a specific geometry of array exhibits the highest optical sensitivity, higher peak height and narrower full-width half maxima (FWHM) at the specific wavelength. Tuning the wavelength to other target frequency requires attenuated peak feature due to dispersion.[5]
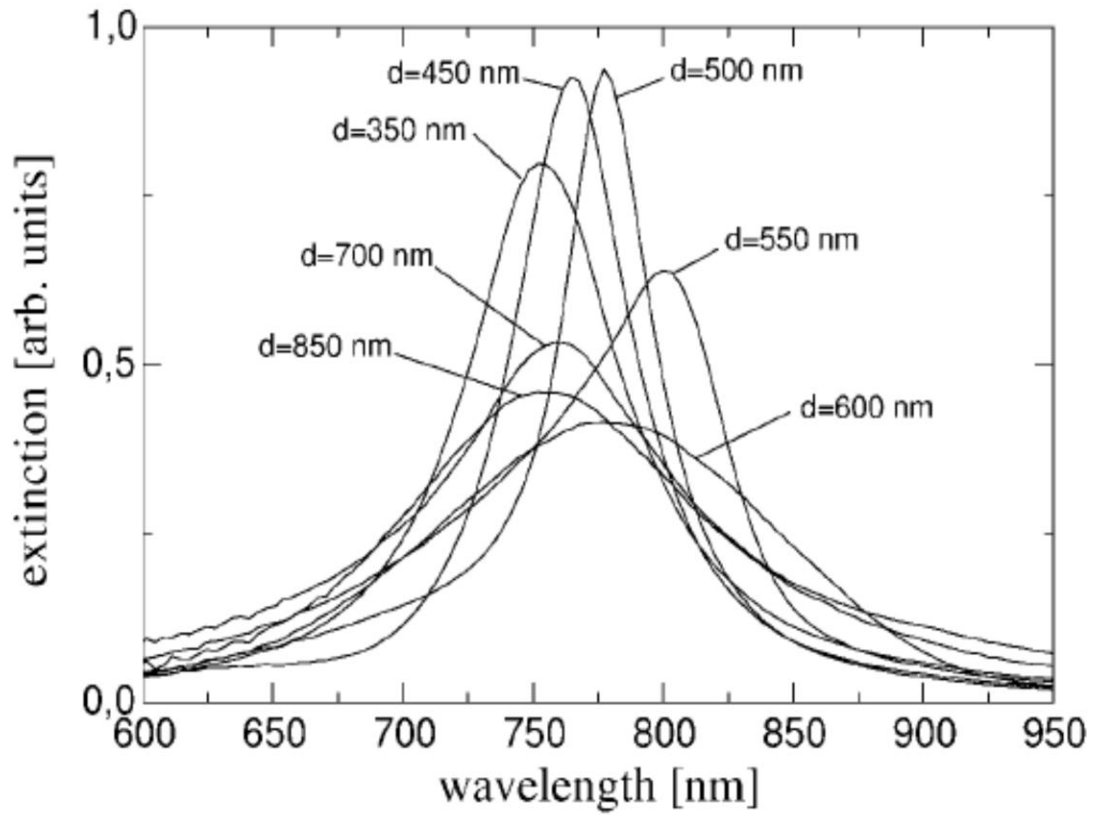
Figure 1.3. Extinction spectra for square 2D grating of Au NPs on an ITO coated quartz substrate (d ; grating constant) (Adopted from Lamprecht[5])

1.2　Conventional Fabrication Methods for Au nanostructures

1.2.1　Top-down metal thin film deposition

Metal thin films and nanostructures are generally fabricated by physical vapor deposition (PVD), vacuum evaporation,[10] sputtering,[11] and chemical vapor deposition (CVD)[12]. These top-down approaches have been successfully used to fabricate metal thin films on an industrial scale with a standardized characterization method for thickness. For example, quartz crystal microbalances (QCM) have been incorporated into sputtering instrumentation to determine specific thickness of deposited thin films.[13]

The mechanism of metal thin film formation by PVD was generally described as adsorption and diffusion of adatoms in an extremely non-equilibrium process starting with nucleation, coalescence, and subsequent thickness growth with external electron donor.[14] The descriptive kinetic models illustrate the deposition behavior in high gas pressure and temperature condition.[15] Due to atomic scale control of thin film microstructure and industrial demands for lowering processing temperature, vapor deposition often produces polycrystalline thin films. Thus, extensive studies have been carried out to define the correlation between polycrystalline film structure and deposition parameters using temperature dependent structure zone models.[14,15] Especially, recent advanced microscopic characterization validates these film growth models and kinetic simulations comparing with *in-situ* time-resolved micrographs.[15]

1.2.2　Bottom-up metal thin film deposition

Electroplating, also called electrolytic plating, is a representative bottom-up metal deposition using external electrical current to reduce cations of a desired metal from a solution onto conductive substrates.[16] It is similar to a galvanic cell acting in reverse. Two half-cells

(anode and cathode) are immersed in a solution called an electrolyte containing other conductive ions and one or more dissolved metal salts. The cathode is to be plated by the dissolved metal via reduction while the anode is to be plated out with the same rate of plating. It has been used to improve corrosion resistance and coat on various shapes and sizes of substrates. This electroplating is a well characterized method. However it usually produces non-uniform metal thin films depending on substrate geometry and plating condition and needs conductive substrates such as Au, Ag, Cu, nickel, carbon steel and indium-tin-oxide.[16] Furthermore, hazardous plating bath waste is produced. Although general reaction rate models and current density (J) have been used to predict the final film thickness,[17] it is still difficult to control deposition rate and nano-scale deposition.

Electroless (EL) plating is auto-catalytic chemical deposition of a desirable metal from an aqueous solution of a metal salt without external electric current. Before describing the plating, it is necessary to define the terminology "electroless plating" because there are three fundamentally different types of chemical plating performed without supply of an external current source.

(1) Galvanic displacement

Galvanic displacement plating, often called immersion, is the deposition of a more noble metal on a less noble metal substrate without external electron donor.[18] An example is the plating of zinc with copper in an acidified copper sulfate solution. When zinc metal is immersed in the solution, the zinc atoms (less noble) dissolve and are spontaneously replaced by copper atoms from the solution. The two redox reactions can be described as follows:

Oxidation: $Zn^0 \rightarrow Zn^{2+} + 2e^-$ (Anodic) $E^0 = 0.76$ V

Reduction: $Cu^{2+} + 2e^- \rightarrow Cu^0$ (Cathodic) $E^0 = 0.34$ V

Overall reaction: $Zn^0 + Cu^{2+} \rightarrow Zn^{2+} + Cu^0$, E^0=1.1 V
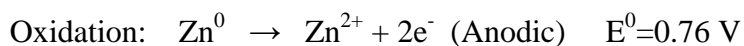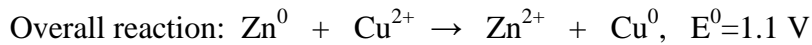
When the entire substrate is fully cover with copper, the displacement effectively ceases and no further thickness increases. Thus, the chemical plating yields deposits limited to a few micron in thickness, usually 1 to 3µm.[18] For gold (Au) plating, the available substrates are silver (Ag), copper, brass, nickel, tin or mild steel. The adhesion is not satisfactory.

(2) Autocatalytic plating

Autocatalytic plating is the desirable metal deposition by the chemical reduction of metallic ions in an aqueous solution containing a reducing agent.[18] Due to the reducing agent, the deposition is controllable to few hundred microns in thickness. The metal salt and reductant usually react in the presence of a catalyst, i.e. the part to be plated. The reductants are hydrazine, sodium hypophosphite, sodium borohydride, amine borane, titanium chloride, and formaldehyde.[19] The available metal salts are nickel, copper, tin (Sn), Ag and Au. The term "electroless plating" only describes the autocatalytic plating.

(3) Substrate-catalyzed processes

The substrate-catalyzed processes are similar to autocatalytic plating because of the presence of reducing agent. Considering the solution composition, it is not possible to distinguish between two processes. Thus, it can be categorized by the material of catalysis. For Au plating, the substrate-catalyzed plating performs Au deposition on a different substrate, while autocatalytic plating allows plating on a Au substrate.[19]

1.2.3 Bottom-up EL Au plating

It is widely reported that conventional EL Au deposition using Au(I) consists of four chemical regimes[20]: Sn sensitization, substrate catalyzed Ag activation, galvanic displacement of Ag by Au, and autocatalytic Au film growth. Figure 1.4 shows SEM images from the first three regimes with corresponding chemical reaction and T-UV spectra inset on the bottom LHS and top RHS, respectively. In the Sn sensitization process of Figure 1.4(A), a target surface is wetted by an acid solution of $SnCl_2$. The SnO_2 generated in the solution from the hydrolysis of stannous ion (Sn^{2+} (II)) adsorbs on the surface and Sn^{2+} act as molecular anchors for subsequent adsorption of catalytic nuclei.[21] Possible surface reaction mechanisms that have been suggested for Sn sensitization on SiO_2 glass substrate are:[21]

$$—\overset{|}{\underset{|}{Si}} – OH + SnCl_3^- + H_2O \leftrightarrows —\overset{|}{\underset{|}{Si}}—O—Sn—OH + 2H^+ +3\ Cl^- \qquad (1)$$

$$\overset{}{\underset{}{Si}}\overset{OH}{\underset{OH}{}} + SnCl_3^- \leftrightarrows \overset{}{\underset{}{Si}}\overset{O}{\underset{O}{}}Sn^{2+} + 2H^+ + 3\ Cl^- \qquad (2)$$

$$O\overset{—\overset{|}{Si}–OH}{\underset{—Si–OH}{\underset{|}{}}} + SnCl_3^- \leftrightarrows O\overset{—\overset{|}{Si}–O}{\underset{—Si–O}{\underset{|}{}}}Sn^{2+} + 2H^+ + 3\ Cl^- \qquad (3)$$
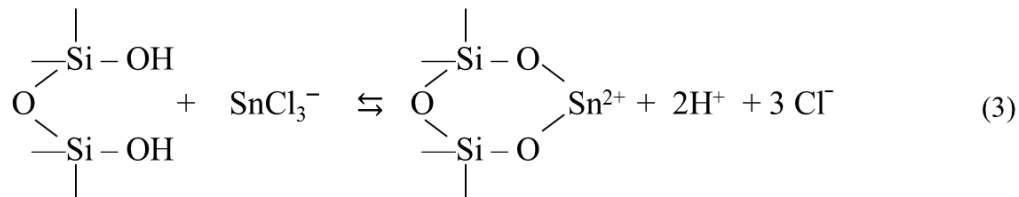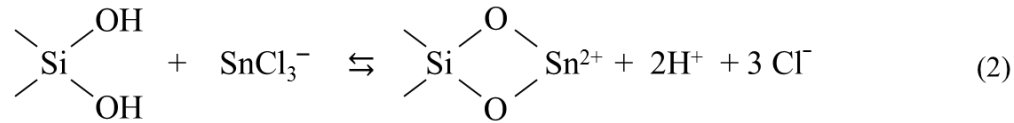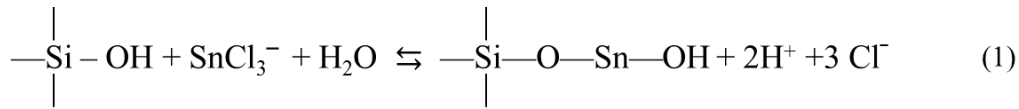
The Sn sensitized silicate substrate, as indicated in the transmission spectra in Figure 1.4(A), exhibited no observable spectral features relative to a referential bare glass substrate (overlapped Sn spectra). Its corresponding SEM image shows no recognizable specific features due to electron charging effects on semi conductive thin SnO_2 layer and nonconductive silicate glass. The feature in the upper LHS of the SEM image is a contaminant particle used to focus the
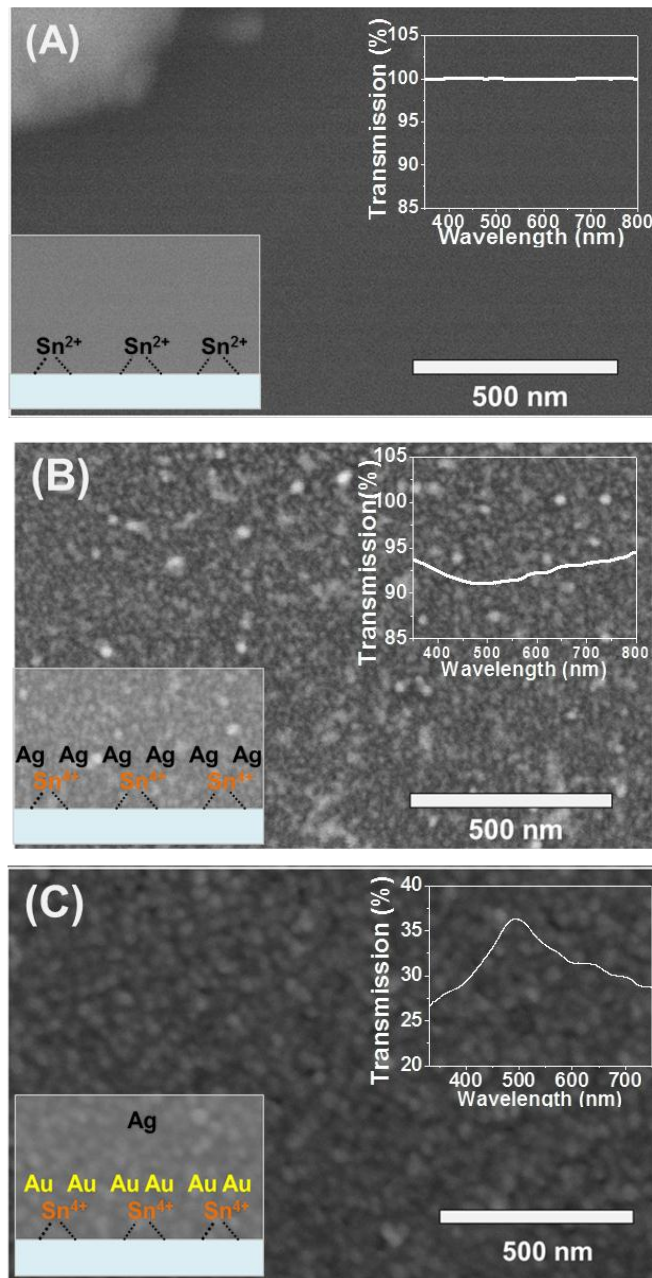
Figure 1.4. Images of products from three regimes of conventional EL deposition procedure: (A) Sn sensitized substrate (B) Ag activated substrate (C) Au deposited substrate after galvanic displacement of Ag by Au (batch immersion plating for 5 min: BI-5)

electron beam on the surface. Generally, SnO_2 thin film is considered to be optically transparent. The transparency of SnO_2 has been investigated in application of transparent conductor[22] and electrode of transparent dye-sensitized solar cell.[23]

After sensitization by Sn, the substrate is exposed to ammoniacal silver nitrate solution. The higher galvanic potential of Ag relative to Sn enables metallic Ag to cover the Sn layer via a rapid redox reaction. During Ag activation (Figure 1.4(B)), the adsorbed Sn(II) is oxidized to Sn(IV) concurrent with Ag(I) being reduced to elemental Ag(0), which adheres strongly to the surface. The suggested mechanism is shown in equations (4-5):[21]

$$\begin{array}{c}\diagdown\\Si\\\diagup\end{array}\hspace{-4pt}\begin{array}{c}O\\\diagdown\\Sn^{2+}\\\diagup\\O\end{array}\ +\ 2Ag^+\ \rightleftarrows\ \begin{array}{c}\diagdown\\Si\\\diagup\end{array}\hspace{-4pt}\begin{array}{c}O\\\diagdown\\Sn^{4+}\\\diagup\\O\end{array}\hspace{-4pt}\begin{array}{c}Ag\\\\\\Ag\end{array} \qquad (4)$$

$$Si\hspace{-4pt}\begin{array}{c}-Si-O\\\diagup\hspace{30pt}\diagdown\\\\\diagdown\hspace{30pt}\diagup\\-Si-O\end{array}\hspace{-20pt}Sn^{2+}\ +\ 2Ag^+\ \rightleftarrows\ O\hspace{-4pt}\begin{array}{c}-Si-O\\\diagup\hspace{30pt}\diagdown\\\\\diagdown\hspace{30pt}\diagup\\-Si-O\end{array}\hspace{-20pt}Sn^{4+}\hspace{-4pt}\begin{array}{c}Ag\\\\\\Ag\end{array} \qquad (5)$$
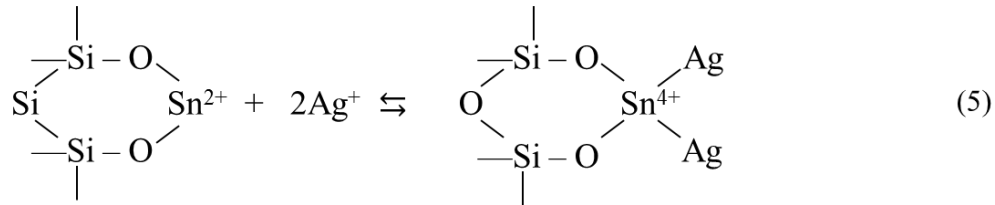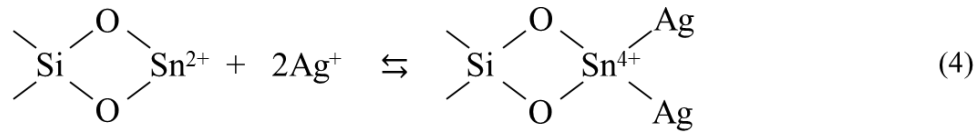
The reduced Ag adheres strongly to the Sn sensitized surface in the form of metallic Ag islands. Figure 1.4(B) shows that after 2 min of Ag reduction, the reduced Ag formed a thin island structure on the Sn sensitization layer. The T-UV spectra in the inset of Figure 1.4 (B) show a broad transmission valley with a minimum at ~500 nm. This decrease in transmission is attributable to deposition of thin metallic Ag island layer. An unannealed 2-nm thick mass of Ag island film was previously reported to exhibit absorption maxima at ~510 nm.[24] In separate work, an unannealed 5-nm thickness Ag island film showed a broad resonance peak around 520 nm.[25]

The metallic Ag is galvanically displaced by more noble metal Au^+ ions as illustrated by Figure 1.4 (C). In subsequent reduction of Au^+ ions onto the galvanically substituted Au film, a reducing agent, HCHO, plays the role of an electron donor to reduce Au(I) to Au(0). The galvanically substituted Au particle acts as a catalytic site after Au particles entirely cover with the substrate.[26] The proposed mechanism for galvanic replacement (Eq. 6) and autocatalytic Au film growth (Eq.7) can be represented as follows:[26]

$$\text{Si} \begin{matrix} \diagdown O \diagdown \\ \diagup O \diagup \end{matrix} \text{Sn}^{4+} \begin{matrix} \diagup Ag \\ \diagdown Ag \end{matrix} + 2Au^+ \rightleftharpoons \text{Si} \begin{matrix} \diagdown O \diagdown \\ \diagup O \diagup \end{matrix} \text{Sn}^{4+} \begin{matrix} \diagup Au \\ \diagdown Au \end{matrix} + 2Ag^+ \qquad (6)$$

$$2Au^+ + HCHO + 3OH^- \rightleftharpoons HCOO^- + 2H_2O + 2Au \qquad (7)$$
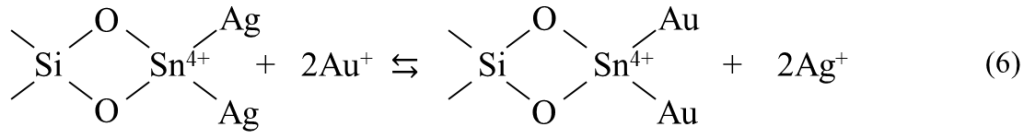
The SEM image of Figure 1.4 (C) shows EL deposition of Au form for 5 min results in a relatively continuous film structure. The film exhibits a spectroscopic PL feature at ~500 nm. The PL peak of EL Au thin film increased from 490 nm to 504 nm with increasing deposition time between 2 min and 6 min.[20]

1.2.4   Conventional nanopattern fabrication

Diverse nanofabrication techniques are being developed to meet scientific and industrial demand for highly ordered metal NP arrays. Namely, electron beam lithography (EBL) is commonly used to create precise nanopatterns with resolution on the order of several nanometers.[4,5] EBL works by tracing an electron beam in a specifically designed pattern across a surface coated with a thin film of polymer electron resist. The exposed regions of resist are then chemically removed in a process called "development", leaving the substrate exposed. Then thin

film evaporation or sputtering is performed on the developed pattern. Finally, the remaining resist region is lifted-off by chemical solvents to obtain the designed metal pattern.

1.3   Existing advantage/limitation of suggested fabrication methods

Conventional top-down metal depositions such as physical sputtering and chemical evaporation methods must be operated under highly-controlled conditions such as high temperature, pressure and vacuum necessitating costly sophisticated instrumentation. They share the limitation of one-dimensional deposition preventing their application in structures that require multi-dimensional deposition such as the internal walls of optical capillaries and three dimensional coatings on probe tips. Furthermore, these metal depositions require a conductive substrate, such as indium tin oxide (ITO), to create uniformly deposited films and regular arrays. Nonetheless, for non-pretreated substrate, the weak bonding between substrate and metal particles induced by lattice mismatch still results in discontinuous island structures. Technically, the discontinuity of island structures on the non-conductive substrate can be improved by ultra-thin (~5 nm) Cr pre-coating procedure. However, the Cr addition to the substrate is problematic to well-ordered nanostructures for applying biomolecular sensing, because the thin Cr layer may weaken sensitivity.[6,27] The developed particle shapes in EBL are limited to polycrystalline cylindrical structures due to characteristics of the electron beam and strong bonding between the deposited metal and Cr coated substrate. Additionally, the metal ion diffusion into the undercut between the polymer resist layer and the substrate surface is a common problem resulting in background metal residue. However, as an alternative plating method, conventional batch immersion EL (BI-EL) Au plating, using aqueous metallic solutions at ambient conditions, allows to satisfy the specific scientific demand for fabrication of various nanostructures without the need for an external electric energy source or a conductive substrate. Moreover, BI-EL

plating could develop an Au film with improved uniformity relative to top-down sputtering and evaporation. The uniformity of deposition still can be improved by a different mass transportation.

Figure 1.5 shows SEM images of four different Au films deposited on conductive substrates: BI-EL plating (a), evaporation (b) and sputtering (c,d). The BI-EL film exhibits a uniformly distributed, dense film with a thickness of approximately ~80 nm. Evaporated Au films on < 5 nm thick Cr pre-coated layer show randomly-sized particles and a less uniform morphology. The 8 nm sputtered film without Cr pre-coating shows distinguishable separated island features and the 80 nm sputtered film shows gaps between islands and distinct Au pillars of irregular shape. Also, Sn sensitization of BI-EL plating induces moderate bonding between deposited Au and the substrate which allows the creation of thermally transformed NP platforms over a range of thicknesses at the nanoscale.

Moreover, BI-EL plating mitigates health and safety issues by avoiding hazardous reagents like cyanide and hydrofluoric acid and eliminating hazardous plating solution wastes which are usually generated with electroplating. Optimized bench-scale BI-EL plating conditions such as plating solution composition, temperature, pH, agitation rate, reducing agent, bath stability, deposition rate and resulting crystal structure have been well characterized.[18]

1.4   Motivation and Objectives

In spite of these promising advantages of BI-EL Au plating, a suitable process for continuous operation on an industrial scale has not been developed and commercial BI-EL plating remains limited to bench-scale with micro-thickness structures.[18] To date, Roper's lab has focused on characterizing and fabricating Au nanostructures by BI-EL Au plating. Still, further
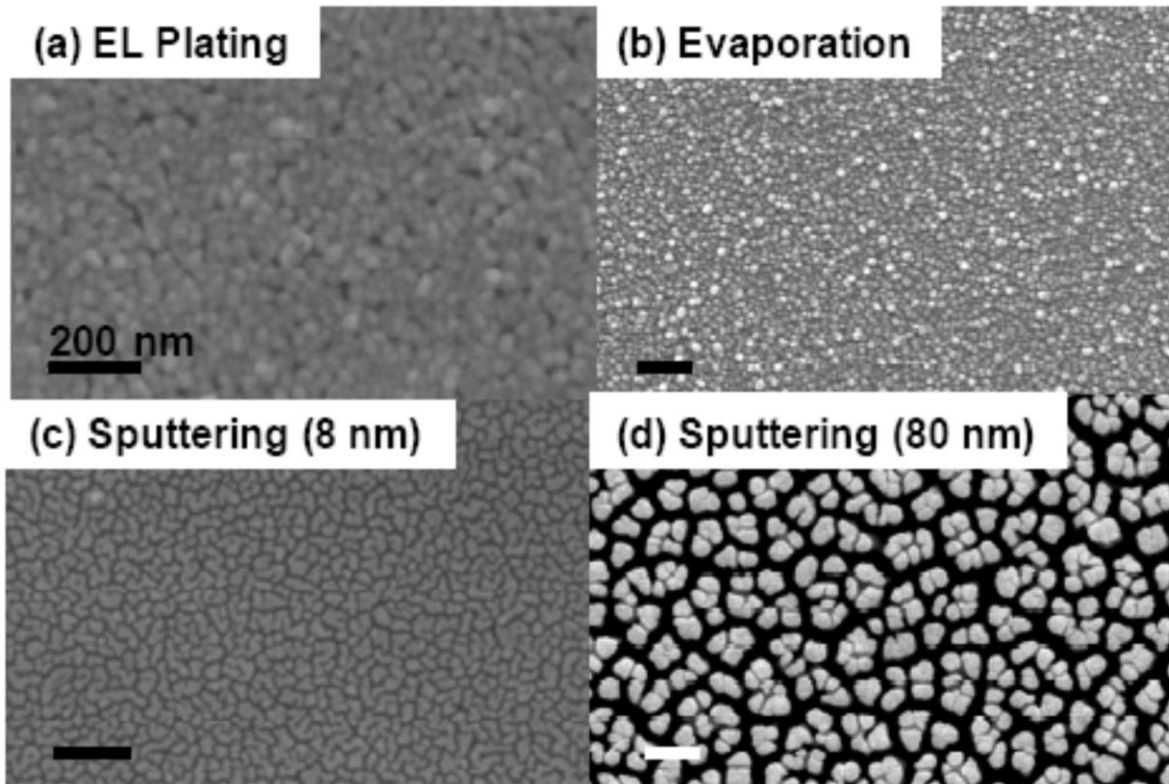
Figure 1.5. SEM images of diverse metal thin film. (a) EL Au film by BI-EL plating (b) Evaporated 50 nm Au film with 5 nm Cr coating (c) 8 nm- and (d) 80 nm-thick sputtered Au film without Cr coating (Adopted from Ahn[28]).

study is required to improve the precision of nanostructure and understand the chemistry. Technically, the uniformity of BI-EL Au film may be more improved by changing the present mass transportation mechanism, in which unsteady state mass transportation of BI-EL plating induced by decreasing concentration of metallic solution during plating forms non-uniform surface morphology. This presents one of the critical limitations to developing scale-able uniform metal thin films and nanostructures. Also, immersing a whole target substrate in the BI-EL solution bath can lead to unwanted surface plating, which is costly and labor-intensive. Furthermore, there are no generalized standard methods to characterize overall thickness and physical features of nanoscale EL thin film. Standard profilometer cannot measure less than a hundred nanometers and AFM is a time consuming, complicated method which is only available to local areas.

Therefore, based on understanding about the unsteady state diffusion of BI-EL plating, novel steady state diffusion system is developed to overcome suggested disadvantages. Then, the scalability of the novel plating system is validated by various micro- and spectroscopic characterization. As fundamental study, the film growth mechanism and diffusion phenomenon at steady and unsteady conditions are investigated using time-resolved characterization along with mass transfer models. For scale-up continuous EL plating system, the fast liquid and solid Au analysis approaches are studied using T-UV spectroscopy and spectrophotometric methods. Then, as application of novel plating system, the order Au NP arrays are fabricated.

The specific objectives of this work are described as follows;

I. Modeling (Chapter 2)

(1) Develop mass transfer models of EL Au plating and related correlations which allow characterizing metal film growth mechanism and predicting deposited amount of metal ion.

II. Fabrication (Chapter 3)

(1) Fabricate uniformly deposited EL Au thin films and thermally transformed random NPs using CF-EL plating system.

(2) Optimize Au chemistry of EL plating solution and hydraulic operation of CF-EL plating for uniform thin film

(3) Fabricate scalable CF-EL thin films using a flexible CF-EL Au plating system with real-time T-UV spectroscopy for quantitative, in-situ evaluation of dynamic spatiotemporal effects during Au deposition.

(4) Fabricate regular Au NP array via combination of EBL and CF-EL plating

III. Characterization (Chapter 4)

(1) Characterize structural and spectroscopic feature of CF-EL and BI-EL films and their NPs via micro-/spectroscopic analysis.

(2) Characterize balancing redox activity of Au(I) using TMB and develop a novel spectrophotometric Au ion assay for CF-EL plating solution.

(3) Characterize dynamic physical and optical features of EL metal deposition on silicate surface at steady and unsteady conditions measured using real-time T-UV spectroscopy, SEM and XPS.

(4) Characterize physicochemical sequential steps in EL Au deposition and validate possible mass transfer models predicting precise deposition rates and specific deposition amount.

1.5   References

(1) Surface plasmon resonance, Biacore (http://www.rci.rutgers.edu/~longhu/Biacore/pdf_files/ SPR_TechNote.pdf)

(2) Lim, D.; Jeon, K.; Hwang, J.; Kim, H.; Kwon, S.; Suh, Y.; Nam, J. *Nature Nanotech*.**2011**, *6*, 452-460

(3) Hutter, E.; Fendler, J. H. *Adv. Mater*. **2004**, *16*, 1685-1706.

(4) Zhao, L.; Kelly, K.L.; Schatz, G.C. *J. Phys, Chem. B* **2003**, *107*, 7343-7350.

(5) Lamprecht, B.; Schider, G.; Lechner, R.T.; Ditlbacher, H.; Krenn, J.R.; Leitner, A.; Aussenegg, F.R. *Phys. Rev. Lett*, **2000**, *84*, 4721-4724.

(6) Haes, A.J.; Hall, W.P.; Chang, L.; Klein, W.L.; Van Duyne, R.P. *Nano lett*. **2004**, *4*, 1029-1034.

(7) Ozbay, E. *Science*, **2006**, *311*, 189-193.

(8) Atwater, H. A.; Polman, A, *Nature Materials* **2010**, *9*, 205-213.

(9) Weissleder, R. *Nature Biotechnol.* **2001,** *19*, 316-317.

(10) Kalyuzhny, G.; Vaskevich, A.; Ashkenasy, G.; Shanzer, A.; Rubinstein, I. *J . Phys. Chem. B* **2000**, *104*, 8238-8244.

(11) Wei, Q.H.; Su, K.H.; Durant, S.; Zhang, X. *Nano Lett*. **2004**, *4*, 1067-1071.

(12) Chu, Y.; Crozier, K.B. *Opt. Lett.* **2009**, *34*,244-246

(13) Wajid, A. *Sensors ad Actuators A* **1997**, *63*, 41-46.

(14) Kaiser, N. *Applied Optics*, **2002**, *41(16),* 3053-3060.

(15) Martin, P. M. *Handbook of Deposition Technologies for Films and Coating-Science, Applications and Technologies*, 3nd ed.; Elsevier : 2010; Chapter 12

(16) Koch, Carl C. Nanostructured materials-Processing, Properties, and Applications (2nd ed.; William Andrew Publishing ; 2007; Chapter 6

(17) Luo, J.K.; Pritschow, M.; Flewitt, A.J.; Spearing, S.M.; Fleck, N.A.; Milne, W.I. J. Electrochem. Soc. 2006, 153, D155-D161

(18) Mallory, G. O.; Hajdu, J. B *Electroless Plating: Fundamentals and Applications* Eds.; American Electroplaters and Surface Finishers Society: Orlando, FL, 1990;

(19) Ali, H. O.; Christie, I. R. A. *Gold Bull*. **1984**, *17*, 118-127.

(20) Jang. G.; Roper, D.K. *J. Phys. Chem. C* **2009**, *113*, 19228-19236.

(21) Pederson, L. R. *Solar Energy Mater.* **1982**, *6*, 221-232.

(22) Park, H.; Park, H.; Hill, R.H. *Sens. Act. A* **2006**, *132*, 429-433.

(23) Tan, B.; Toman, E.; Li, Y.; Wu, Y. *J. Am. Chem. Soc.* **2007**, *129*, 4162-4163.

(24) Singer, R. R.; Leitner, A.; Aussenegg, F. R. *J. Opt. Soc. Am. B*, **1995**, *12*, 220-228.

(25) Baba, K.; Okuno, T.; Miyagi, M. *Appl. Phys. Lett.* **1993**, *62(5),* 437-439.

(26) Menon, V.P.; Martin, C.R. *Anal. Chem.* **1995**, *67*, 1920-1928

(27) Jin,Y.; Kang, X.; Song, Y.; Zhang, B.; Cheng, G.; Dong, S. *Anal. Chem.* **2001**, *73*, 2843-2849.

(28) Wonmi Ah, Ph. D Dissertation, Novel electroless gold nano-architectures to enhance photon-plasmon coupling, 2010

CHAPTER 2

2. Modeling of Electroless Au deposition[*]

The significance of the present work is described in Section 2.1 regarding mass transfer models in EL Au deposition. In section 2.2, mathematical deposition rate equations for BI-EL plating is described to predict deposition amount on a substrate. The Au ion transfer rate of CF-EL Au plating is described in Section 2.3. Applicable mass transfer models for scalable CF-EL plating and considerations with relevant quantitative mass balance equations are present in Sections 2.4. and 2.5. The concluding statement for this chapter follows in Section 2.6

2.1   Significance of the Present Work

A conventional EL Au plating has been performed by immersing a target substrate in working metallic solution baths. Due to no external driving force for deposition, the lower plating rate relative to electroplating was a challenging technical issue for microstructure development. Thus, many studies had focused on either optimizing thermo-mechanical conditions or controlling chemical composition to improve deposition rate in stable operation condition. However, the low deposition rate and non-uniform surface morphology formation are still problematic due to the fundamental mass transfer issue, depletion of metal ion solutions during batch immersion (BI) plating. Thus, less industrial and scientific demand resulting from the limited scalability of bench scale, the study of metal ion diffusion for thin film formation at an atomic view in aqueous phase had not investigated since 1990s. In this work, novel CF-EL plating system is developed to overcome the unsteady mass transportation of BI-EL plating. In

particular, various mass transfer models are studied to interpret the Au diffusion in these two different system, BI-EL and CF-EL Au deposition.

This study of Au ion diffusion in EL Au plating is important to develop a future industrial continuous process and control over ultra-thin film formation. Particularly, the calculation of deposited amount enables not only to predict the physical dimension of deposited solid Au such as thickness, but also to suggest optimal operating conditions for various dimension substrates. Controlling steady (CF-EL) and/or unsteady state (BI-EL) diffusion conditions also allow improving the opto-physical feature of deposited EL Au film by involving the surface morphology formation and continuity of deposited Au clusters.

2.2   Mass transport in conventional BI-EL plating

To date, EL Au deposition has been performed by immersion of a substrate into a series of metal ion solutions. Figure 2.1 shows a schematic of the hypothesized mass transfer model during BI-EL plating. In BI-EL plating, Au ions in a stagnant medium diffuse toward and deposit onto the substrate wall during incubation. The mass transfer model of BI-EL plating via unsteady-state molecular diffusion considers the depletion of species with respect to time in a unit volume through which the species are diffusing. Unsteady diffusion from a semi-infinite medium, rather than a finite slab, best describes this system since $D_{AB}t/a^2 < 1/16$ where $a =$ half the thickness of the flow channel, and other parameters are defined following equation 1. Thus, the instantaneous rate of molar transfer (n) of immersion plating on a wall is described by :[1]

$$n_A\big|_{z=0} = \sqrt{\frac{D_{AB}}{\pi t}} A \Delta C \quad (2.1)$$
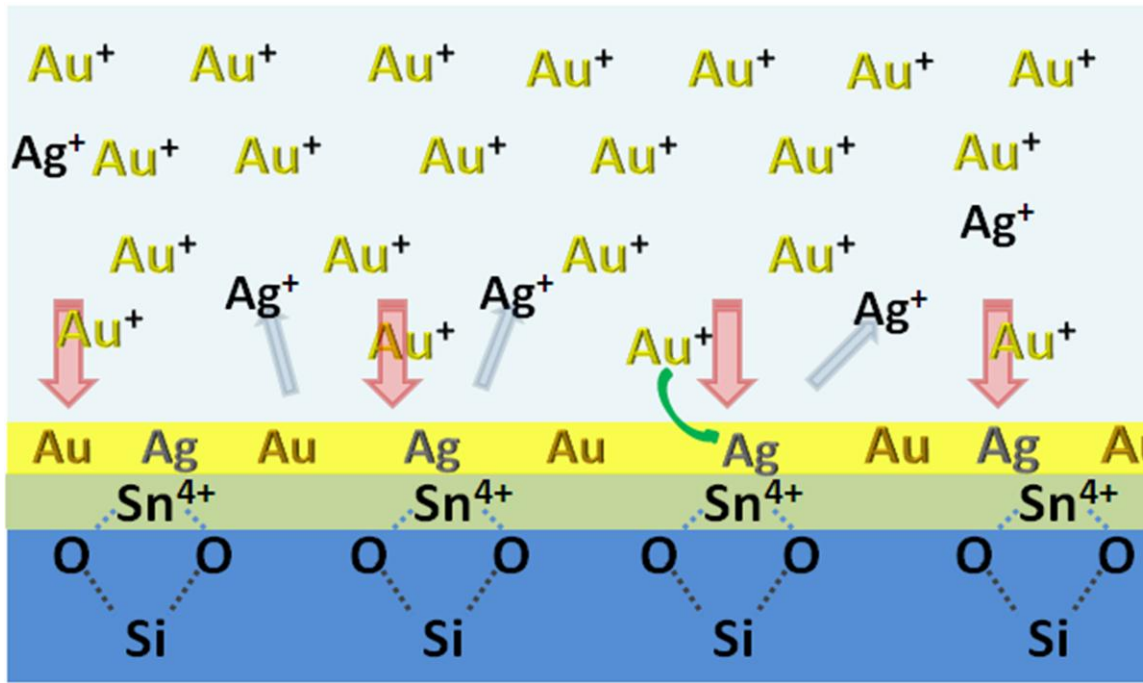
Figure 2.1. Schematics of a mass transfer model in BI-EL Au plating.

where A = the area of substrate, t = elapsed time, D_{AB} = diffusivity of A ions in an aqueous solution(B) and ΔC= concentration difference between Au ion in bulk solution and at the surface of substrate.

Au film morphology and thickness depend on the total number of Au ions deposited onto the substrate. For BI-EL plating, the total number of solute ions (M_A) transferred into the semi-infinite medium is determined by integrating equation (2.1) with respect to time:

$$M_A = \left[2A\sqrt{\frac{D_{AB}t}{\pi}}\,\Delta C \right] \times N \quad (2.2)$$

where N is the number of immersions onto an open substrate.

For scalable BI-EL plating, we also suggest a finite one-dimensional, unsteady-state diffusion model[1] to predict Au deposition in a confined system. The instantaneous rate of mass transfer (n_A) across the surface of either unsealed face of the medium (i.e., at z = ±a) is

$$n_A\big|_{z=a} = \frac{2D_{AB}(C_{As} - C_{Ao})A}{a^2} \times \sum_{n=0}^{\infty} \exp\left(-\frac{D_{AB}(2n+1)^2 \pi^2 t}{4a^2} \right) \quad (2.3)$$

where C_{As}= Concentration at surface, C_{A0}=Concentration in bulk

The total number of moles transferred across either unsealed face is determined by integrating equation (2.3) with respect to time. Thus,

$$M_A = \frac{8(C_{As} - C_{Ao})Aa}{\pi^2} \times \sum_{n=0}^{\infty} \frac{1}{(2n+1)^2}\left(1 - \exp\left[-\frac{D_{AB}(2n+1)^2 \pi^2 t}{4a^2} \right] \right) \quad (2.4)$$

2.3   Mass transport in CF-EL plating

Due to improved optical and physical features and compatible engineering scale-up possibility, CF-EL plating is a more effective process to continuous industrial fabrication relative to BI-EL plating. Thus, developing a mass transfer model for CF-EL plating is an essential step to be fulfilled in advance.

CF-EL plating occurs via steady deposition from an adjacent bulk in laminar flow. In CF-EL plating, the developed mass transfer coefficient is different from BI-EL due to continuous laminar flow which decreases the stagnant boundary layer adjacent to the wall and provides time-invariant Au concentration and Au deposition rate. The mass transfer rate of CF plating has been defined using the two-compartment and effective rate models which use a first-order transfer coefficient to account for diffusive mass transfer resistance to the functionalized silica substrate.[2,3] In brief, solutes at uniform concentration equal to the injection concentration flow in an outer compartment at a constant rate (F) parallel to the surface in an open channel while solute concentration in an inner compartment increases at rates due to mass transfer from the outer compartment (k_m) and desorption from the interface of compartment (k_r). Simultaneously, inner compartment solute concentration decreases at a rate due to deposition onto the substrate surface (k_f). The forward and reverse mass transfer coefficient (k_m) is related to flow cell length (L), width (w) and flow thickness (h), operational flow rate (F) and molecular diffusivity (D_{AB}) by :[2,3]

$$k_m = \frac{1.5}{\Gamma(4/3)}\left[\frac{D_{AB}{}^2\gamma}{9L}\right]^{\frac{1}{3}} \quad (2.5)$$

where $\gamma = 6F/(h^2w)$ is the wall shear rate.

Figure 2.2. shows the entire procedure of CF-EL Au plating. Overall CF-EL plating procedure is a combination of both steady state mass transfers during laminar flow and unsteady state diffusion during post injection incubation. In the CF-EL plating, metal ion solutions are continuously injected into a confined rectangular substrate channel to produce a higher, time-invariant Au deposition rate via a higher, steady concentration driving force across a narrower stagnant boundary layer adjacent to the surface. In the incubation, Au ions in a stagnant medium diffuse toward, and deposit onto the substrate wall during incubation. In the washing, the continuous flow plating is applicable. Thus for CF-EL, the total moles of mass transferred solute ions, M_A, is obtained by adding the semi-infinite mass transfer solution (2.2) and the steady state mass transfer solution (2.5), resulting in:

$$M_{AB} = A\Delta C \left[k_m t_2 + 2\sqrt{\frac{D_{AB}t_1}{\pi}} \right] \quad (2.6)$$

where t_1 and t_2 are the time of batch immersion and continuous flow, respectively.

2.4   Mass transport model for fully developed laminar flow

Two other mass transfer models were compared to determine the better models for CF-EL plating in the scalable rectangular channel. When solutes are passed into a confined flow channel, the developed concentration profile yields calculable expression for the mass-transfer coefficient and the Sherwood number. For a long length of flow channel, the concentration profile is fully developed and the local Sherwood number, N_{sh}, approaches a limiting value of 3.656. The constant dimensionless local mass transfer coefficient suggests that a steady amount of introduced solutes deposit along the inside surface of a channel. Thus, a uniformly deposited Au film overall substrate could be formed by performing EL plating
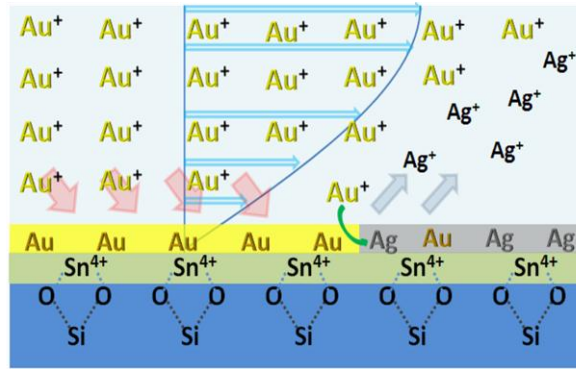
(1) Continuous flow plating
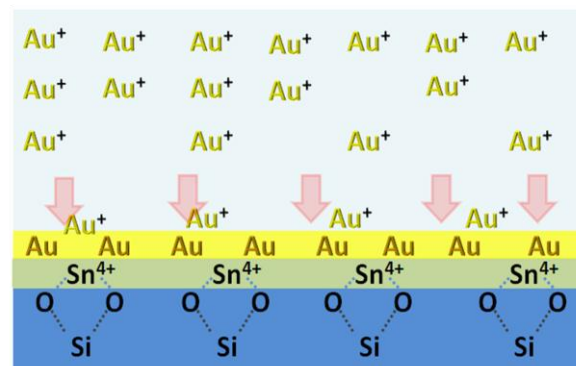
(2) Incubation (Immersion)
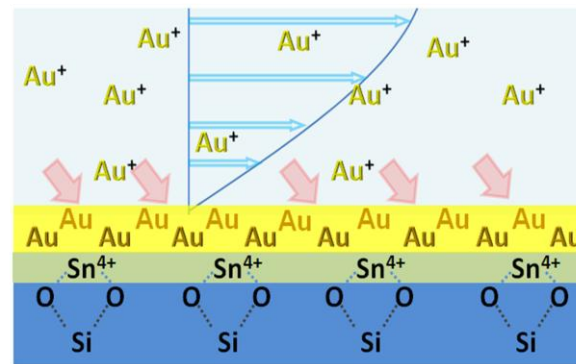
(3) Washing (CF plating)

Figure 2.2. Schematics of entire CF-EL plating procedure. (1) Substrate Sn sensitization, activation with Ag and galvanic replacement of Ag by Au are performed with a series of injections of metallic solutions (Sn, Ag, Au) during CF-EL plating; (2) Incubation period while the Au syringe was exchanged with a syringe containing H_2O; and (3) Thorough rinse with H_2O.

in a fully developed laminar flow. The empirical expression for the average Sherwood number proposed by Hausen[1] is

$$N_{Sh_{avg}} = 3.66 + \frac{0.0668[N_{Pe_M}/(x/d_H)]}{1 + 0.04[N_{Pe_M}/(x/d_H)]^{2/3}} \quad N_{Pe_M} = \frac{d_H u_x}{D_{Au}}, \; k_{c_{avg}} = N_{sh_{avg}} \frac{D_{Au}}{d_H} \quad (2.7)$$

where x= length of flow channel. d_H= hydraulic diameter of channel. This correlation is based on a log-mean concentration driving force.

A general empirical film-model correlation can suggest typical mass-transfer coefficients for a channel flow with membrane separation. The model may be applicable to define Au ion deposition on the selective substrate in EL plating. The dimensionless mass transfer coefficient for laminar flow ($N_{Re} <$ 2,100) is:

$$N_{Sh} = k_i d_H / D_{Au^+} = 1.62 \left[N_{Re} N_{Sc} \frac{d_H}{L} \right]^{1/3} \quad (2.8)$$

where $N_{Sc} = \mu/(\rho D_{Au^+})$, $N_{Re} = d_H Q/(A_c \nu)$, μ = dynamic viscosity, ν = kinematic viscosity, Q = volumetric flow rate (m^3/s), A_c = cross sectional area of flow channel, ρ = density, d_H= hydraulic diameter($2hw/(h+w)$), and k_i= mass transfer coefficient at interface.

2.5   Consideration of CF-EL plating in scalable deposition substrate

Momentum and mass transfer affect the scale-ability of the CF-EL method. In an ideal channel, a hydrodynamic entrance region length, x_h, required to achieve fully developed laminar flow is given by[1]

$$\frac{x_h}{d_H} = C \cdot N_{Re} \quad (2.9)$$

where C is an empirical constant whose recommended value is 0.05[1].

The mass transfer coefficient in (2.7) is valid for thin concentration boundary layers that occur before the concentration profile is fully developed, at which point the local Sherwood number reduces to its lower limiting value of 3.656.[1]

For introducing a fully developed laminar flow in the channel, the second consideration is that the mass of Au ion entering the channel must meet or exceed the mass deposition. Based on the assumption that the concentration of Au ion at the substrate interface is zero due to Au crystallization, the limitation of entire mass-transfer deposition, with fully developed laminar concentration profiles, are constrained by

$$F \geq \frac{k_{avg} A_s}{\ln(\frac{\overline{C_{A_0}}}{\overline{C_{A_x}}})} \quad (2.10)$$

where F= volumetric flow rate, A_s = surface deposition area, k_{avg}= average mass transfer coefficient, C_{A0}= Au concentration at inlet, and C_{Ax}= Au concentration at outlet.

After calculating mass transfer coefficients (k_m and k_i) in the models, the average concentration of Au ion in the out-flowed solution ($\bar{c}_{A_x}$) can be predicted by the mass flux balance relationship using log-mean concentration driving force.[1] Then the total deposited amount of Au ion (M_A) to the surface (c_{Ao}) can be determined by integrating mass flux balance equation with respect to time (t):[1]

$$M_A = n_A t = Ft(\bar{c}_{A_x} - c_{A_o}) = k_i \, At \frac{[(c_{Ai} - c_{Ao}) - (c_{Ai} - \bar{c}_{Ax})]}{\ln[\frac{c_{Ai} - c_{Ao}}{c_{Ai} - \bar{c}_{Ax}}]} \quad (2.11)$$

where F = volumetric flow rate, A = deposition area, c_{Ai} = concentration of the in-flowed solution, c_{Ao} is the concentration at the surface, and $\bar{c}_{Ax}$ is the average concentration at a distance x along the flow channel.

These predicted mass transportation values will be validated by experimental Au assay for out-flowed solution and dissolved Au deposited film.

2.6   Conclusion

In summary, a semi-infinite diffusion model and a finite slab model are described to interpret mass transfer rate in BI-EL plating. Three different mass transfer models such as two-compartment with effective rate, fully developed laminar flow, and general empirical thin film, are suggested to predict Au deposition amount on the substrate channel during CF-EL plating. The relevant entrance region expressions and mass balance equations for limitation of entire uniform CF-EL plating will be a standard to determine an optimal CF-EL plating condition. The mass flux balance correlations allow predicting the total deposited amount of Au ion after CF-EL plating and suggest a guideline for an Au assay which validates the best fitted CF-EL model.

2.7   References

(1) Seader, J. D.; Henley, E. J. *Separation Process Principles.* 2nd Ed. (John Wiley and Sons, Inc.2006).

(2) Roper, D. K. *Chem. Eng. Sci.* **2006**, *61*, 2557–2564.

(3) Roper, D. K. *Chem. Eng. Sci.* **2007**, *62*, 1988–199

CHAPTER 3

3. Fabrication of SPR Enhanced Au nanostructure via CF-EL plating

A novel CF-EL plating system is developed by integrating a syringe, a syringe pump, connecting tubes and a flow cell, which allow enhanced mass deposition rate in equilibrium diffusion condition. Combining this system with EBL, CF-EL plated Au films and nanostructures were fabricated for enhancing surface plasmon resonance features. Especially, a novel automated CF-EL plating system integrated with a real-time T-UV spectroscopy enable us not only to fabricate scalable uniform EL thin film but also to characterize the transitory optical transformation regimes during EL Au film growth. This chapter is organized as follows: The significance of this work is illustrated in Section 3.1 regarding the advantage of CF-EL plating. Section 3.2 describes simple fabrication procedure and its results of uniformity enhanced EL Au thin film via a novel CF-EL plating system. Section 3.3 demonstrates fabrication procedure of 2D ordered NP arrays via CF-EL plating on EBL sample. The scalable CF-EL films fabricated by a novel automated CF-EL plating system with a built in real-time T-UV spectroscopy are described in Section 3.4. Section 3.5 illustrates optimization of Au solution chemistry and hydraulic operation conditions for scalable CF-EL plating. Concluding statement for this chapter follows in Section 3.6.

3.1 Significance of the Present Work

In this work, a steady state Au deposition system, so called CF-EL Au plating system, is developed as a novel EL Au plating method which allows controlling deposition rate at equilibrium condition. As described in Chapter 2, while the control of mass transfer rate in BI-EL plating is limited to the closed system due to no external metal ion source, the CF-EL plating enables us to control local mass transfer rate with varying operating conditions such as injection

flow rate due to supply of metal ion from an outer system. Furthermore, it is expected that the steady deposition rate resulting from CF improve physical surface uniformity of deposited Au films and easier prediction of mass transferred amount relative to unsteady deposition of BI-EL plating.

In this chapter, uniform enhanced EL Au thin film and NPs are fabricated by a prototype of EL plating system and following thermal treatments. As a comparison, EL Au thin film and NPs are fabricated using BI-EL plating method. Regular Au NP arrays are developed by combining EBL and CF-EL plating for an application. For scalable EL Au film and time-resolved characterization of EL Au thin film growth, a novel automated CF-EL plating system is developed with integrating a real-time T-UV spectroscopy.

3.2   Uniformity Enhanced EL Au thin film by a novel CF-EL plating

3.2.1   Experimental Method for BI and CF-EL plating

Au thin film coating onto the internal surface of borosilicate glass capillaries was performed by the immersion method and CF-EL deposition method. Figure 3.1 shows a CF-EL plating system developed by integrating a syringe, a syringe pump, connecting tubes and a flow cell. The detailed procedure of BI-EL method and CF-EL method are well described in the published paper .[1]

3.2.2   Results of fabricated BI-EL and CF-EL films

CF-EL plating improves continuity of Au thin films. Figure 3.2 shows SEM images of Au thin films produced by CF-EL plating at various flow rates (A,B); BI-EL plating with different substrates (C,D); Au evaporation (E); and sputtering (F). In EL plating, dissolved Au(I) reduces to surface-associated Au(0) by galvanically displacing Ag, producing a Au island film due to
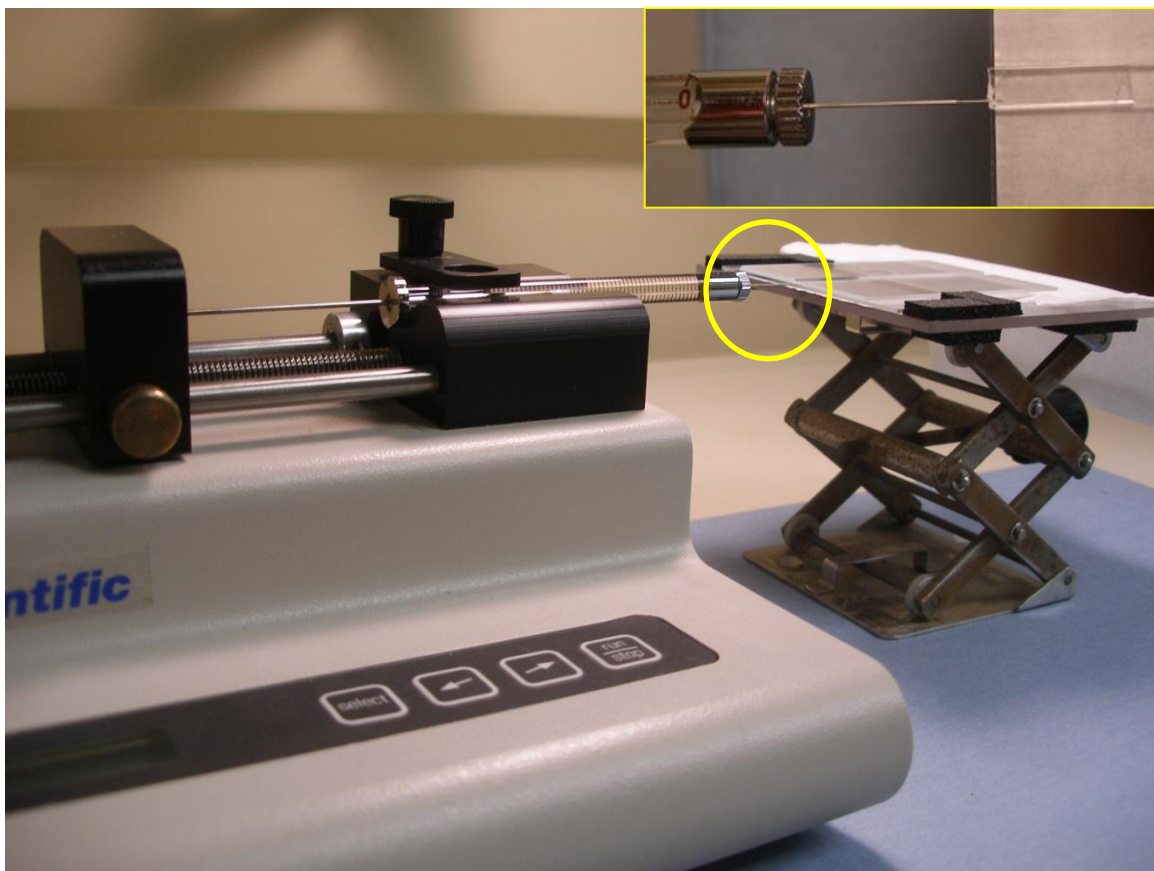
Figure 3.1 Schematic of a prototype CF-EL plating system showing syringe pump, glass syringe, and (inset) optical capillary.
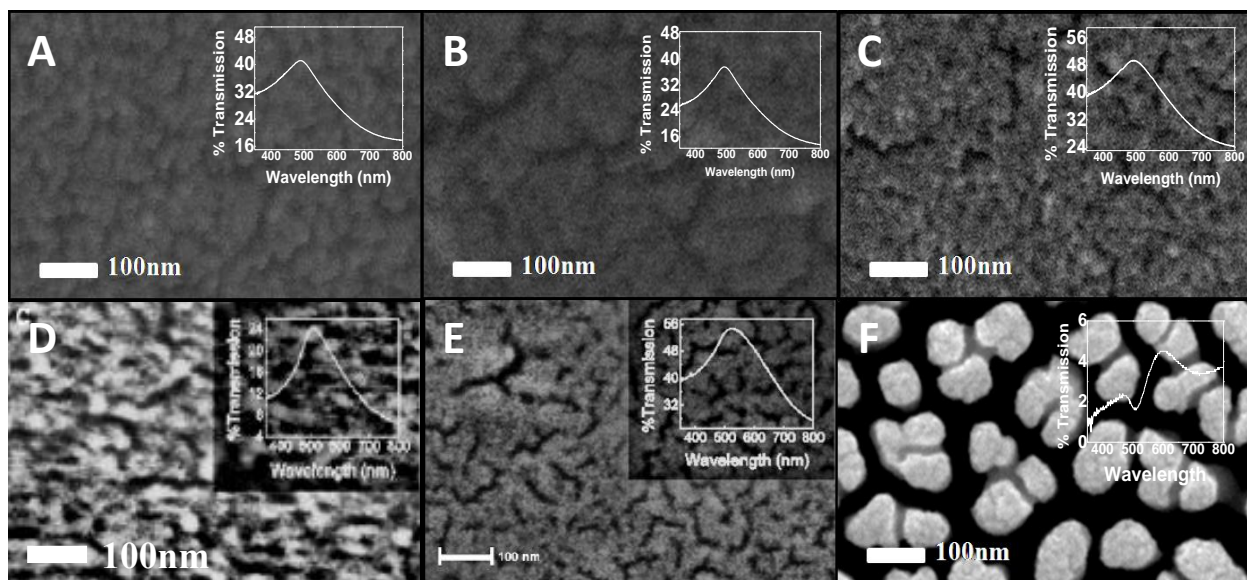
Figure 3.2. SEM images of Au thin films deposited by EL plating via CF, BI, evaporation, and sputtering. (A) CF-EL plating in rectangular capillary for 2 min at 800µl/h followed by 1 min incubation, (B) CF-EL plating for 2 min at 1000µl/h followed by 1 min incubation, (C) BI-EL plating in capillary for 4 min total, (D) BI-EL plating on fused quartz slide for 4 min total (from Ahn[4], 2008), (E) Evaporation on fused quartz slide at 20 nm/min for 0.33 min (from Ahn[5], 2010), (F) Sputtering on ITO glass for 20 min. Insets are T-UV spectra corresponding to each image.

weak binding on the silica substrate. The EL Au films in Figure 3.2.A and B were deposited in borosilicate capillaries at flow rates of 800 μl/hr (CF-EL 800) and 1000 μl/hr (CF-EL 1000), respectively. Total plating time for CF-EL films was 3 min: two minutes of continuous flow plating was followed by 1 min of static incubation during which the Au and H_2O syringes were exchanged. Rectangular capillaries were subsequently split along the narrow wall to observe each primary wall separately by SEM. Figure 3.2.C shows Au film from BI-EL plating inside a borosilicate capillary for 4 min. The SEM images of Figure 3.2.D and E represent a 4 min immersed deposited Au film on quartz slide and Au evaporated on quartz slide at 20 nm/min for 0.33 min, respectively. A sputtered film on ITO glass is shown in Figure 3.2F.

Comparing SEM images in Figure 3.2. shows that Au films produced by CF-EL appear continuous and relatively uniform compared to films obtained by BI-EL plating on quartz slides, evaporation, and sputtering. In particular, the sputtered film (Figure 3.2.F) shows discrete island structures with diameters up to ~150 nm. The surface morphology of the evaporated film in Figure 3.2.E exhibits discontinuous island structures. The higher density of dark grooves and holes on the surface indicate a lack of continuity, compared with CF-EL films and a BI-EL film (Figure 3.2.A, B and C). The BI-EL films on capillaries and quartz slides (Figures 3.2.C and D, respectively) appear less uniform and continuous than Au thin films deposited by CF-EL. The Au film deposited via BI-EL plating on quartz slide in Figure 3.2.D appears more discontinuous than the BI-EL film deposited on internal surfaces of a capillary (Figure 3.2.C).

3.3 Two dimensional regular arrays fabricated by combination of CF-EL plating and EBL

3.3.1 Experimental Method for BI and CF-EL plating

Substrate Preparation: Indium tin oxide (ITO) coated polished glass slides (SPI Supplies, West-Chest, PA) were used to provide electrical conductivity for electron beam lithography (EBL) operation in SEM. ITO slides (8×8 mm, thickness 0.8 mm) were cut for CF-EL plating. Before Au EL plating was performed on the EBL substrate, the bare ITO substrate was pre-treated. The ITO slides were tin pre-sensitized by immersion in Sn solution for 4 min to improve uniformity and circularity of deposited particles.[2] The Sn pre-sensitized ITO substrate was spin-coated using a CEE 100 spin coater (Brewer Science, Inc., MO) with 950 kamu PMMA and baked at 150 °C for 1 min. Rotational speed was 4,000 rpm with 3 % poly(methyl methacrylate) (PMMA) concentration to produce a PMMA thickness of approximately 250 nm.

Pattern Creation by Electron Beam Lithography: EBL was performed using a Philip XL 30 Environmental scanning electron microscopy (ESEM) (FEI, Hillsboro, OR) installed with a Nanometer Pattern Generation System (NPGS, Bozeman, MT) to create patterns, control electron beam dosage, and use stage movement. Square arrays of holes in the PMMA were created with an electron beam dose of 2.9 ~ 29.0 $\mu C/cm^2$ for ITO slides with a PMMA thickness of 250 nm. After beam exposure, the sample was developed in a room temperature mixture of methyl isobutyl ketone (MIBK) and isopropyl alcohol (IPA) (1:3 vol.) for 1 min, rinsed with IPA, and then immersed in IPA for 2 min with gentle agitation. In this work, 100.5×100.5 μm^2 square arrays were prepared with lattice spacing of 670 nm.

Creation of Uniform Au NP Arrays by CF-EL Au plating: Figure 3.3. shows the combined procedure of CF-EL Au plating on EBL-produced patterns. Injection of metallic solution for EL Au plating was performed by utilizing a CF-EL plating system. Transparent flow channel frames ($1.2 \times 9 \times 9$ mm) and covers were designed using cut slides, epoxy and silicon. A channel was left at one corner to allow fluid egress. Hot wax was used to seal the edge of E-beam patterned ITO glass and fix on the surface of bottom flow channel. The cover was sealed with silicone rubber. Sodium Au sulfite solution was purchased from Oromerse Part B and was diluted to 0.00153 M for plating. The activation of ammoniacal $AgNO_3$ for 2+1 min (2 min continuous flow and following 1 min incubation), and galvanic replacement of Au for 15+1 min were performed on the substrate by injecting each metallic solution through a micro syringe system. In order to compare with spectral feature of regular array, the random arrays of Au NPs were fabricated on the bare ITO glass by the same plating procedure. After then, Au plated EBL substrate was immersed to dissolve the remaining PMMA in 50 °C acetone for 5 min. The lift-off resulted in uniform arrays of Au cylinders from 250 nm-thick-PMMA slides. Repeated flash thermal annealing for both regular and random Au island film was performed at 850 °C for 90 second to form spherical Au NPs and long term annealing was followed at 350 °C for 100 hrs to improve sphericity.

3.3.2 Results of fabricated Au NP array via CF-EL plating

Using CF-EL Au plating on a Sn pre-sensitized EBL patterned substrate, we successfully fabricated highly ordered arrays of Au NPs with varying size, shape, and pattern. Figure 3.4 shows the SEM images of the resulting film patterns after lift-off and thermal transformed NP arrays. Adopting Sn pre-sensitization substrate with CF-EL plating and EBL could deposit completely filled Au nano-cylinders due to the enhanced mass transfer rate. The subsequent flash
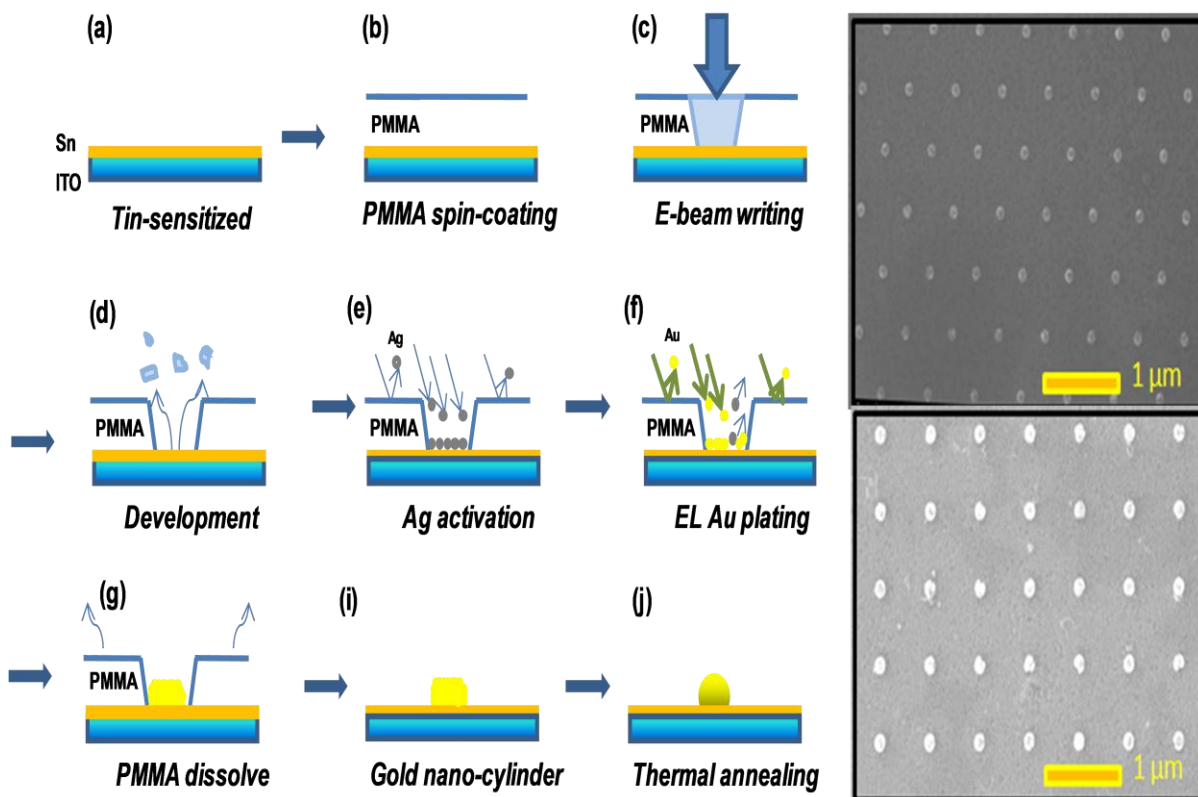
Figure 3.3. Schematic of fabrication process of CF-EL plating on tin pre-sensitized EBL pattern.
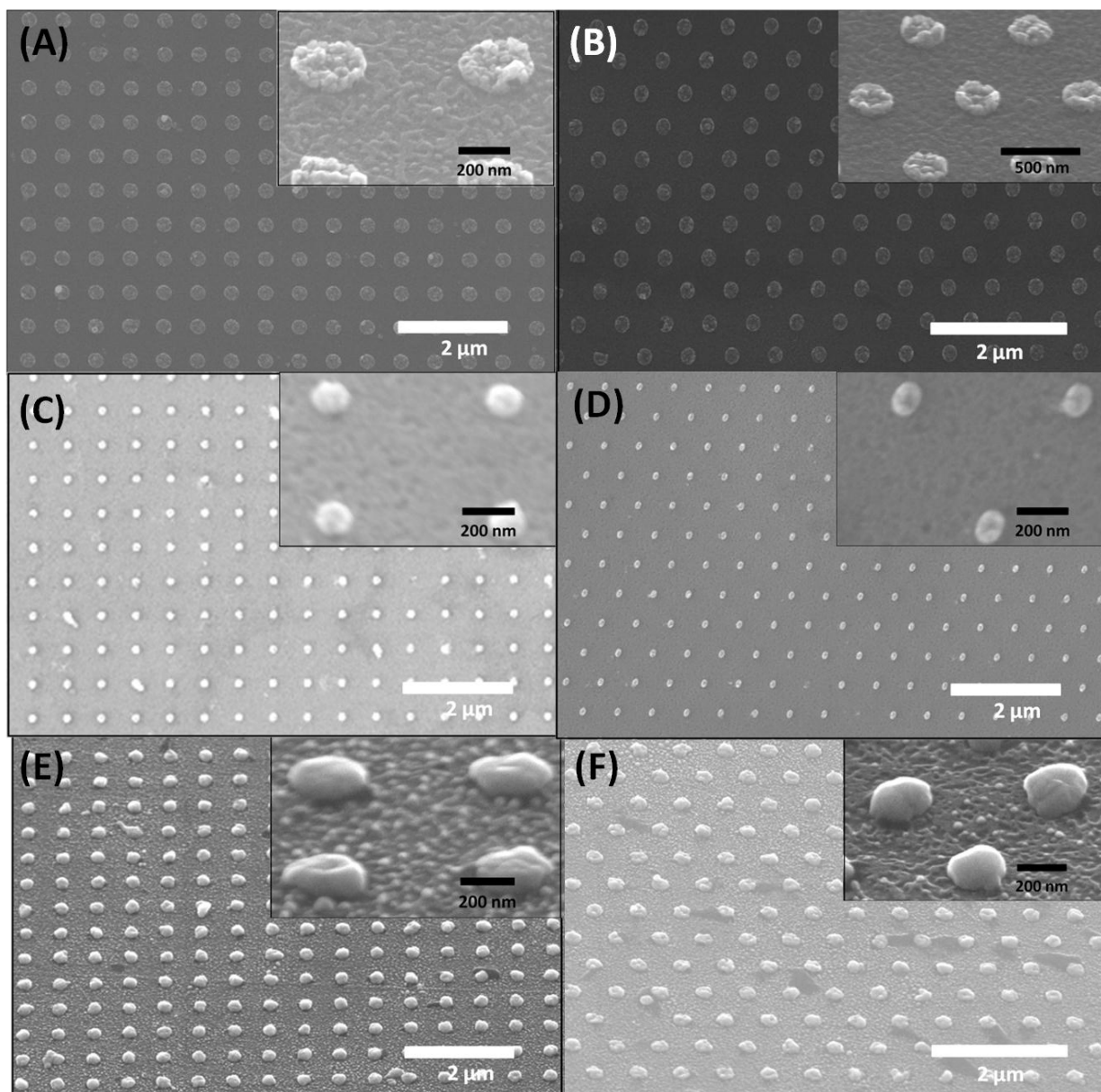
Figure 3.4. SEM images of regular array fabricated by EBL and CF-EL Au plating; (A) Square array, (B) Hexagonal array, (C) Size controlled square Array, (D) Size controlled hexagonal Array, (E) Annealed square array, (F) Annealed hexagonal array.

thermal annealing transforms the deposited polycrystalline nano-cylinder to a single-crystallized nanosphere. Our novel approach enables the fabrication of high resolution, ordered regular metal NP array which would allow improved optical and plasmonic features in sensing and imaging devices, as well as reduced fabrication cost and effort.

3.4 Scalable CF-EL Au thin film fabrication via automated CF-EL plating system with real-time T-UV spectroscopic measurement

3.4.1 Experimental Method

Scalable EL Au deposition and simultaneous optical monitoring were performed by automated CF-EL plating system with real-time T-UV spectroscopy (Figure 3.5). The T-UV spectroscopy measured time-resolved spectra variations during the procedure of CF-EL deposition from Ag activation and Au deposition. The injection of metallic solution was semi-automated by each flow pump. BI-EL plating was performed in the automated CF-EL plating system to characterize spectra variation. The detailed procedure of CF-EL deposition is well described in the published papers.[3]

3.4.2 Optimization of Au solution chemistry and hydraulic operation condition for scalable CF-EL plating

Table 3.1 compares the deposited surface morphology of CF-EL film with varying a final Au solution concentration in the mixture of sodium gold sulfite, Na_2SO_3 and HCHO via diluting stock sodium gold sulfite solution with D^3-H_2O at a determined ratio and then mixing the diluted sodium gold sulfite solution with Au reducing reagent (Na_2SO_3 and HCHO) at 1:6 of dilution ratio. The CF-EL plating was performed on ITO glass with 3 ml/hr for increasing plating time. At 0.0157M of Au, 10 min plating, as shown, produces irregular flakes deposited film.
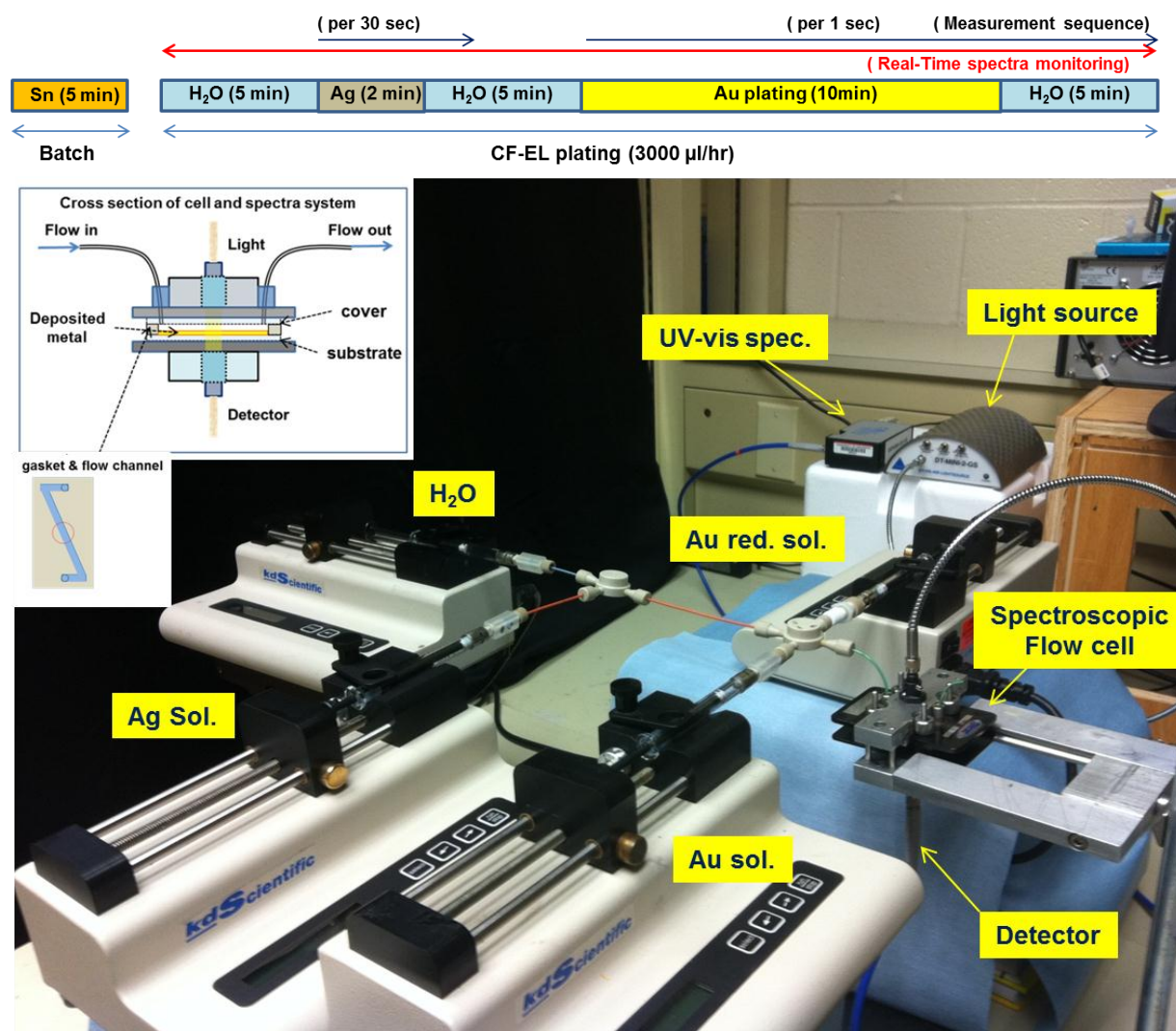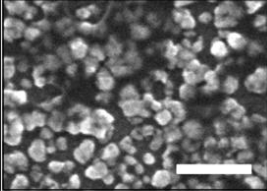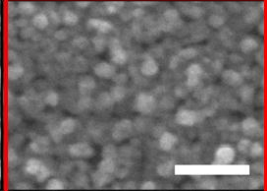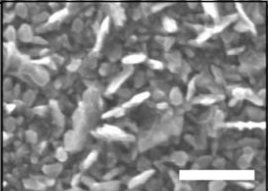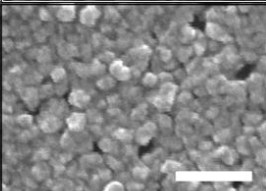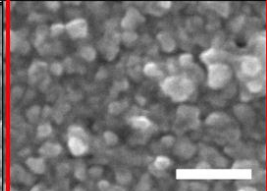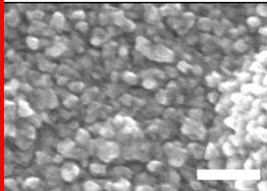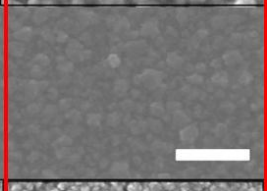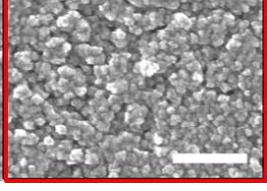
Figure 3.5. The automated CF-EL Au plating system with real-time T-UV spectroscopy. The upper diagram represents the cycle of EL plating with real-time monitoring. Inset is the cross section of flow cell with spectra system.

Table 3.1. Optimization of Au concentration conditions *vs* CF-EL plating time.

Substrate: ITO glass, Stock sol. :0.11M

Au \ Time	0.0157M (1:6)	0.0078M (1:1→1:6)	0.0052M (1:2→1:6)	0.0022M (1:6→1:6)
5 min				
10 min				
15 min				
20 min				
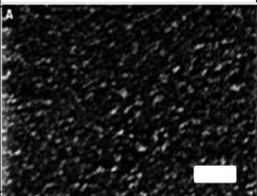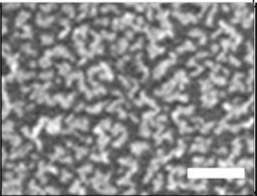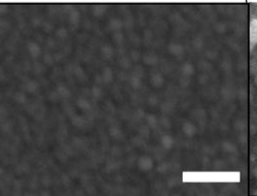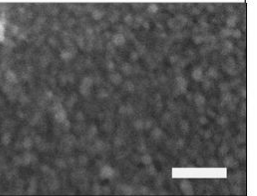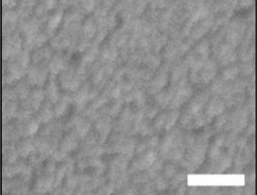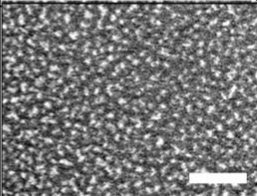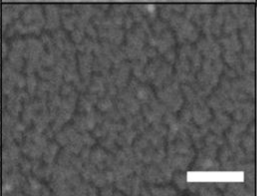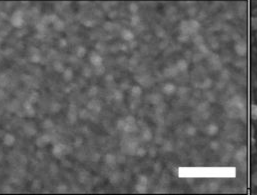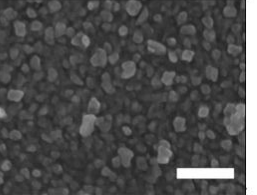
Scale bar =200 nm

Interestingly, as the Au concentration decreases to 0.0078M, the SEM image shows well defined Au grains deposited to form a continuous film. However, 5 min plating appears to produce irregular surface morphology with a part of side-reacted contamination. The further decreased Au concentrations to 0.0052 and 0.0022 M deposited similar well-packed Au grains films. At 0.0052 M, the deposited Au film exhibits similar surface morphology despite of broad range of plating time from 5 min to 20 min. Based on this observation, the chemistry of Au solution was determined to be 0.0052 M for scalable CF-EL plating.

Table 3.2 compares the surface morphology of EL film with varying hydraulic condition via increasing flow rate. The hydraulic condition was evaluated by Reynolds number because of various dimensional flow cells. The dimensionless Reynolds number ($N_{Re}=Qd_H/(vA_c)$) Q = volumetric flowrate, d_H = hydraulic diameter, A_c = cross sectional area of flow cell) can be used to determine hydrodynamic similarities between different experimental cases. For a Reynolds number of 0, in other word, BI-EL plating, the deposited film appears to form nucleated NP for 1 min. As increasing to 2 min, the nucleated NP film grows to discontinuous island structure. Further deposition to 5 min and 10 min, BI-EL plating produce well packed continuous Au film. At 0.13 Reynolds number, 1 min CF-EL plating appears to produce similar nucleated NPs, but its density and size are higher than 1 min BI-EL film. Interestingly, the 2 min CF-EL plating produce more continuous thin film relative to 2 min BI-EL film. At higher 0.66 Reynolds number, the intermediate plating time produce well packed continuous Au grains films. The steady higher mass transfer of CF-EL plating produce more continuous EL Au film at short time plating while intermediate plating time for > 5 min produce similar surface morphology.

Table 3.2. Flow rate effects in EL Au plating (BI-EL *vs* CF-EL plating).

Substrate: silicate glass, Plating Au Concentration :0.0052M

Re \ Time	1 min	2 min	5 min	10 min
0 (batch)				
0.10				
0.13				
0.66				

Scale bar =200 nm

3.5 Conclusion

In summary, the developed novel continuous flow plating system allows fabrication of more uniform thin film relative to BI-EL film. The CF-EL plating is applicable to fabricate advanced Au nanostructure by integrating with EBL. The scalable CF-EL thin films are fabricated by a novel automated CF-EL system. The time-resolved optical features are successfully measured in this system. The more optical and physical characterization of fabricated sample will be discussed in Chapter 4: Characterization.

3.6   Reference

(1) Jang, G.; Roper, D.K. *J. Phys. Chem. C* 2009*, 113,* 19228-19236.

(2) Blake, P.; Ahn, W.; Roper, D. K. *Langmuir* **2010**, *26(3)*, 1533-1538.

(3) Jang, G.; Hawkridge, M.; Roper, D.K *J. Mater. Chem.,* **2012**, DOI*:10.1039/c2jm34208a*

(4) Ahn, W.; Taylor, B, Dall'Asen, A.; D, K, Roper. *Langmuir.* **2008**, 24, 4174-4184.

(5) Wonmi Ah, Ph.D. Dissertation, Novel electroless gold nano-architectures to enhance photon-plasmon coupling, University of Utah, 2010

CHAPTER 4

4. Characterization of SPR Enhanced Au nanostructure and relevant materials

Various Au nanostructures, scalable thin films and thermal transformed random NP arrays, fabricated by a novel CF-EL plating system were characterized by microscopic and spectroscopic measurement. These Au structures exhibit improved surface plamson feature due to enhanced surface uniformity. The quantitative Au(I) characterization method was developed by using balancing redox activity of Au(I) via control of reductant, oxidant, and indicative color reagent. This simple, straightforward method improves the limit of detection (LOD) which is comparable to more elaborate analytical instrument. The real time T-UV measurement built in the automated scalable CF-EL plating system allow time-resolved characterization of transitory EL thin film growth regimes and physicochemical surface, internal and interface structure of Au film on silicate substrate. The characterized optical kinetics during Au deposition validates the mass transfer limited EL Au reaction. The developed mass transfer correlations allow precise control of structural dimension design at the nano-scale.

This chapter is organized as follows: Section 4.1 describes characterization of uniformity enhanced Au thin film and thermal transformed NPs using microscopic and spectroscopic measurements correlated with mass transfer models. Novel spectrophotometric characterization method of detecting Au(I) ion concentration for EL Au deposition is described in Section 4.2. Noble metal disposition and dynamics during EL metal thin film synthesis are depicted by time-resolved spectroscopic and microscopic measurement in Section 4.3. The kinetics of Au film growth and its mass transfer interpretation are illustrated in Section 4.4.

4.1   Characterization of uniformity enhanced EL Au thin film[*]

4.1.1   Significance of this work

This study examines a novel CF method for EL plating that deposits uniform, continuous Au thin films with improved physical and optical properties. CF-EL films with different flow-rates are compared with BI-EL films fabricated by increasing immersion times. Physical surface morphology of CF and BI-EL films is evaluated by SEM and AFM. PL features characterized by T-UV spectra show that CF-EL films are more opaque and less dispersive in spite of shorter plating times. The extinction spectra of NP ensembles, transformed from CF and BI-EL films by successive heating, exhibits enhanced LSPR extinction peaks compared to BI-EL. SEM image analysis of NP sizes and particle densities of the ensembles shows that CF-EL NP ensembles exhibit a more monomodal particle size distribution, resulting in enhanced LSPR extinction spectra compared to BI-EL NP ensembles. A mathematical model for mass transfer in CF-EL plating shows steady state deposition driven by the higher transport driving force increases the total number of Au ions accumulated on the substrate, which correlates with improved film morphology and optical features including PL, SPR, and LSPR spectra.

4.1.2   Experimental Characterization method

T-UV spectroscopy, SEM and AFM were performed to characterize fabricated EL Au thin films and their thermal annealed NPs. The detailed procedures are described in the published paper.

4.1.3 Characterization Results

4.1.3.1. Improved microscopic and spectroscopic feature of CF-EL Au thin films

The CF-EL plating deposits Au films that exhibit increased continuity and uniformity relative to BI-EL as measured by SEM and AFM shown in Figure 4.1.1. The plating conditions of CF-EL films are 2+1 min (CF plating + incubation) with injection flow rate of 800 μL/hr, whereas the BI-EL film was fabricated by immersion followed by 4 min incubation. Theoretically, the deposited mole amount calculated by mass transfer models is similar for both methods. The 2D AFM images show that the CF-EL film's surface morphology is formed by uniformly close-packed island structures whereas the BI-EL film exhibits wide-ranging peaks and crevices. The cross-sectional profiles shown below the AFM images compare uniformity and smoothness of CF-EL and BI-EL films. CF-EL film has an average total roughness of 0.64 nm, compared with 0.97 nm for BI-EL film. The surface morphology shown in the AFM image and the SEM image (Figure 3.2A) are in good agreement.

The transmission peak around 480 nm is a PL peak which is directly related with the surface roughness. The PL feature is primarily caused by electron transitions from the top *d*-band to the Fermi-level conduction band followed by radiative recombination as well as collective optical absorption induced by SPR coupling inside cavities and between surfaces on both sides of the island structures.[1,2,3] PL at ~500 nm increases with increasing thickness for films less than 60 nm, but PL decreases when increasing film thickness over 60 nm.[4] A smooth surface not only diminishes scattering, but also narrows the PL feature.[5] The phenomenon is especially observed at energies lower (e.g., longer wavelengths) than the interband adsorption edge. Evaporation plating is capable of developing less rough surface than sputtering deposition. The PL optical density at ~500 nm of evaporated Au thin films are 5 times lower than rough, sputtered 20 nm
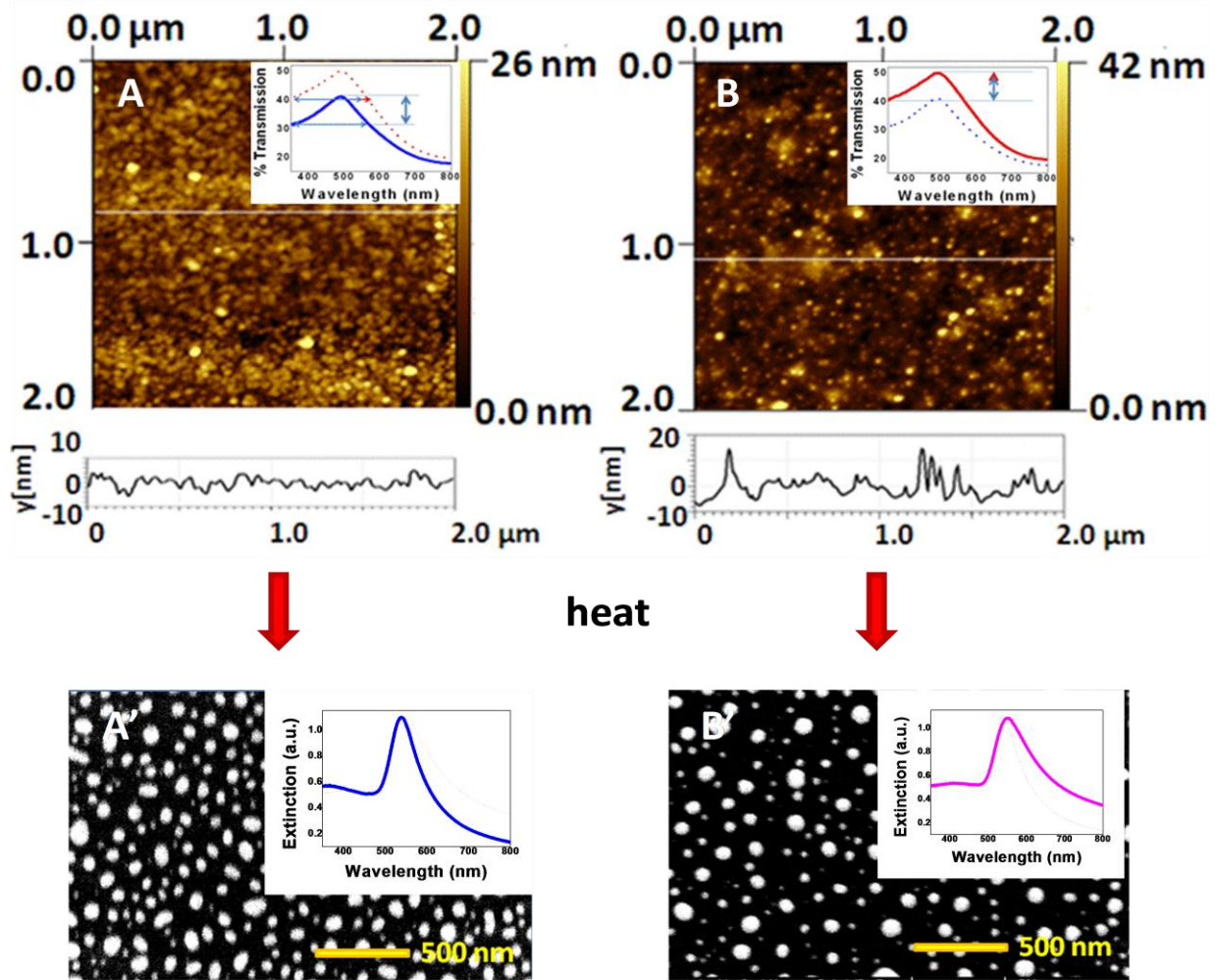
Figure 4.1.1. Microscopic/spectroscopic comparison between CF-EL nanostructure, A, and BI-EL, B. A, B and A', B' are AFM and SEM images, respectively. Cross-sectional diagram below AFM image represent the roughness of both films. The NPs in A' and B' are thermally transformed from deposited film structure. Insets are transmission (film) and extinction (NP) spectra.

Au films.[6] It is reported that PL intensity of sputtered Au films sharpen and decrease in intensity as sputtering time increases to yield more uniform and smooth films, while EL Au plating forms more rough morphology as deposit time increases.[5]

Furthermore, the SEM images of thermally transformed NPs show that the CF-EL particle size is more uniform and its particle distribution density is higher than BI-EL. CF-EL extinction spectra from thermally transformed NPs exhibit higher PH and narrower FHWM – enhanced LSPR than NPs transformed from BI-EL films. This is due to the more uniformly formed NP and higher particle density.

4.1.3.2. Quantitative microscopic feature of EL NPs

CF-EL films yield larger particles at comparable densities than BI-EL at comparable plating times. The extinction maxima and intensity of LSPR absorption bands of metallic nano-island films are sensitively affected by the particle size, size distribution, and densities, as well as by the surrounding conditions.[7] Figure 4.1.2. shows particle size distributions determined by the image analysis from inset SEM images for 800 °C heated EL Au films. BI-EL NP ensembles of 1, 2, and 4 min and CF-EL 800 (flow rate 800 mL/hr) NP ensembles are shown in Figure 4.1.2A. Figure 4.1.2B shows BI-EL 6 min NPs ensembles, Ahn[5] and CF-EL 1000 (1000 mL/hr) NPs. BI-EL films of Figures 4.1.2.A and B show that as immersion time increases from 1 to 2 to 4 to 6 min, average particle diameters produced by successive annealing and heating change from 13.8 ± 6.2 to 19.6 ± 8.7 to 35.6 ± 14.6 to 48.6 ± 23.2 nm, particle densities changes from 1163 to 654 to 173 to 87.6 counts per μm^2, particle distances (center to center) change from 20.1 to 28.7 to 56.7 to 78.5 nm. Increasing deposition time enlarges Au NPs size and broadens the size distribution and distance between particles. CF-EL films of Figure 4.1.2.A and B show that as
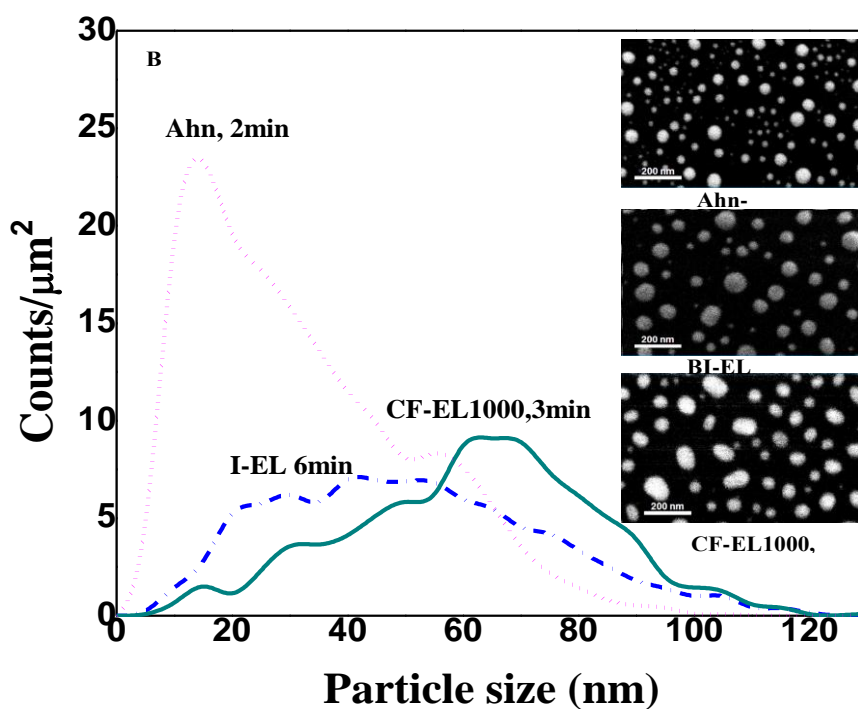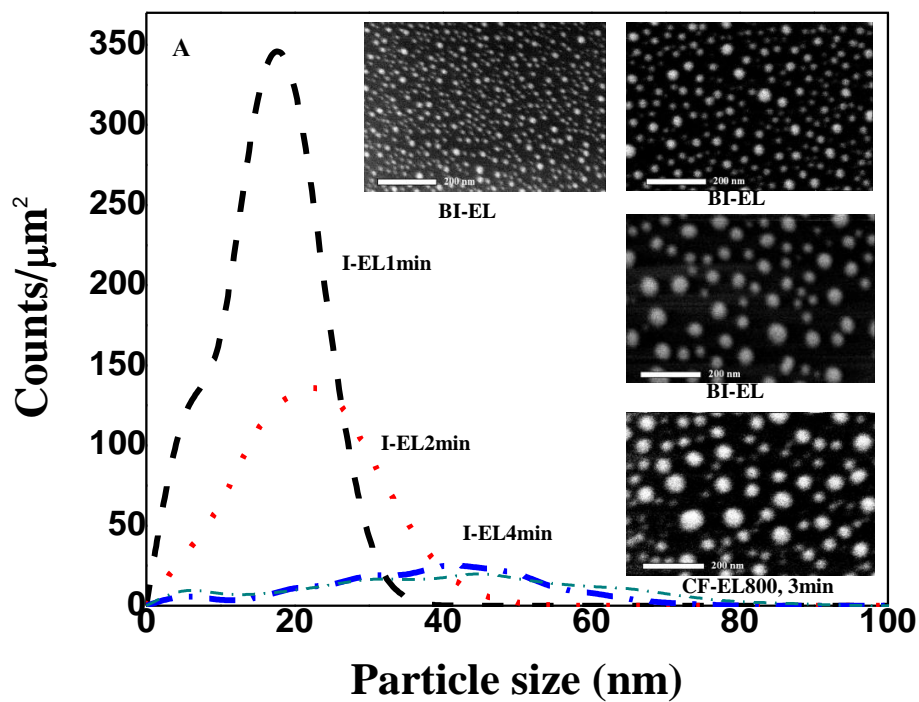
Figure 4.1.2. Distributions of NP diameters acquired from SEM images of Au films annealed at 350˚C for 3hr, followed by annealing at 800˚C for 30 min. (A) Shows BI-EL 1 min, BI-EL 2 min, BI-EL 4 min, and CF-EL 800 (2+1 min) (B) Shows Ahn[5] (2 min), BI-EL 6 min and CF-EL 1000 (2+1 min).

the flow rate increases from 800 to 1000 μl/hr, average particle diameters produced by successive heat treatment increased from 38.5 ± 19.4 to 54.6 ± 21.2 nm, particle density decreased from 190 to 89.3 counts per μm^2, particle distances (center to center) change from 51.7 to 82.4 nm. This result suggests increasing flow rate enlarges Au NPs and broadens the size distribution and distance between particles as seen in BI-EL. Even though overall CF plating time is only 3 min, particle size and density of CF-EL 800 are higher than BI-EL 4 min and CF-EL 1000 is higher than BI-EL 6 min. The total number of Au ions deposited on the silica substrate in CF-EL 800 and 1000, respectively, appears to be higher than 4 min and 6 min BI-EL. Even though the average particle size of CF-EL 1000 (54.6 ± 21.2 nm) is much larger than that of BI-EL 6 min (48.6 ± 23.2 nm), the size distribution in figure 4.1.2.B shows not only clear better monomodal NP distributions, but also a lower standard deviation, indicating the surface morphology of CF-EL1000 film is more uniform than BI-EL 6 min film. The reference particle size (Ahn) is much smaller than CF-EL films. We attribute the higher peak intensity and narrower FWHM of CF-EL 1000 extinction spectra compared to BI-EL 4 min and BI-EL 6 min to the significantly higher number of NPs in the range of 60~100 nm. The monomodal NP distribution for CF-EL transformed films enhances the LSPR.

4.1.3.3. Correlation of optical features and mass transfer model

CF-EL enhances Au deposition relative to BI-EL plating. Mass transfer rate in CF plating is enhanced due to steady, laminar introduction of fresh bulk Au solution. Based on derived models, the total number of deposited Au ions on a wall may be calculated for each plating condition and incubation time. The calculable scaled value of the total number of deposited Au moles, $M_{Au}/(A\Delta C_{Au})$, shown on the x-axes of Figure 4.1.3. was obtained by rearranging
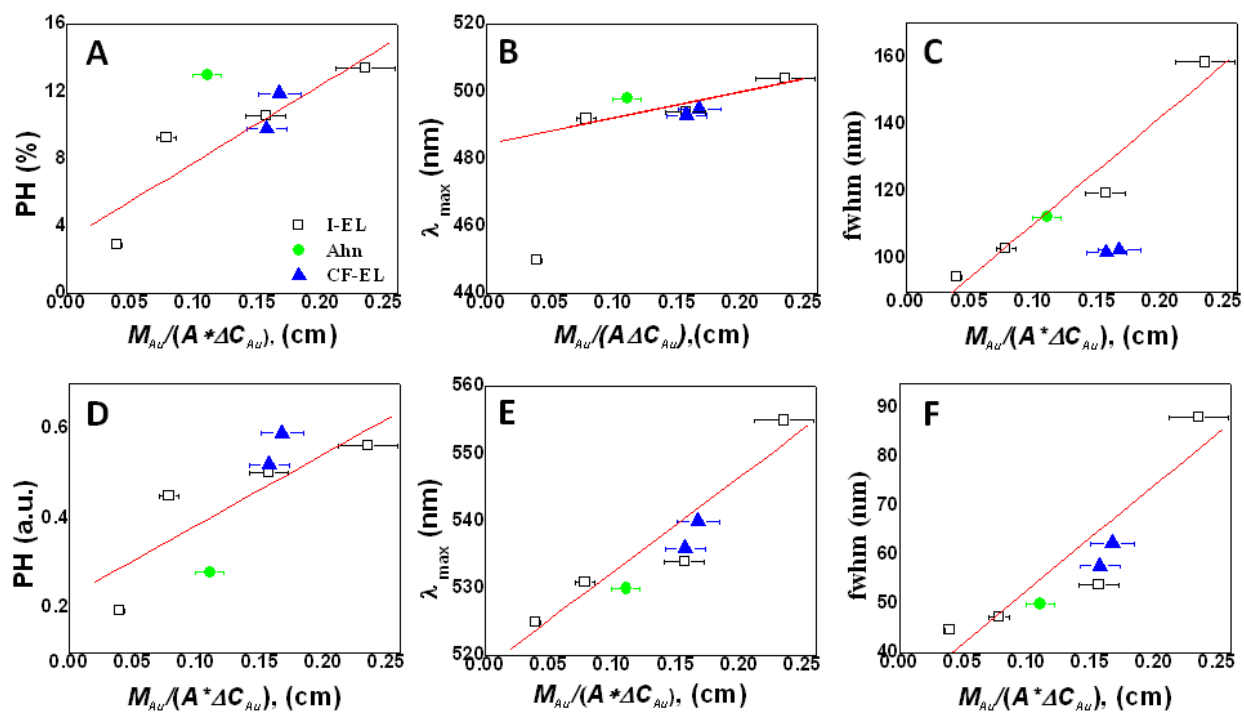
Figure 4.1.3. Variation of optical features – PH (A,D), λ_{max} (B,E), and fwhm (C,F) -- with increasing time-integrated mass transport coefficient ($M_{Au}/A\Delta C_{Au}$) from T-UV of thin Au films (A,B,C) and thermally-transformed Au NP (D,E,F). Data are for BI-EL (open squares), CF-EL (solid triangles) and Ahn[5] (open circle). Lines show linear least squares fit to BI-EL data. Measured PH, λ_{max}, and fwhm values increase in proportion to calculated Au deposition values. The least squares fit for Fig 4.1.3B excludes the BI-EL 1 min data point for λ_{max} which is not clearly distinguishable.

Equations (2.2) and (2.6) in Chapter 2 to obtain a time-integrated mass transfer coefficient. The infinite-dilution diffusion coefficient (D_{AB}) of Au ions in aqueous solution is estimated by the Nernst-Haskell equation.[8] The calculated Au ion diffusivity is 1.063×10^{-5} cm^2/s. For BI-EL plating, the total number of Au ions transferred to the wall increases with the square root of immersion time. For CF-EL plating, the mass transfer rate is dependent on the flow rate, so the number of Au ions deposited increases in proportion to the incubation time, as well as increasing flow rate and decreasing capillary dimensions. Although overall plating time of CF-EL films was 3 min, the overall Au moles transferred for CF-EL films are more than BI-EL 4 min film. The calculated mass transfer rate of CF-EL 1000 over 30 s is $78.3 \pm 1.6\%$ higher than BI-EL plating for each 30-second interval. This is due to enhanced mass transfer rate and the steady-state diffusion condition.

Optical features of transmission T-UV of CF-EL and BI-EL Au films are consistent with models for mass transfer of Au mole deposition. Optical properties of CF-EL and BI-EL films measured by *transmission* T-UV in Figure 4.1.3A to C change linearly in proportion to the total number of deposited Au moles. PH, λ_{max}, and FWHM versus the scaled value of the total number of deposited Au ions, $M_a/A\Delta C$, are plotted in Figure 4.1.3. The total number of Au ions deposited via CF-EL 800 and 1000 is slightly more than the number deposited via BI-EL 4 min. Figure 4.1.3A and B show PH and λ_{max} of CF-EL films are close to BI-EL 4 min *because the number of Au ions deposited via mass transfer is comparable* for 4 min of immersion, via unsteady diffusion from a stagnant bulk (BI-EL), and for 2 min continuous flow, via steady deposition from an adjacent bulk in laminar flow followed by 1 min of stagnant incubation (CF-EL).

On the other hand, FWHM values are lower for CF-EL films than for BI-EL films with comparable numbers of Au ions deposited (Figure 4.1.3C). The lower values of FWHM suggest

that CF-EL 800 and 1000 are smoother than BI-EL 4 min and 6 min despite similar deposited total number of Au ions. Figure 4.1.3 showed that the values of % transmission at 350 nm of CF-EL 800 (31.3%) and CF-EL 1000 (25.7%) are much lower than BI-EL 4 min (38.3%), which might suggest that CF-EL films could be thicker than BI-EL 4 min. However, since the number of Au ions transferred is similar for CF-ELs and BI-EL 4 min, this suggests that the opaqueness is due to different deposition pattern. A steady high local concentration of Au ions in CF-EL plating appears to yield uniform, continuous, evenly packed Au deposits, while unsteady-state diffusion of BI-EL plating, yields relatively non-uniform, discontinuous, inconsistently packing structures as local Au concentration is depleted in proportion to $(time)^{1/2}$. One reason may be that the high mass transfer rate of CF-EL plating removes galvanically displaced Ag^+ ions from the surface at a faster rate, which may reduce effects of local variation in tin or silver content at the wall. Thus, both the steady state diffusion induced by the high concentration in the outer compartment of CF-EL plating and the rapid substitution between Au and Ag due to an enhanced mass transfer rate increase uniformity and smoothness of deposited Au.

Optical properties of *Au NP ensembles* that were thermally transformed from CF-EL and BI-EL films and measured by *extinction* T-UV in Figure 4.1.3D to F also change relatively linearly in proportion to the total number of deposited Au ions. Optical features repeated in Figure 4.1.3D, E and F are based on the extinction peak induced by LSPR of NPs. Figure 4.1.3D, E and F show that the PH, wavelength maximum and FWHM of CF-EL 800 are slightly higher than BI-EL 4 min. In particular, note that the PH of CF-EL 1000 exceeds BI-EL 6 min while the FWHM is much smaller. We hypothesize that although the total number of transferred Au ions of BI-EL 6 min is higher than CF-EL 1000, the rough and inconsistent deposition results in a wide size distribution of NPs which deteriorate LSPR intensity and sharpness. The steady state deposition

in CF-EL 1000 with high uniform concentration develops more uniform and smooth packed deposition structures which are transformed to more monodisperse distributed particles compared to BI-EL 6 min. The uniformity of NP ensembles improves LSPR extinction spectra, such as enhanced peak intensity and narrow peak width.

4.1.3. Conclusions

A method to deposit uniform, smooth Au films via EL plating using a CF micro syringe system has been developed and characterized. SEM and AFM images of CF-EL films show Au films deposited via CF-EL plating exhibit increased uniform and continuity relative to films deposited via BI, consistent with narrower FWHM and lower PH for CF-EL films, measured by T-UV spectroscopy. Successive heat treatment of CF-EL Au films yield NP with higher T-UV PH and narrower FWHM compared to NP from corresponding BI-EL films. Monodispersity and particle density of NP from CF-EL films measured via SEM is also increased relative to BI-EL NPs. Magnitudes of optical features [PH, FWHM, and resonant extinction wavelength (λ_{max})] increase in proportion to the time-integrated mass transfer coefficient for both batch and continuous plating systems, suggesting improved mass transfer rate, which yields a steady, higher average local Au ion concentration during continuous plating, increases uniformity and continuity of EL Au films.

4.1.4. References

(1) Mooradian, A. *Phys. Rev. Lett*. **1969**, 22, 185-187.

(2) Boyd, G. T.; Yu, Z. H.; Shen, Y.R. *Phys.Rev. B* **1986**, *33*, 7923-7936.

(3) Xiao, M.; Rakov, N. *J. Phys. Cond. Matter* **2003**, 15, L133-L137.

(4) Kim, J.H.; Moyer, P.J. *Opt. Expr*. **2006**, 14, 6595-6603.

(5) Ahn, W.; Taylor, B, Dall'Asen, A.; D, K, Roper. *Langmuir.* **2008**, 24, 4174-4184.

(6) Lin, H. Y.; Chen, Y. F. *Appl. Phys. Lett* **2006**, *88,* 101914/1

(7) Hutter, E,; Fendler, J.H. *Adv, Mater*. **2004**, *16*, 1685-1706.

(8) Seader, J. D.; Henley, E. J. *Separation Process Principles.* 2nd Ed. (John Wiley and Sons, Inc.2006).

4.2   Quantitative detection of Au(I) concentration for EL Au deposition[*]

In this chapter, a novel spectrophotometric detection method is developed to measure low Au(I) concentration for application of EL Au deposition. The importance of ionic Au characterization is described in Section 4.2.1. The novelty of this work is summarized in Section 4.2.2. Summarized experimental methods for balancing redox activity of Au(I) as a color indicator of Tetramethylbenzidine Dihydrochloride (TMB) are described in Section 4.2.3. The mechanism of balancing redox activity and its correlated sensitivity improvement are described in Section 4.2.4. In Section 4.2.5 future work is addressed with a concluding statement.

4.2.1.   Importance of ionic Au characterization

Au(I) compounds have attracted recent interest due to their unique biological activity[1] and their industrial utility as catalysts and as oxidation agents in EL plating.[2] For instance, Au(I) phosphine complexes have been studied to treat breast cancer[3] and to catalyze oxidation of CO gas.[4] EL plating of Au(I) from aqueous solution has been used to fabricate solid-state islands, films, and particles of Au(0).[5-9] A method to measure Au(I) concentration *in situ* quantitatively and dynamically would be useful to characterize and control Au(I) content in EL plating, catalysis, and *in vivo* therapies, just as several analytic methods have been employed to analyze Au(III) and Au(0) content in various applications. Instrumental methods to determine Au(III) content in aqueous and geological samples after thermo-chemical pretreatment were reviewed by Barefoot (1999).[10] These include atomic absorption spectroscopy (AAS), atomic emission spectroscopy (AES), inductively coupled plasma mass spectrometry (ICP-MS), voltammetry, as well as hyphenated (e.g. ICP-AES) approaches. Spectrophotometric methods to determine Au(III) in aqueous solution using color reagents were summarized by Zaijun (2003)[11] and by Kamble

(2010),[12] who reviewed new synthetic reagents for spectrophotometry of Au(III). Techniques to measure Au(III) have also been used to quantatively determine Au(0) concentration in NPs: MS,[13] direct amperometric methods,[14] fast-scan cyclic voltammetry,[15] ICP-MS,[16] and UV-vis spectroscopy.[17,18] These techniques are supplemented by particle counting[19] to characterize distributions of NP populations. While it is possible to distinguish between various ionization states of Au using MS, extension of facile spectrophotometric methods to quantitatively measure Au(I) or to distinguish Au(0), Au(I), and Au(III) has not been reported.

4.2.2. The novelty of the present work

This work introduces a direct spectrophotometric method to quantitatively determine Au(I) concentration in acidic aqueous solutions by balancing redox activities of a strong reductant (formaldehyde, HCHO) and a strong oxidant (*N*-bromosuccinimide, NBS). The reductant and oxidant are added successively, in varying amounts, to a solution of Au(I), which is then exposed to an oxidizable color reagent (3,3',5,5'-tetramethylbenzidine dihydrochloride, TMB). At low reductant levels, NBS oxidizes Au(I), which linearly suppresses subsequent oxidation of TMB by NBS to its distinctive blue charge-transfer complexes of diamine and diimine.[20] At high initial HCHO reductant levels, Au(I) is reduced to Au(0),[21] then subsequently oxidized to Au(III) by NBS.[22] Upon addition of TMB, Au(III) is reduced to Au(0) accompanying oxidation of TMB to its spectrophotometrically detectable blue complexes, facilitated by the high HCHO level. This note identifies levels of reductant, oxidant, and colorimetric agent which allow quantitative measurement of Au(I) to detection limits (LOD) of 0.0025 and 0.05 mgL^{-1} using low and high levels of reductant, respectively. Defining this straightforward spectroscopic method that uses commercially available redox reagents to measure Au(I) without surfactants or

organic solvents permits rapid, accurate, and sensitive detection of Au ions for applications such as electroless plating, catalysis, and in *in vivo* therapies.

4.2.3. Experimental Method

Scheme 4.2.1 shows the procedure to determine Au(I) content in aqueous solutions at high and low values of the reductant HCHO by subsequent addition of NBS, adjustment of pH to 3.00, and addition of TMB color indicator which is monitored spectroscopically. This procedure was used to generate data shown in Figures 4.2.2 and 4.2.3 in which spectral peak heights of TMB were measured at 370 nm. The detailed procedure is described in the published paper.

4.2.4. Results and Discussion

4.2.4.1 pH-dependent feature of the colorimetric reagent TMB.

The modest oxidation potential of TMB and its unique fluorescence and colorimetric features have made it valuable for analysis of nitrophenols,[23] various heavy metals such as Cr(VI)[24] that have high reduction potentials, and trace Au(III) levels in natural sea water.[25] Two differently-colored oxidation products of TMB may be obtained in aqueous solution, depending on pH,[20] as illustrated in Figure 4.2.1. The single-electron oxidation product obtained at pH~3 consists of a blue charge-transfer complex of the parent diamine and diimine which exists in rapid equilibrium with the radical cation. This blue charge-transfer complex exhibits two peaks at 370 and 652 nm, respectively, in the UV-visible wavelength range. The two-electron oxidation product obtained at pH<2 is a diimine complex that exhibits yellow color at $\lambda_{max} = 458$ nm. It has been reported that oxidation of TMB by Au(III) forms a yellow diimine product which absorbs strongly at 458 nm (1.1×10^4 $cm^{-1}mol^{-1}L$).[25] In this note, the blue charge-transfer complex of
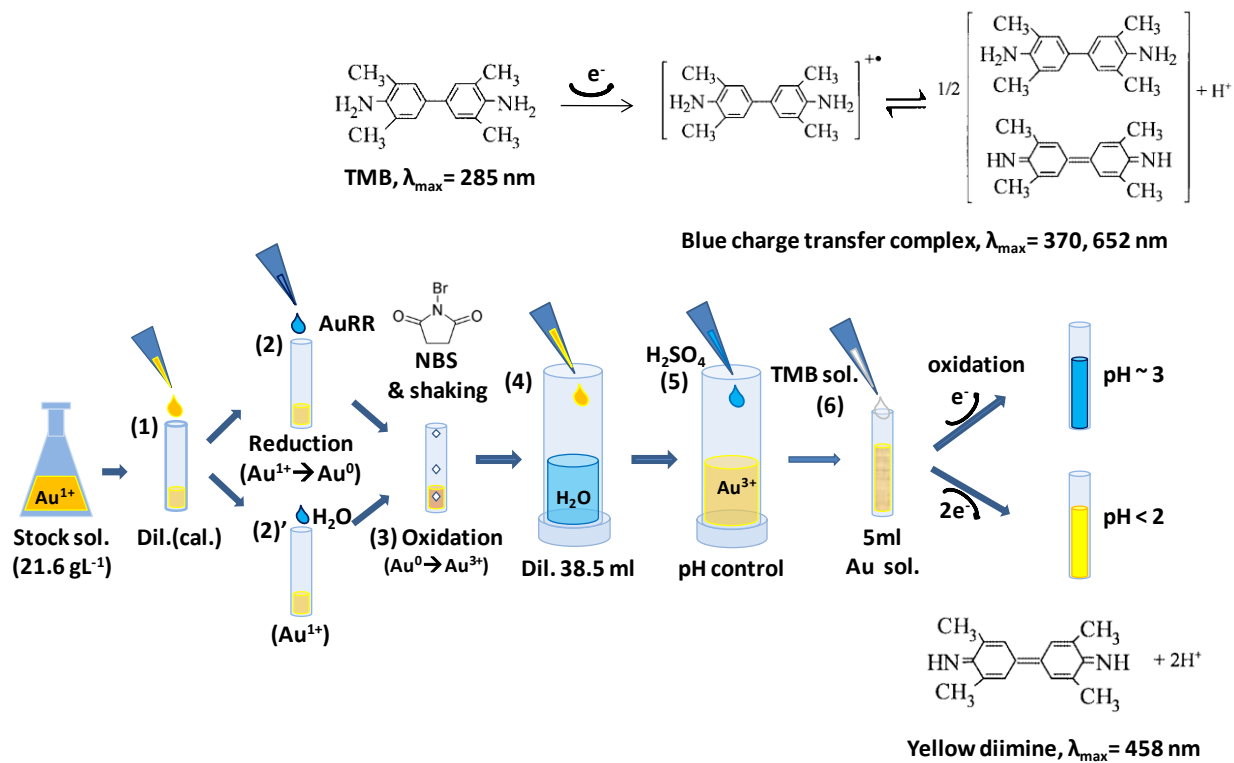
Figure 4.2.1. The basic procedure of determination Au(I) content in TMB aqueous solution at high and low molar ratio of reductant HCHO and oxidant NBS. Au reducing reagent (AuRR) is a mixture of HCHO and Na_2SO_3.

oxidized TMB is detected, rather than the previously reported yellow oxidation product[25] in order to improve the sensitivity and range of Au ion detection. In this work it was found that the first charge-transfer complex at λ_{max}= 370 and 652 nm was stable at pH 2.0 ~ 3.5 with a molar absorption coefficient of 6.17×10^4 cm^{-1}mol^{-1}L at 370 nm, which is approximately 6 times higher than the yellow diimine state which was previously used as a reference. Figure 4.2.3 shows that using the pH-stabilized blue charge-transfer complex extended the linear Au(III) detection range to between 0.025 and 4.0 mgL^{-1}. The previous range reported using the yellow diimine complex was from 0.1 to 2.0 mgL^{-1}. Furthermore, the LOD obtained by detecting the blue complex was 0.025 mgL^{-1}, lower than the value of 0.05 mgL^{-1} reported for the diimine reference complex formed at pH<2.[25]

4.2.4.2 Effect of redox-dependent Au(I) to TMB oxidation

The redox-dependent ability of Au(I) to affect spectroscopically-detectable oxidation of TMB is the basis for the proposed method. Au(I) alone does not oxidize TMB to blue charge-transfer complex in aqueous solution in spite of its large reduction potential (E^0 = +1.68 V) relative to that of Au(III), (E^0 = +1.50 V). This happens in spite of modest reduction potentials reported for TMB in acetonitrile (~0.1), in methanol/benzene mixtures (~0.7), and in voltammogram simulation (0.254), which suggests that TMB should be oxidizable via reduction of Au(I) alone. However, in the presence of a stronger oxidizing agent NBS (E^0 > 1.68 V), Au(I) reduces oxidation of TMB by NBS due to preferential oxidization of Au(I) in solutions with low to moderate reducing power. This is illustrated by the decreasing absorbance values at 370 nm in section I of Figure 4.2.2, where the mole ratio of HCHO to NBS is less than 7. In solutions where reducing and oxidizing power is balanced, low to moderate levels of Au(I) result in oxidation of TMB in a time-dependent manner after Au(I) has been reduced to Au(0) and
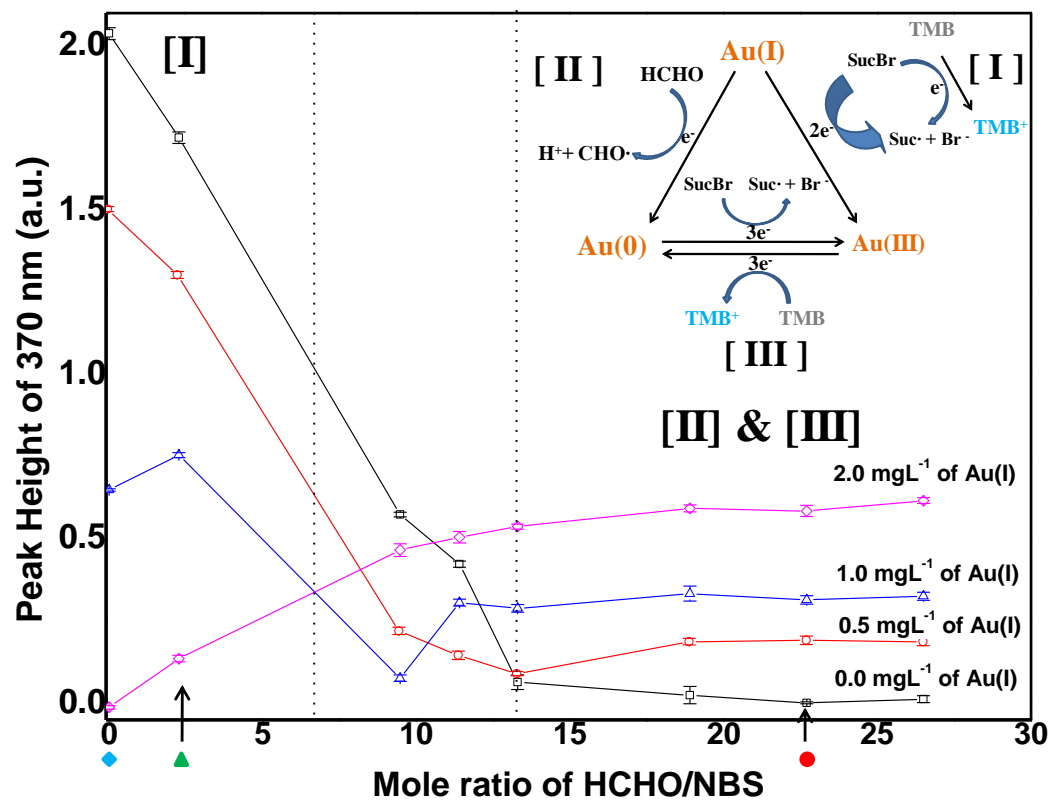
Figure 4.2.2. The Au(I) is quantitatively detected by effect of TMB oxidation in various mole ratios of HCHO/NBS and its association with Au(I). The error bars represent the standard deviation of peak variation (n=8) after mixing from 30 min to 60 min. The inset figures are suggested mechanisms of Au(I) detection in the matrix of Au, HCHO, NBS (SucBr) and TMB. (Solid blue diamond, solid green triangle and solid red circle represent each calibration curves in Figure 4.2.3.)

subsequently oxidized to Au(III). This is illustrated by the increasing absorbance values at 370 nm in section II/III of Figure 4.2.2, where the mole ratio of HCHO to NBS is greater than 13.

The method described herein identifies molar ratios of strong reducing agent HCHO and strong oxidizing agent NBS which are balanced with levels of Au(I) to allow quantitative, spectroscopically-detectable oxidation of color reagent TMB to its blue charge transfer complex. The capacity of Au(I) to kinetically modulate oxidation of TMB in the presence of selected values of HCHO and NBS was quantified by examining colorimetric products obtained from combining mixtures of each redox reagent alone, and in various combinations, with an aqueous solution of the TMB color reagent.

4.2.4.3   Effect of molar ratio of HCHO to NBS on determining Au ion content.

The quantitative effect of Au ions on spectrophotometric oxidation of TMB depends on the HCHO/NBS mole ratio. NBS is strong enough to completely oxidize both Au(0) in NPs to Au(III) ions[22] and TMB to blue charge transfer complex due to its strong positive reduction potential of succinimidyl radical ($E^0 > +1.83$ V (NHE)). The strong reducing reagent, HCHO ($E^0 = -1.07 \sim -3.00$ V; -1.07 (SHE), ~-3.00 (KOH/KCl)), can suppress the oxidation of TMB by NBS. Figure 4.2.2 shows that at a molar ratio of HCHO/NBS=0, 3 mg of NBS oxidized TMB to its blue complex resulting in a peak height (PH) at 370 nm above 2.0. As the HCHO/NBS mole ratio increased, the PH of 0 mgL^{-1} Au decreased, ultimately reaching 0 above a molar ratio of 18.9.

A value of 3 mg of NBS was selected after observing that at a level of 0.0 mgL^{-1} of Au(I) in Step 1 of the procedure, when 600 µL of stock HCHO solution was added at Step 2, as shown in Figure 4.2.1, both 6 and 9 mg of NBS oxidized TMB to blue complex (observed

spectroscopically), whereas neither 1 nor 3 mg of NBS oxidized TMB to a measureable extent, which resulted in a transparent final solution at Step 6. This suggested that 3 mg of NBS oxidant was just balanced by 600 μL of stock HCHO reductant solution, so that the final mixture yielded no measurable oxidation of TMB.

The optimal molar ratio of HCHO/NBS = 22.7 for re-oxidized Au(III) was identified by holding 3 mg of NBS constant and varying the HCHO:NBS ratio from 0 to 26.5. Adding Au(I) oxidant at this defined HCHO:NBS ratio of 22.7 resulted in oxidation of TMB to its blue charge transfer complexes with a monotonic, essentially linear response function. Whereas, adding Au(I) under non-reducing conditions depleted the availability of NBS to oxidize the TMB completely. These PHs decrease monotonically as Au(I) content increases at molar ratios of HCHO reductant relative to NBS oxidant less than 7, as illustrated by a blue diamond (HCHO/NBS = 0.0) and a green triangle (HCHO/NBS = 2.27) in Figures 4.2.1 and 4.2.2. In contrast, at molar ratios of HCHO reductant relative to NBS oxidant greater than 13.3, these PHs increase monotonically, as illustrated by red circles (HCHO/NBS = 22.7) in Figures 4.2.1 and 4.2.2. At HCHO:NBS > 22.7, the range of values over which 370 nm peak height increased in proportion to added Au(I) ceased to become larger.

In Steps 2 and 3 of the procedure, as shown in Figure 4.2.1, Au(I) ions were reduced to Au(0) by adding HCHO, then oxidized to Au(III) by subsequent addition of NBS. This occurred before the solution was introduced to aqueous TMB. Interestingly, Au ion changed from a reducing agent to an oxidizing agent, depending on the HCHO content. In the non-reducing environment produced by no HCHO addition, Au was preferentially oxidized by NBS, which interfered with oxidation of TMB in a proportional fashion as initial Au(I) content increased from 0.0 to 2.0 mgL^{-1}. The range over which this low-reductant level mechanism appears valid is

identified as region I on the left hand side of Figure 4.2.2 and the suggested redox Mechanism I is shown in the inset of Figure 4.2.2. It is useful that the blue color of the TMB charge transfer complex is quantitatively regained with decreasing Au(I) ion, because this permits sensitive detection of dilute Au ion at an improved LOD. Increasing the molar ratio of HCHO/NBS to 11.4, decreases TMB oxidation at Au(I) $\leq$ 0.5 mgL^{-1} but increases it at Au(I) $\geq$ 1.0 mgL^{-1}. Further increasing the molar ratio of HCHO/NBS to 13.3 or above permits monotonically increasing oxidation of TMB by Au(I). This appears due to the reduction of Au(III), since a constant, approximately proportional relationship between amount of NBS oxidized and Au content occurs, beginning at ca. 18.9 mole ratio of HCHO/NBS. The range over which this high-reductant level mechanism appears valid is identified as region II/III on the right hand side of Figure 4.2.2, and the suggested redox steps II and III are shown in the inset of Figure 4.2.2. Between HCHO/NBS molar ratios from 7 to 13.3, the role of Au ion shifts from being preferentially oxidized, to that of an oxidizing agent, depending on Au concentration. This feature is attributed to the moderate reduction potential of TMB color reagent (E^0 = + 0.22 ~ 0.7 V) relative to HCHO (E^0 = -1.07 ~ -3.00 V), Au(III) (E^0 = +1.50 V), Au(I) (E^0 = +1.68 V), and NBS (E^0 > +1.83 V). The dual-mechanism behavior illustrated in Figure 4.2.2 allowed two distinct calibration curves to be employed to detect Au(I) using either low (0<2.27<7) or high (13<22.7) molar ratios of HCHO/NBS.

4.2.4.4   Calibration curve for ionic Au determination

Adjusting the redox potential balance in determining Au(I) content allows enhancement of the linear range of detection at high reductant levels, as well as improved LOD at low reductant levels. Figure 4.2.3 shows two Au(I) calibration curves at low reductant levels (blue diamonds, green triangles), one curve at high reductant level (red circles), and a reference curve
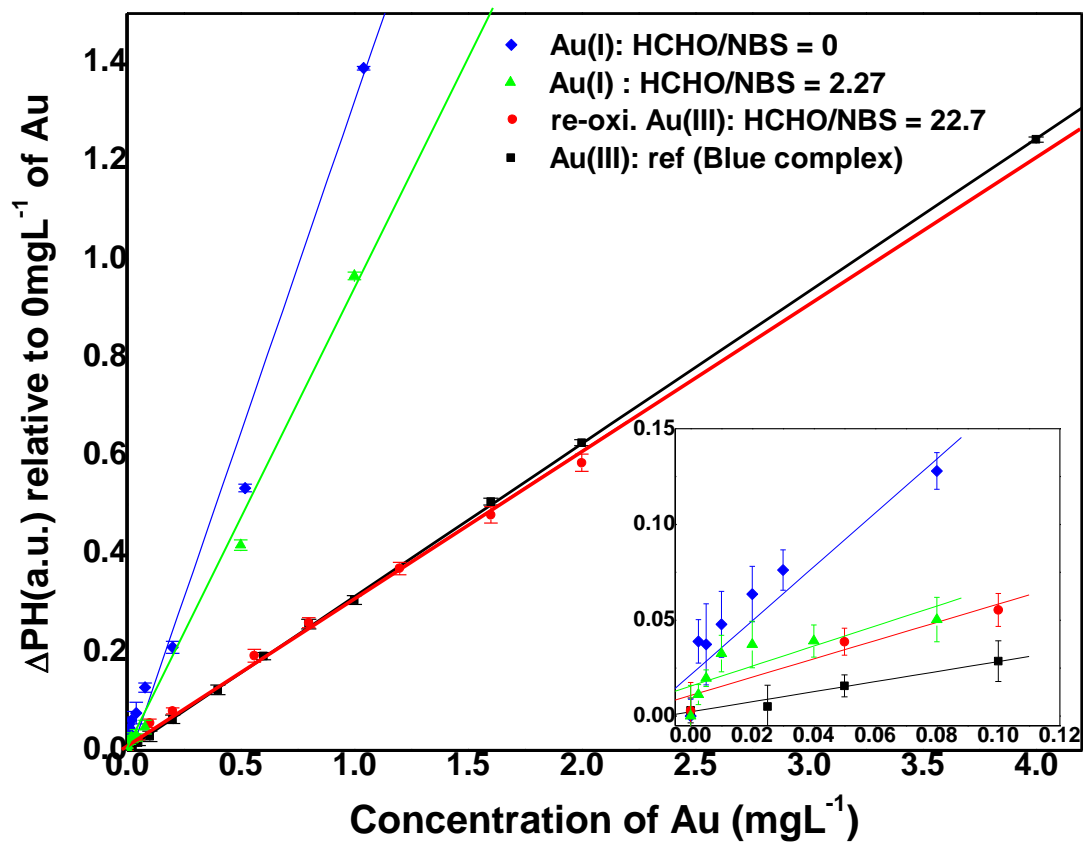
Figure 4.2.3. Balancing reduction potential improves the LOD of Au(I) determination. Comparison of calibration curves between Au(III) reference experimental result and re-oxidized Au(III) are well matched. The two Au(I) determination at low reluctant levels exhibit improved accuracy for detecting Au(I). The trend lines in inset are in the range of 0.00 - 0.10 mgL^{-1}

obtained using stock Au(III) solution (black squares). To ensure a valid comparison, the absorption data were collected every 3 minutes from 30 to 60 minutes after the reaction commenced. Direct measurement of Au(I) via interference with TMB oxidation by NBS at 0 mole ratio of HCHO/NBS (blue diamonds) yielded a Beer's law relationship over the concentration range of 0.005 - 1.00 mgL^{-1} (R^2=0.988) with a molar absorption coefficient of 2.75 $\times$ 10^5 cm^{-1}mol^{-1}L calculated by subtracting the peak observed at a particular concentration from the peak observed at 0.0 mgL^{-1} Au(I). The LOD was 0.0025 mgL^{-1}, a value lower than all but one previously reported method for colorimetric detection of Au(III).[25] The RSD calculated from 8 repetitions for determining 0.52 mgL^{-1} of Au(I) was 0.60%. The standard deviation of absorption values at low Au(I) concentrations from 0.005 to 0.08 mgL^{-1} were relatively higher than values in other systems. This was attributed to peak noise that occurred at low Au(I) concentrations which produced spectra near the maximum spectrophotometric UV absorption limit of 2.0. Increasing reducing agent HCHO to a mole ratio of HCHO/NBS = 2.27 (green triangles) decreased the measured UV absorption at 0.0 mgL^{-1} Au(I) from 2.0 to 1.70 and improved peak symmetry, both of which reduced the standard deviation. The linear concentration range in this case was from 0.01 to 1.00 mgL^{-1} (R^2=0.995) with a molar absorption coefficient of 1.91 $\times$ 10^5 cm^{-1}mol^{-1}L.

At high reductant levels typified by the optimized molar ratio of HCHO/NBS = 22.7, the re-oxidized Au(III) system obeyed Beer's law over a wider concentration range than at lower reductant levels: 0.05 - 2 mgL^{-1} (R^2=0.998). The molar absorption coefficient was 6.07 $\times$ 10^4 cm^{-1}mol^{-1}L. Interestingly, as shown in Figure 4.2.3, the calibration curve of the re-oxidized Au(III) matched well with the stock solution of Au(III). This supports a mechanism at this optimized high molar ratio in which initial Au(I) ions are reduced to Au(0) and then re-oxidized to Au (III).

4.2.5. Conclusions

Adjusting the balance of redox activity in acid solution allows sensitive spectrometric analysis of Au(I) via oxidation of the color reagent TMB. Methods were developed at both low and high reductant conditions which were simple, reproducible, and sensitive. The promising features of this novel approach are (i) improved LOD of 0.0025 mgL^{-1} at low reductant levels, which is comparable to more elaborate analytical instruments; (ii) improved linear detection range of 0.05 - 2.00 mgL^{-1} at high (balanced) reductant levels; (iii) ability to cross-check Au(I) content in different redox environments; (iv) potential to extend to the detection of other metal ion concentrations spectrophotometrically may be possible; and (v) the method is simple, straightforward and economical, since all key redox reagents are commercially available and readily available spectrophotometric determination obviates the need for expensive capital equipment. The proposed approach could also allow Au(I) to be distinguished quantitatively from Au(III) in solutions since the latter (but not the former) can be reduced in acidic aqueous solutions to oxidize TMB to its blue charge-transfer complex.

4.2.6. References

(1) Abdou, H. E.; Mohamed, A. A.; Fackler Jr, J. P.; Burini, A.; Galassi, R.; Lopez, J. M.; Olmos, M. E. *Coord. Chem. Rev.* **2009**, *253*, 1661-1669.

(2) Ali, H. O.; Christie, H. O. *Gold Bull.* **1984**, *17*, 118-127.

(3) Rackham, O.; Nichols, S. J.; Leedman, P.J.; Berners-Price, S. J.; Filipovska, A. *Biochem. Pharmacol.* **2007**, *74*, 992-1002.

(4) Kozlov, A.I.; Kozlova, A.P.; Asakura, K.; Matsui, Y.; Kogure,T.; Shido, T.; Iwasawa, Y. *J. Catal.* **2000**, *196*, 56-65.

(5) Menon, V.P.; Martin, C.R. *Anal. Chem.* **1995**, *67*, 1920-1928.

(6) Lee, S. B.; Martin. C.R. *Anal. Chem.* **2001**, *73*, 768-775.

(7) Ahn, W.; Taylor, B.; Dall'Asen, A. G.; Roper, D. K. *Langmuir* 2008, *24,* 4174-4184.

(8) Jang, G. G.; Roper, D. K. *J. Phys .Chem. C* **2009**, *113*, 19228-19236.

(9) Blake, P.; Ahn, W.; Roper, D. K. *Langmuir* **2010**, *26*, 1533-1538.

(10) Barefoot, R. R.; Van Loon, J. C. *Talanta* **1999**, *49,* 1-14.

(11) Zaijun, L.; Jiaomai, P.; Jian, T. *Anal. Bioanal. Chem.* 2003, *375*, 408-413.

(12) Kamble, G.S.; Kolekar, S.S.; Han, S.H.; Anuse, M.A. *Talanta* 2010, *81*, 1088-1095.

(13) Arnold, R. J.; Reilly, J. P. *J. Am. Chem. Soc.* **1998**, *120*, 1528-1532.

(14) Quinn, B. M.; Liljeroth, P.; Ruiz, V.; Laaksonen, T.; Kontturi, K. *J. Am. Chem. Soc.* **2003**, *125*, 6644-6645.

(15) Song, Y. Heien, M. LAV.; Jimenez, V.; Wightman, R. M.; Murray, R.W. *Anal. Chem.* **2004**, *76*, 4911-4919.

(16) Allabashi, R.; Stach, W.; Escosura-Muniz, D. L.; Liste-Calleja, L.; Merkoci, A. *J. Nanopart.Res.* **2009**, *11*, 2003-2011.

(17) Haiss, W.; Thanh, N.T.K.; Aveyard, J.; Fernig, D.G. *Anal. Chem.* **2007,** *79*, 4215-4221.

(18) Khlebtsov, N.G. *Anal. Chem.* **2008,** *80*, 6620-6625.

(19) Lenggoro, I. W.; Xia, B.; Okuyama, K. *Langmuir* **2002**, *18,* 4584-4591.

(20) Josephy, P. D.; Eling, T.; Mason, R. P. *J. Biol. Chem.* **1982**, *257,* 3669-3675.

(21) Richter, F.; Geseman, R.; Gierth, L.; Hoyer, E. *Ger, Dem. Rep. Pat.* DD 15 07 62 (1981)

(22) Singh, S.; Prasad, B. L. V. *J. Phys. Chem. C* **2007,** *111*, 14348-14352.

(23)Yang, R.; Wang, K.; Xiao, D.; Luo, K.; Yang, X. *Analyst* **2000**, *125,* 877-882

(24) Xiao, D.; Wang, K.; Xiao, W. *Analyst* **2001**, *126*, 1387-1392.

(25) Fazli, Y.; Hassan. J.; Karbasi, M-H.; Sarkouhi, M. *Mineral Engineering,* 2009, *22*, 210-212.

4.3   Metal disposition and dynamics during EL metal thin film synthesis

In this chapter, a novel real-time T-UV spectroscopy, SEM and XPS were used to characterize dynamic morphological and physicochemical disposition of metal during redox-driven self-assembly of EL metal thin film on silica surfaces under equilibrium and non-equilibrium hydraulic condition. Optical features consistent with LSPR, SPPs, and PL from Ag and related Au nanoarchitectures that included clusters, particles, and films were identified in time-resolved T-UV spectra obtained *in situ* using a novel EL metal deposition system. Kinetic changes in plasmon features suggested that four previously unrecognized time-dependent physicochemical regimes occur during consecutive EL deposition of Ag and Au onto tin-sensitized silica surfaces: self-limiting Ag activation; transitory Ag NP formation; transitional Au-Ag alloy formation during galvanic replacement of Ag by Au; and uniform metal deposition under controlled hydraulic conditions. Physicochemical features of Ag and Au at the surface, interior, and interface of the resulting thin metal films consistent with growth mechanisms inferred from real-time T-UV measurements were characterized by the depth profile XPS analysis. The importance of this work is described in Section 4.3.1. Summarized experimental characterization method is illustrated in Section 4.3.2. The revealed mechanism of metal disposition and dynamics during EL metal thin film growth is described in Section 4.3.3. In Section 4.3.4 future work is addressed with a concluding statement.

4.3.1   Significance of this work

Growth of uniform metal thin films with controlled thickness is vital for fundamental science and technical applications. Understanding film growth mechanism at the atomic scale provides a strong impetus for obtaining better control over the dynamics of process governing the nanoscale structure of as-deposited film. Technology of Au thin film deposition in aqueous

solution, specifically EL Au deposition, has been utilized to fabricate microelectrodes[1,2] and electronics[3,4] because of the simplicity of the operation (i.e., requiring no external source of current and no sophisticate equipment). However, although kinetics and thermodynamics of metal thin film growth via vapor phase have been extensively studied along with the advance of instrumental technologies controlling extreme conditions such as vacuum and high temperature, the study of metal ion diffusion for thin film formation at an atomic view in aqueous phase had not been investigated since 1990s due to less industrial and scientific demand resulting from limited scalability of bench bath system.[6] A fundamental mechanism of EL Au thin film growth and its control at a nano-scale view and internal and interfacial structure between substrates and Au films remain unclear because time-resolved characterization of transitory physicochemical features has not been performed.

4.3.2 Experimental Characterization method

Real-time T-UV spectral measurement was recorded in a 350–800 nm wavelength range during overall EL metal plating. D^3-H_2O filled Sn-sensitized flow channel cells were used as a reference blank spectra. Spectra were fit to Gaussian curves [Origin(Pro) 7.5, OriginLab Corp., Northampton, MA] to calculate relative peak height (PH) and the minimum extinction as a baseline offset, y_o. SEM was performed using a Philips XL-30 ESEM FEG (FEI, Hillsboro, Oregon). XPS data were acquired by using the PHI Versaprobe XPS (Physical Electronics Inc, Chanhassen, MN) equipped with a monochromated Al-Kα source (hν =1486.6 eV). The spherical capacitance analyzer was operated at a constant pass energy of 23.5 eV in fixed analyzer transmission mode with a take-off angle of 46.7°. Depth profiling was performed using an Ar^+ ion gun at 2 keV with a corresponding Au sputtering rate of 20 ~ 40 nm/min. Peak fitting was performed using the PHI Multipak program (Physical Electronics Inc, Chanhassen, MN).

Spin-orbit doublets were related using the appropriate area and separation relationships after applying a Shirley background correction.

4.3.3 Results and Discussion

4.3.3.1 Dynamics and disposition of Ag during EL Ag thin film formation

Ag reduction is light-sensitive and appears Sn^{2+}-limited. Figure 4.3.1(A) shows four T-UV spectra taken in real time during Ag reduction onto Sn-sensitized silica. The initial spectra (0s) show the surface is transparent prior to D^3-H_2O wash or Ag addition. The reduced-transparency three spectra were obtained during three subsequent periods identified in Figure 4.3.1(D): D^3-H_2O wash of Sn-sensitized silica (for 113 sec; no shading), Ag reduction (for 120 sec; red shading), and subsequent D^3-H_2O wash of Ag reduced on Sn (for 105 sec; no shading). The three representative spectra shown were captured at 120 s, 270 s, and 338 s after the initial wash began, respectively, or in other words 7 seconds after Ag reduction began, 37 seconds after Ag reduction ended, and at the point the 2nd water wash ended, respectively. The first two spectra were selected from spectra taken every 30 seconds during initial wash, silver reduction, and 37 seconds into the subsequent wash. Thirty-second intervals between T-UV measurements were necessary to minimize interference by *in situ* photochemical reduction of Ag ions on Sn^{2+}-driven reduction of Ag^+ onto the surface. Exposure to a broadband light source induces photochemical reduction of light-sensitive Ag ions to metallic Ag clusters in the presence of trace halide in solution. For example, photochemical reduction of Ag ions by UV exposure is a basis for light photography.[12] Experimentally, light-induced reduction of dissolved Ag ions was observed to preclude Sn^{2+}-catalyzed reduction of these ions onto the surface. Blackish powders, spots and irregular gray color that occasionally appeared on reduced-Ag substrates, even after reducing T-UV measurement intervals to 30 sec, was indicative of agglomeration of UV-reduced Ag
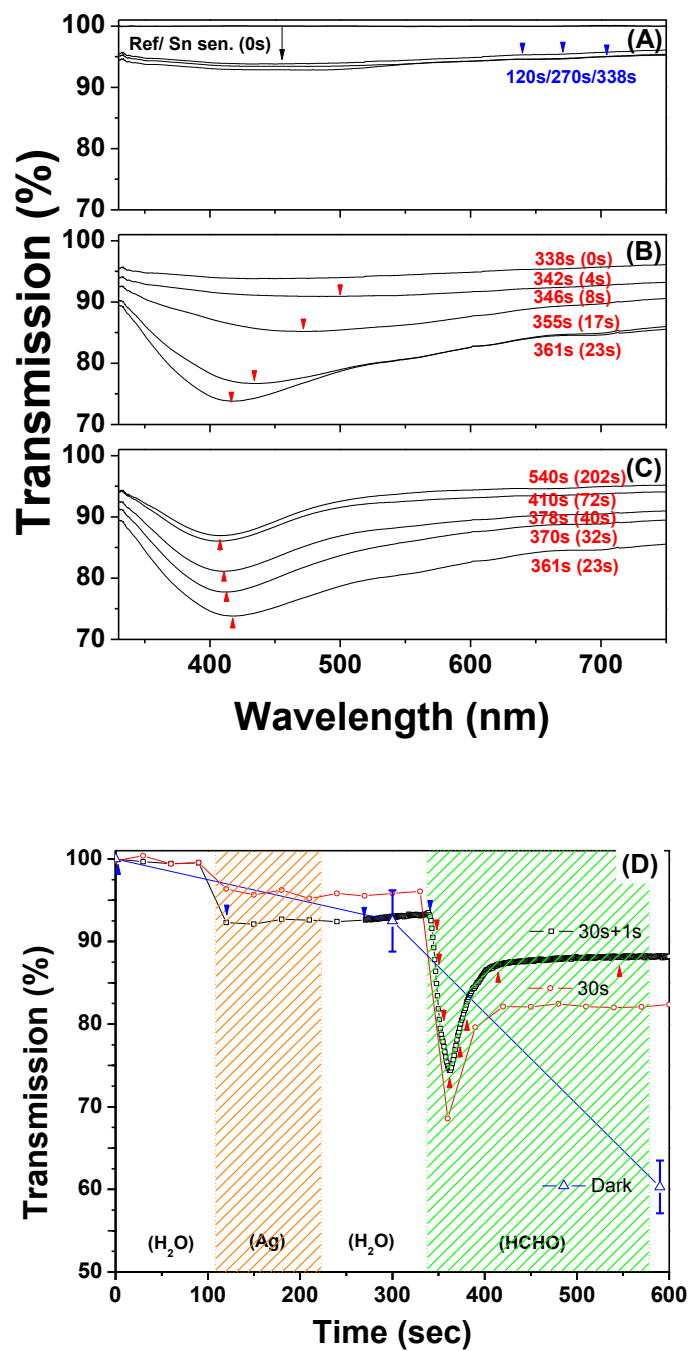
Figure 4.3.1 Real-time spectra monitored from Sn sensitization, through Ag activation, to Au reducing agent (HCHO) treatment at 3 ml/hr. (A) Ag reduction for 2 min (i.e. between 60 s and180 s) , (B) HCHO reductant exposure for 23 sec (i.e. between 308 s and 331 s) (C) HCHO reductant exposure for additional 2 min (i.e. between 331 s and 490 s) (4) Corresponding kinetic profile of % transmission at 425 nm (the Ag LSPR feature). Colored arrowheads on (D) shown when each spectra in (A-C) were taken.

clusters by attractive van der Waal forces and their association with free hydroxyl (-OH) group found on silicate glass.

The initial spectra at 0 sec in Figures 4.3.1(A) and (D) (corresponding black empty square profile) shows 100% transmission, as anticipated for Sn-sensitized silicate substrate corresponding to complete optical transparency in Figure 1.4.(A). The silica had been sensitized by dropwise addition of $SnCl_2$ solution followed by 10-min incubation. Subsequent T-UV spectra in Figure 4.3.1(A) show transmission rapidly changes from 100% for Sn sensitized surface to ~95% with a broad valley at ca. 500 nm at about 7 seconds after ammoniacal silver nitrate was introduced to the substrate. This appears consistent with a rapid formation of Ag island thin film illustrated in Figure 4.3.1(B). There was a volumetric holdup of ~89 μl in the injection system between glass syringes containing ammoniacal Ag solution and the spectroscopic flow cell (see Figure 3.5.). At the 3 ml/hr flowrate, this resulted in a theoretical lag of ~106 seconds. This corresponded to the 106 s period of initial water wash during which injected Ag solution flushed water out of the volumetric holdup.

To dynamically follow transformation of Ag thin film to Ag particles, Figure 4.3.1(D) plots three time-course profiles of % transmission values at 425 nm *only* vs. plating time throughout the pre- and post-silver reduction D^3-H_2O washes (no shading), Ag reduction (red shading), as well as subsequent exposure to aqueous HCHO reductant (green shading) with varying broadband light exposure time. Black empty squares (30s+1s) represent spectra measured at 30-second intervals during Ag reduction (120 sec) and 1-second intervals during HCHO treatment (240 sec). Measurements at 1-second intervals produced continuous broadband light exposure to the sample. Red empty circles (30s) profile spectra measured at 30-second intervals during the entire Ag reduction and HCHO treatment procedure. Blue empty triangles

represent average spectral values obtained at 300 sec (after Ag reduction; n=8) and 590 sec (after HCHO treatment; n=3) with no broadband light exposure, thus providing a negative control for exposure to broadband light exposure. Error bars show one standard deviation from the mean. At a wavelength of 425 nm, these dynamic profiles track the maximum wavelength of the LSPR feature for Ag NP. Colored arrowheads to black-squares in Figure 4.3.1(D) show when individual spectra in Figure 4.3.1(A-C) were taken. Spectra of data points that lack arrowheads are not shown in Figures 4.3.1(A-C), for clarity.

Significantly, the three profiles for 0 ~ 338 sec indicate that reduction of ammoniacal $AgNO_3$ to Ag island film at constant, equilibrium conditions provided by the continuous-flow conditions appears complete in $\leq$ 30 s. Further exposure to ammoniacal $AgNO_3$ did not discernibly decrease overall transmissivity or enhance Ag island film PL. This result, and the transmittivity of the resulting reduced Ag film, did not change appreciably with exposure to light at intervals $\leq$ 30 sec, within measured data error. Specifically, 2-min Ag activation in darkness (blue empty triangle at 300 sec) reduced transmission to 92.5±3.7 %, consistent with results obtained during 30-sec exposure intervals. Morphological effects during Ag reduction to Ag island film are limited due to fast, Sn^{2+}-limited redox reaction. More frequent exposure to light during Ag reduction induced visible formation of black powders, spots, and irregular gray color indicative of *in situ* photochemical Ag reduction and agglomeration of resulting clusters. A small change in overall transmission during a subsequent 105-s wash with D^3-H_2O, as shown in Figure 4.3.1(A), was attributable to replacement of the ammoniacal $AgNO_3$ solution by D^3-H_2O. Silver reduction onto Sn-sensitized silica to form Ag island film in the absence of external reducing agent appears limited by the availability of Sn^{2+} on the surface, in contrast to the previous

report.[15] Reduction of Ag redox-catalyzed by Sn-sensitizer apparently ceases when these electron donors are consumed despite a steady, continuous supply of Ag ions in the bulk

Exogenous reductant forms Ag NP from Ag film. Galvanic replacement of Ag by Au$^+$ conventionally occurs in the presence of the exogenous reductant, a mixture of sodium sulfate and HCHO. Formaldehyde (HCHO), a strong electron donor, has been used to reduce Au(I) to Au(0) as well as Ag(I) to Ag(0).[13,14] It was previously shown in our lab that aqueous Au ion can be shifted between +3, +1, or 0 oxidation states by adjusting the balance of HCHO reductant and N-bromosuccinimide oxidizing agent as indicated by a dissolved colorimetric reagent.[13] Reductant has been added to aqueous Ag$^+$ to deposit Ag island or NP on surface with varying reaction time and formulation,[15] but effects of reducing agent added to Ag film already reduced onto Sn^{4+} do not appear to have been investigated.

Figure 4.3.1, panels B and C show representative real-time T-UV spectra taken at 1-sec intervals during additional 68 sec D^3-H$_2$O wash and 202 sec exposure to formaldehyde (HCHO) reductant at 0.63 (M) molar concentration. Volumetric holdup (~60 μl) in the injection system between glass syringes containing HCHO solution and the spectroscopic flow cell (see Figure 3.5) produced a theoretical ~72 s lag at 3 ml/hr. Real-time transmission spectra in Figure 4.3.1(B) show that equilibrating the reduced Ag film with a continuous flow of HCHO-containing reductant decreases transmittance and briefly appears to enhanced thickness of the Ag island film, since the transmission minima remains near 500 nm. But in < 10 sec the minima blueshifted rapidly toward the LSPR of Ag NP (410 nm) and sharply drops between 338 s and 361 s. The transmittivity decrease and minima blueshift are attributed to dynamic Ag NP aggregation via reduction of active Ag ions remaining at the Ag island surface and/or produced by concomitant reduction from Sn(IV) to Sn(II). Mie theory predicts that an aqueous suspension of 50-nm

diameter Ag NP exhibits a LSPR at 410 nm,[20] while 15±10 nm diameter Ag NP thermally annealed from a 3-nm Ag island film, exhibit an absorption maxima at ~430 nm wavelength[10] which is similar to the spectra at 361sec. The high optical cross section of Ag LSPR contributes to an overall reduction in transmission.

Exogenous reductant with concomitant light exposure removes Ag from Sn^{2+}-sensitized surface. Prolonging exposure to reductant past 23 sec reverses the preceding dynamic: transmission increases and the LSPR feature slightly blue-shifts. Interestingly, Figure 4.3.1(C) and corresponding black square profile in Figure 4.3.1(D) shows that transmissivity rapidly recovers with continuous blueshifting of the LSPR minima from 410 nm to 405 nm during the first 49 sec after the reversal (between 361 s and 410 s). After 410 s, transmission increases only slightly for 130 sec (between 410 s and 540 s) and the transmission baseline stabilized to ~95%. During this regime, Ag film appears to leave the surface and larger particulates are ostensibly washed out of the spectroscopic field of view leaving behind smaller particles associated to the surface. This may occur concurrent with further HCHO reduction of Sn(IV) to Sn(II) at the substrate and continuous photochemical reaction due to exposure to broad band light source at 1 sec intervals. Mie theory suggests the transmission LSPR minima at ~400 nm correspond to ~40-nm diameter Ag NP.[20]

Exposure to light during HCHO reduction affects Ag nanoparticle morphology. Figure 4.3.1(D) shows that exposure to light at 1-sec (black squares) to 30-sec (red squares) intervals produces similar transmittivity profile features: a rapid decrease corresponding to fast NP formation followed by a slower recovery corresponding to NP disappearance. Decreasing or eliminating exposure to light substantially decreased transmittivity at 425 nm during and after HCHO reduction. The Ag LSPR of 30 sec interval exposure was stabilized the lower value of

~82 % compared to 92% for 1 sec interval exposure in spite of the higher initial transmissivity of the former sample. Complete darkness further reduced transmittivity to 60% after producing an optical profile similar to 30-second exposure at the conclusion of Ag reduction.

This result appears attributable to Ag NP self-association without light-induced erosion. Figure 4.3.2(A) is an SEM image of sample (corresponding blue triangle) after exposure to HCHO in dark. It shows the Ag island film from Figure 1.4(B) has been largely aggregated to spherical Ag NPs of diameter >100 nm. Individual NPs (inset lower LHS) are coated with ~10 nm Ag NPs that appear to nucleate at the surface of the larger particle core.. Application of such nucleated Ag NPs to thin film solar cells has been shown to improve light trapping effects.[21] This results from excitation of the dipolar and quardropolar plasmonics mode for longer wavelength due to large core and large angle scatters for shorter wavelength light due to the small nucleated particle. The T-UV spectra inset on the upper RHS of SEM obtained was identical to the blue triangle profile spectra at 590s in Figure 4.3.1(D). Self-assembled Ag NP reduced by HCHO from Ag film without exposure to light exhibit a broad transmission valley with a minima at ~425 nm. Mie theory suggests the transmission Ag LSPR minima corresponds to a ~220-nm diameter Ag NP.[20] Figure 4.3.2(B) shows that continuous light exposure during HCHO treatment results in a distribution of smaller NPs, most of which are < 10 nm with scattered, larger 50-nm particles. Their corresponding transmittivity is blue-shifted, narrower, and higher. Mie theory predicts a transmission LSPR minima at ~400 nm corresponds to ~40 nm diameter Ag NP.[20] Inset in the lower LHS of Figure 4.4.2(B) is a schematic that indicates HCHO reduction of Ag film may covalently bind Ag to Sn(IV) or physically adsorb reduced Ag NP onto
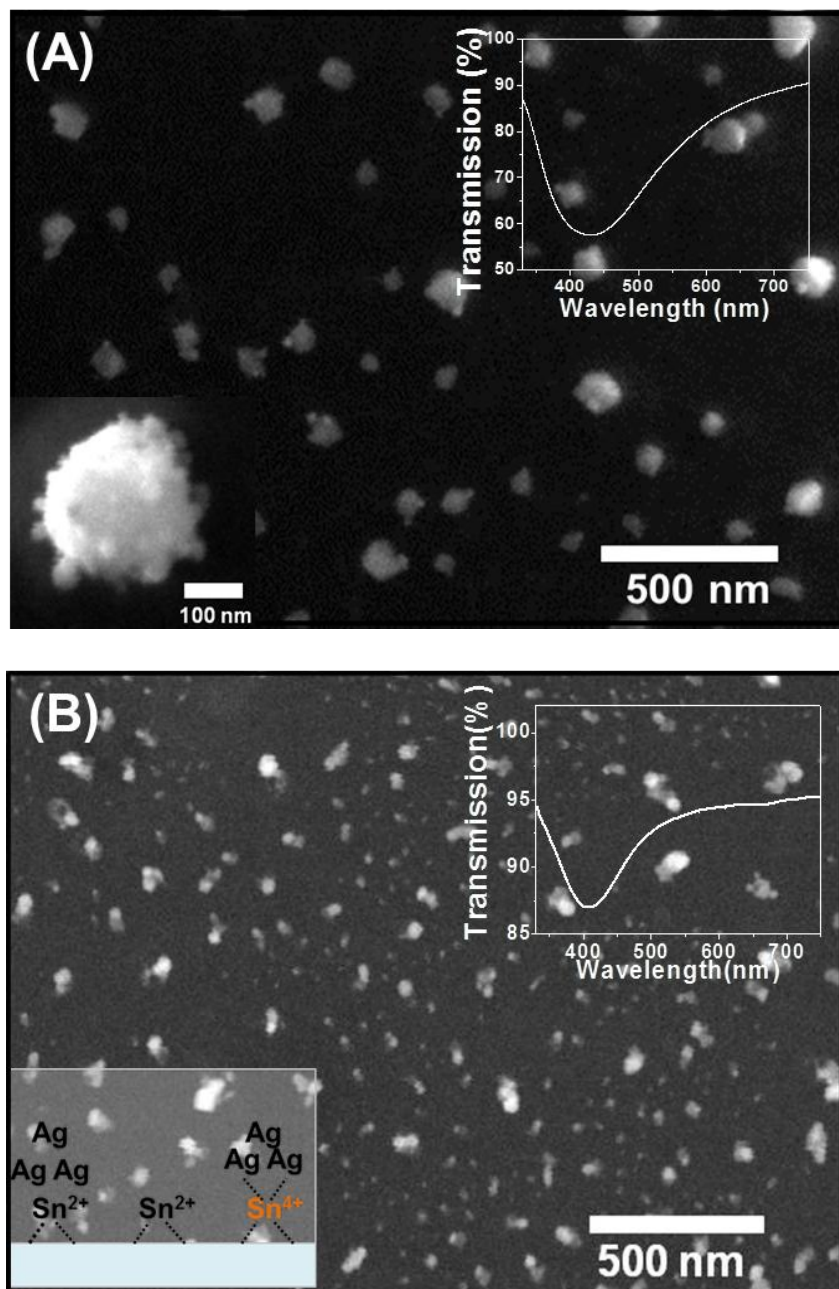
Figure 4.3.2 SEM images of wideband light exposure effect to HCHO treated Ag film on silicate substrate: (A) dark condition (B) continuous light exposure.

Sn(II). The schematic also indicates vacancies on the Sn-sensitized substrate due to HCHO-induced Ag film removal and washout of smaller Ag NP.

Previously, high temperatures were applied to thermally transform Ag island film to surface-associated NP. The data in Figures 4.3.1 and 4.3.2 indicate it is possible to transform Ag island film into nucleated Ag NP associated with a planar substrate using a strong reducing agent in the dark without energy intensive thermal treatment. Concomitant UV exposure appears to induce reduction of light sensitive Ag ions in solution, which interferes with aggregation into larger particles on the surface and apparent surface nucleation.

4.3.3.2   Dynamics and disposition of Ag and Au during EL Au thin film formation

Novel time dependent regimes are revealed in EL Au film growth. Dynamic, real-time T-UV spectroscopy revealed additional, previously-unrecognized time-dependent regimes during Au reduction, which occurs subsequent to Sn sensitization and Ag reduction. These successive regimes are transitory Ag NP formation, and transitional Ag and Au alloy formation, followed by self-catalyzed Au film growth. EL plating has the advantage of being able to uniformly coat a substrate without consideration of geometry (e.g. in recesses or holes), since the reducing potential is equal over the entire surface. However, it has also been reported that very thin films of EL coatings are not uniform because the initial deposition is confined to discrete nucleation sites that grow laterally and coalesce into a continuous film.[22] This motivates improved understanding of the nucleation regime to control nucleation rate and coverage in order to deposit uniform, ultra-thin film. While it has been reported that the nucleation of EL Au plating is initiated by galvanic displacement of Ag by Au, further characterization of transition steps between galvanic replacement of Ag by Au has not been performed.

Figure 4.3.3(A-B) show individual real-time T-UV spectra during an entire EL Au deposition, beginning with a baseline spectra for Sn sensitized substrate, and proceeding through a 2 min Ag activation and 5 min rinse, to a final 5 min Au deposition. Figure 4.3.3(B) expands the spectra obtained during an especially dynamic period between 0 sec and 70 sec for clarity. Notable in the spectra of Figure 4.3.3(A-B) are a transmission valley at ~425 nm corresponding to plasmon resonant Ag absorption and scattering, and a transmission peak at ~500 nm corresponding to Au PL. Figure 4.3.3(C) plots changes in the central wavelength (top panel) and amplitude (PH, bottom panel) for each feature as a function of deposition time. The Sn spectra captured after 10 min sensitization provides a transparent, reference silicate substrate with 100% transmission. Real time spectra were then *in situ* measured throughout Ag deposition at 30-sec intervals, consecutive D^3-H_2O washing and Au deposition at 1-sec intervals. The sample was designated CF-3-5 based on this hydraulic condition (3 mL/hr) and deposition time (5 min). The transmission spectra at 0 sec, selected after 2 min Ag activation and successive 5 min H_2O washing, exhibited transmissivity decreased to about 95% overall with a broad valley at ~495 nm. Consistent with the spectra of Ag island film in Figure 1.4(B)[Chapter 1] and 4.3.1(B), the transmission decrease due to reduction of Ag islands onto Sn^{2+} was completed in ≤30 s and the spectral features stabilized during subsequent 90 sec Ag injection and successive 5 min H_2O washing (data not shown). Overlapping spectra were omitted and specific time spectra were selected for clarity in Figure 4.3.3(A-B).

Transitory Ag NP formation. Upon introduction of the Au solution, a mixture of sodium Au(I) sulfite and HCHO, the transmission minima, as shown in Figure 4.3.3(B), rapidly blueshifted from 490 nm to 425 nm with increasing intensity between 0 s and 10 s as the mixture first contacted the Ag activated substrate. The transition of this optical feature was similar to
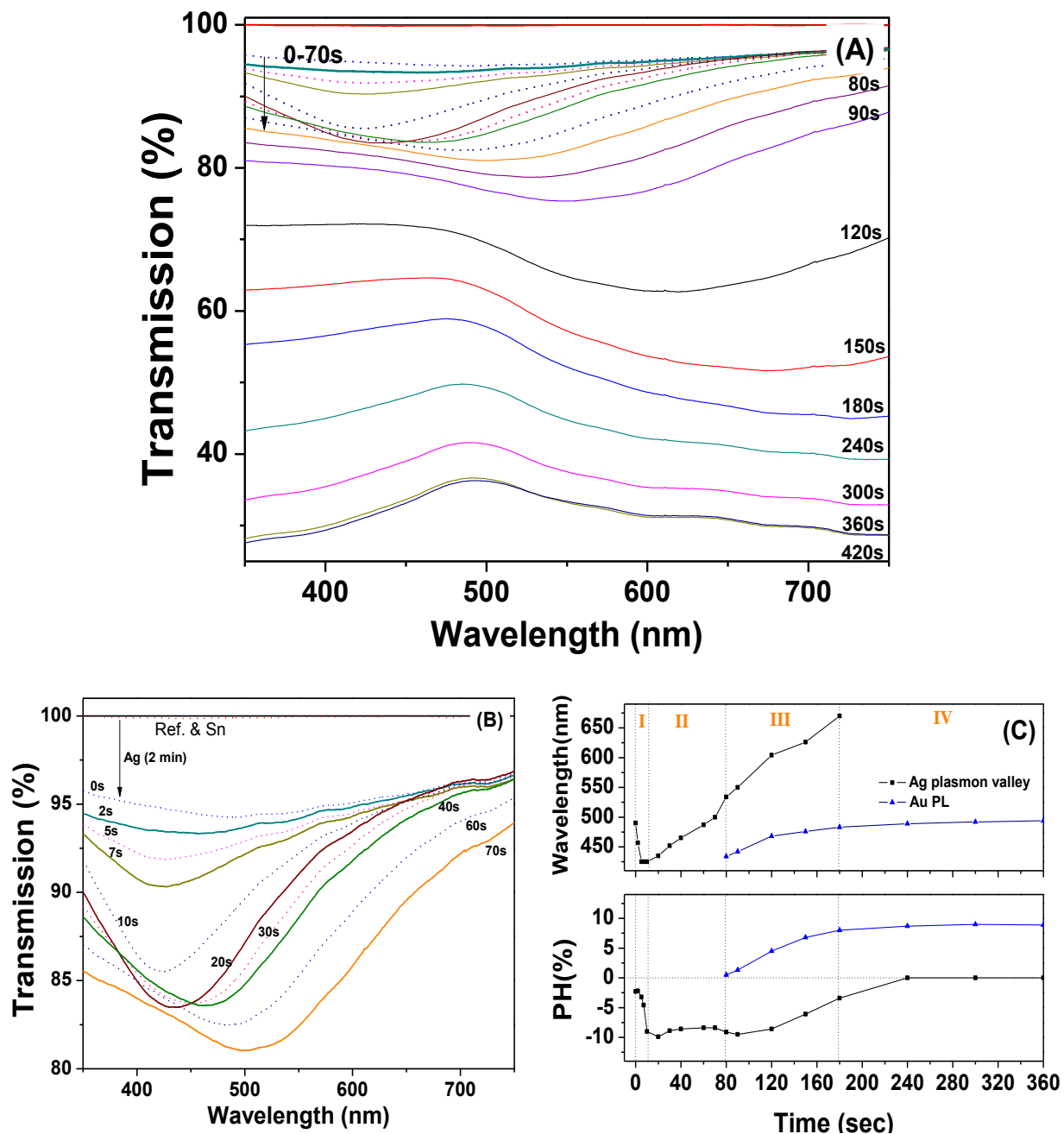
Figure 4.3.3 (A) Time resolved transmission spectra during a whole procedure of CF-EL Au deposition; Sn sensitization, Ag activation, galvanic replacement of Ag by Au, and Au film growth. The Ag spectral transmission was captured after 2 min CF deposition. The Au plating was performed at a flowrate of 3 ml/hr for 5 min. (B) Blow-up of spectra for 0-70 sec (C) Corresponding plasmon peaks (Ag Valley, Au PL) shift and peak height profile during EL Au deposition. Optical feature may represent physical transitions: Ag NP formation (I), Au/Ag alloy formation (II), Au film formation (III), and uniform Au film growth (IV)

isolated HCHO treatment of a Ag activated substrate as shown in Figure 4.3.2(B). It is attributed

to Ag NP aggregation resulting from 2-fold faster axial diffusion of HCHO ions in the advancing

front in addition to 2-fold faster lateral diffusion of HCHO ions through the stagnant boundary

layer adjacent to the surface, respectively, relative to Au(I) sulfite complex. Reductant may

contact reduced Ag film in advance of Au(I) ion due to the lower diffusivity of the latter ion

through a stagnant boundary layer of H_2O. The binary aqueous diffusion coefficient of methylene

glycol, a major hydration form of HCHO,[16] ($CH_2(OH)_2$; 1.6×10^{-5} cm^2/s) is ~2.7 times larger than

that for Au(I)-sulfite complex ion ($Au(SO_3)_3^{2-}$; 0.6×10^{-5} cm^2/s) as calculated from Wilke-Chang

and Nernst-Haskell equation[17] at 18 ºC, respectively. The diffusivity of Au(I) complex in

aqueous solution was measured 0.7×10^{-5} cm^2/s at kinematic viscosity of 0.011 cm^2/s for 0.05

mol/L.[18] From mass transfer principles[16] and hydraulic properties of diluted HCHO at 18 ºC, the

theoretical mass transfer rate of $CH_2(OH)_2$ (6.2×10^{-4} cm/s) is therefore ~2 times higher than

Au(I) complex (3.2×10^{-4} cm/s) in the CF-EL system. It has been reported that Au(I)-sulfite

complex dissociates to Au(I), which is reduced to Au(0) in the presence of exogenous electrons

supplied by galvanic displacement, electrical current, or strong reductant.[19] Using Mie theory, the

transmission minima, Ag LSPR absorption, at ~423 nm is attributable to a 40-nm diameter Ag

NP.[20]

Transitional Au and Ag alloy formation. At 20 sec, the transmission minima red-shifted as

the width of the underlying spectral feature increased. This corresponded to Au(I) ions

penetrating the stationary boundary layer, contacting the Ag activated surface, and initiating

galvanic displacement of Ag by Au. The bulk Au solution contacting the surface includes Au(I)

ions, displaced Ag ions, and/or metallic NPs, all of which may contribute to the observed

variation in transmission features during this transition period. Between 20 sec and 70 sec,

redshifting and peak broadening proceeded with decreasing overall transmissivity as galvanic formation of alloy NP and metallic island film layer progressed. Redshift and peak broadening are attributable to the formation of Ag/Au (core/shell) NP and/or Ag-Au alloy during the galvanic displacement of Ag by Au. Increasing the Au content of Ag/Au (core/shell) NPs and nano Ag-Au alloy in aqueous media is known to red-shift and increased damping of the plasmon spectra relative to pure Ag NPs.[23,24] Au-Ag alloy island film exhibits similar optical red-shifting and peak broadening with increasing Au content.[11,25] Decrease of overall transmissivity after 40 sec was attributable to additional Au deposition relative to the concurrently displaced Ag amount. This is consistent with the report by Ahn, et al.[7], that EL Au thin film formation is characterized by the formation of metallic nuclei and their subsequent annealing from discontinuous to continuous island structure. Au(I) ions diffusing through the boundary layer reduce metallic clusters as nuclei via galvanic displacement on available Ag NPs bound to Sn sensitizer. Ag NPs and Au NPs momentarily coexist until completion of galvanic displacement when deposited Au entirely covers the substrate.

Self-catalyzed Au film growth. Figure 4.3.3(A) shows that at 80 sec, the minima of transmission valley red-shifted to 530 nm in wavelength and a new transmission peak feature arose at ~430 nm. This feature is consistent with PL from Au thin films.[7,8] At 90 sec, the PL feature became distinguishable at a wavelength of 442 nm. Subsequently, it redshifted with sharpening PH as alloyed Ag was replaced by Au. In this kinetic period, galvanic displacement slows as the driving force of Au thin film growth switches to external electron donation from the reductant. HCHO reduces Au^+ to Au^0 on the galvanically formed Au nuclei which play the role of catalyst. As Au deposition time increased between 90 sec and 180 sec, the PH of Au PL dramatically increased and the peak position also red-shifted. This can be attributed to growth of

island film structure to a reported percolation threshold thickness[9] where coalescence creates a continuous path for electrons through the network with dramatically changing optical and electrical properties. In particular, the PL feature profile (blue triangles) in Figure 4.3.3(C) shows that after 180 sec, peak position and PH remained relatively constant while the overall transmission continued to decrease. This suggests that steady state Au deposition via CF increases the film thickness while sustaining the surface morphology.

These dynamic spectroscopic data during deposition, corroborated by opto/electronic microscopic and spectroscopic observations, suggest physical deposition of metal ions during EL Au film growth procedures, as shown in Figure 4.3.3(C), occurs during four dynamic regimes: (I) initial Ag NP formation via fast diffusing HCHO, (II) transitory Au/Ag alloy formation, (III) continuous Au film formation through percolation thickness, (IV) autocatalytic uniform Au film growth. This expanded understanding of transitional regimes in the initial EL Au film growth could improve control of continuity and surface uniformity of EL thin coating, and allow implementation of measures to control the size and coverage of nucleation clusters for coalescence of film formation.

4.3.3.3   Microscopic characterization of EL Au thin film

Intermediate deposition times produce continuously deposited films with packed uniform grains. Steady diffusion in equilibrium hydraulic conditions (i.e. CF) has been shown to produce EL Au films at short deposition times that exhibit more uniform surface morphology and optical features than EL films formed by unsteady-state diffusion in batch immersion (i.e. BI), or by vacuum vapor-deposited films. For deposition times in the range of 20 sec, 60 sec and 4 min, BI-EL plating yields discrete nucleated Au NPs, separated island, and discontinuous island films on quartz slides, respectively.[7] Without surface pretreatment and conductive substrate, vapor

deposition usually produces separate island thin film structure due to lattice mismatch. Equilibrium, steady diffusion via a constant concentration driving force in CF-EL plating improves continuity and uniformity of EL film for 2 min deposition relative to BI-EL film for 2 min.[8] The steady, higher mass transfer rate improved the surface morphology and uniformity, however the effect of extended plating time and different hydraulic conditions on film thickness and surface morphology have not been investigated for CF-EL thin films.

In this work, EL Au thin films were produced at longer deposition times of 5 min and 10 min, respectively, at both unsteady and steady hydrodynamic conditions. For 5 min BI deposition time, the EL Au film, as shown in SEM image of Table 3.2, exhibit uniformly close packed grain structures with less than 50 nm diameter. Increasing BI deposition time to 10 min (BI-10) and performing continuous, equilibrium deposition at similar hydraulic conditions of about 3 mL/hr (CF-3-5, CF-3-10) also exhibit very similar close packed grain structure. It appears that the HCHO driven autocatalytic Au reduction on nucleated Au NPs form uniform Au grains during intermediate deposition.

4.3.3.4   XPS interpretation of the EL Au thin film structure

Despite its relevance to a variety of optical and spectroscopic applications, the interface and internal physicochemical structure of EL deposited metal films does not appear to have been previously investigated. Extensive use has been made of X-ray photoelectron spectroscopy (XPS) in similar applications to quantify chemical composition and grain size of metal thin film structures at surfaces and to characterize solid inter-diffusion interactions at metal/oxide interfaces.[26,27] XPS has also been used to characterize chemical compositions of EL Au film surfaces, but without depth profiling.[28,29] In this work, XPS depth profiling indicates that the as-deposited EL Au film structure consists of a eutectic Au-Sn alloy and SnO_2 layer at the interface

between the metal film and silicate substrate upon which an internal Au film is deposited, with bulk Au grains and trace Ag debris at the upper metal-air surface.

Reduced Au ions appear to form bulk Au grains at interface and internal structure as deposited EL thin films. Application of XPS to characterize EL Au deposition suggests deposited EL Au exists as bulk grains (> 4 nm) at the interface accompanied by various internal structures. Electron microscopic images show that EL deposition at intermediate times forms Au bulk grains with ~50 nm diameter on the film surface. Figure 4.3.4(A) shows spectra of Au in CF-3-10 film at sputtering time intervals between 0 and 140 sec. The bulk Au in the Au 4f level exhibits two photoemission peaks, $4f_{7/2}$ (84.0 ± 0.2 eV) and $4f_{5/2}$ (87.65 ± 0.2 eV), with intensity ratio of 4:3 and energy difference, the spin-orbit splitting, of 3.65 eV.[30] When the uncorrected raw data from which Figure 4.3.4(A) was obtained were corrected for charging effects using the peak from carbon contamination at the surface, an Au photoemission peak at the surface for 0 min sputtering of 83.7 eV was obtained(See Table 4.3.1). This indicates as-deposited EL Au thin film forms a bulk elemental Au-Au bond at the surface. It also suggests that Au ions deposited by EL Au plating form bulk Au grains with larger than 4 nm diameter, since large metal clusters whose diameters exceed 4 nm have BE values that closely approximate the bulk metal value. When the size of deposited Au cluster decreases to less than 2 nm, the observed core-level Au $4f_{7/2}$ BE increases by a maximum of $0.8 - 1.2$ eV. This increase is attributed to effects of decreased core-hole screening by the conduction band, as a result of the discretization of the conduction band.[31,32,33] The SEM images of four different EL Au films, in Table 3.2, also confirm that the grain size of deposited Au NPs are larger than ~50 nm. This reaffirms the observed Au peak is the $4f_{7/2}$ Au-Au bulk peak (~84.0 eV) and validates spectral corrections for charging effects.
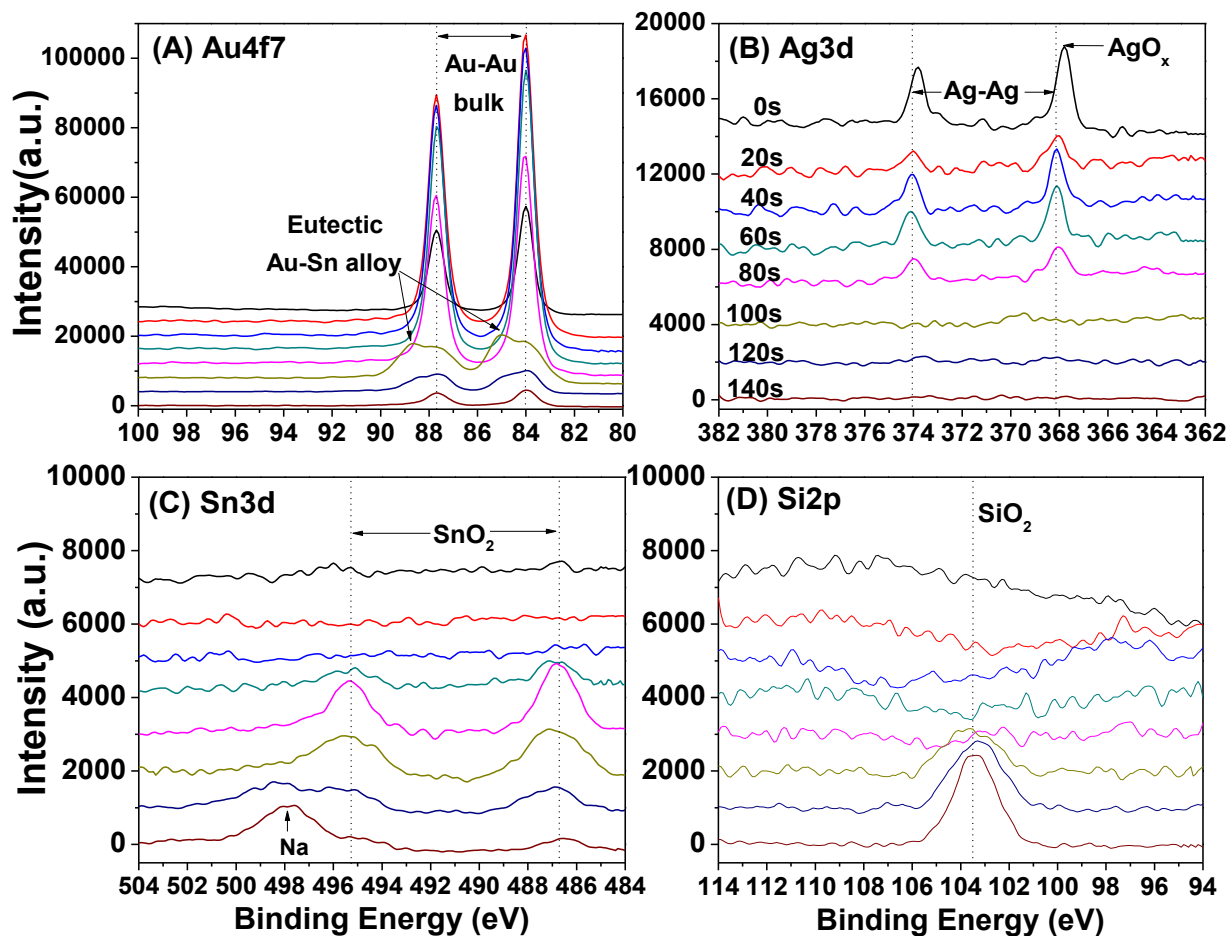
Figure 4.3.4 The XPS depth profiles of CF-3-10 for main chemical components: A) Au4f7; B) Ag3d; C) Sn3d; D) Si2p

Table 4.3.1. Peak position of XPS analysis for CF-3-10. The number in bracket is the corrected value after considering charging effect via Au reference.

Sput. Time (sec.)	C1s (C = 284.3~ 285.0)	O1s (SiO$_2$ = 532.5 -533.3)	Si2p (SiO$_2$ = 103.2~ 103.8)	Au 4f$_{7/2}$ (Au= 83.8 ~84.2)	AuSn4 (~85.0)	Ag3d$_{5/2}$ (Ag= 368.1~ 368.3)	Sn3d$_{5/2}$ (SnO$_2$ = 486.5~ 486.9)	Na Auger KLL (~498.0)	Shifting by Au ref (84.0)	Structure
0	284.0 (285.7)	531.1 (532.8)	-	82.3 (84.0)	-	366.1 (367.8)	-	-	+1.7	Surface
20	-	-	-	82.9 (84.0)	-	366.9 (368.0)	-	-	+1.1	Internal (Au)
40	-	-	-	83.0 (84.0)	-	367.1 (368.1)	-	-	+1.0	Internal (Au)
60	-	-	-	83.1 (84.0)	-	367.1 (368.0)	485.9 (486.8)	-	+0.9	Internal (Au)
80	-	531.9/530.7 (532.8/531.6)	-	83.1 (84.0)	-	367.1 (368.0)	485.9 (486.8)	-	+0.9	Internal (Au)
100	-	533.4/530.9 (533.0/530.5)	104.1 (103.7)	84.4 (84.0)	85.4 (85.0)	-	487.4 (487.0)	-	-0.4	Interface
120	-	532.4/529.9 (532.7/530.2)	103.1 (103.4)	83.7 (84.0)	84.7 (85.0)	-	486.5 (486.8)	498.1 (498.4)	+0.3	Interface
140		532.2/530.2 (532.6/530.6)	102.9 (103.3)	83.6 (84.0)			486.1 (486.5)	497.1 (497.5)	+0.4	Glass

The observed Au4f$_{7/2}$ peak positions below the surface (0 sec) were also corrected to the reference Au-Au bulk values (~84.0 eV). For CF-3-10 in Figure 4.3.4(A), the Au4f$_{7/2}$ peak intensity increased dramatically after the first sputtering, reaching a maximum between 20 and 60 sec, and decreasing at $\geq$ 80 sec. The intensity increase was attributable to removal of contamination layers associated with disappearance of the carbon peak during the first 20-sec interval of Ar$^+$ sputtering. Values of FWHM for 20, 40, 60 and 80 sec were 0.76, 0.76, 0.77 and 0.77, respectively. Consistency of the peak intensity and FWHM values indicates the uniformity of reduced metallic Au grains that form the internal structure of CF-EL Au film. The Ar$^+$ sputtering rate for Au depth profiling was 0.3 ~ 0.7 nm/sec. While bombardment with Ar$^+$ ions can promote Au diffusion and aggregation and transform Au-Au cluster to Au-Au bulk due to transfer of kinetic energy of the ion to the surface atom, the consistency of the spectral features suggest the bulk elemental Au-Au bond is inherent to the film itself.

The above microscopic characterization indicates that the EL deposited Au form bulk grain with ~50 nm of diameter at the surface. However, the interface and internal Au structure in as-deposited films are not investigated. XPS has been used extensively to investigate chemical composition and grain size of metal thin film structures at surfaces and solid inter-diffusion interaction at metal/oxide interface. The XPS interpretation suggest the deposited Au exist as bulk grains (> 4 nm) at the interface and internal structure.

Sensitized Sn forms Au-Sn alloy and SnO$_2$ at the interface between silicate and Au. Sensitization by Sn via dehydration of surface hydroxyl groups provides catalytic sites which are a path for the initiation of EL plating of other metals. Stannous ion (Sn(II)) is usually used as a sensitizer for Au film growth. SnCl$_2$ sensitization also provides better uniform coverage on hydrophobic surfaces than SnCl$_4$. In addition to redox mechanisms for stannous ion illustrated in

Eqs. (4-7) time-resolved XPS profiles suggest that sensitized Sn reacting with Au and silicate results in heterogeneous AuSn alloy and SnO_2 at the interface.

In Figure 4.3.4(A) a new peak appeared at ~85.0 eV on the shoulder of $Au4f_{7/2}$ photoemission peak after 100 sec sputtering (depth 50 ±17nm). It is attributed to the existence of eutectic Au-Sn alloy at the interface between Au film and silicate glass substrate. The BE of Au_5Sn at ζ'(composition based on Au_5Sn) phase was reported at 84.14 eV.[34] AuSn at ζ' and δ (composition AuSn) phases were 84.30 eV and 84.9 eV, respectively.[27] The alloy of Au_4Sn shows a shoulder peak at ~85.0 eV.[30] This suggests that during EL Au plating, deposition of reduced metallic Au completely replaces Ag clusters and anchors onto Sn layer in the form of Au-Sn alloy. For the as deposited Au-Sn thin film system, the phase formation via interfacial reaction between Au and Sn is easily performed at room temperature.[27,34,35] Due to faster diffusivity of Au atoms compared to Sn atoms, Au atoms rapidly diffuse into the Sn layer through the Sn grain boundaries, resulting in Au_5Sn, Au_2Sn AuSn, $AuSn_2$ and $AuSn_4$.[27] The Sn3d depth profile in Figure 4.3.4(C) after 80 s sputtering confirms the existence of Sn at the interface between the Au film and the silicate substrate.

After EL Au deposition, the sensitized Sn presents as eutectic Au-Sn alloy and putative oxidized tin (SnO_2) at the interface. Fig. 4.3.4(C) shows no observable Sn3d peaks in the uppermost layer of Au thin film during 0~40 sec of sputtering. After 60 sec, two noticeable peaks appeared 495 eV and 487 eV and the intensity intensely increased at 80 sec. The peak intensities decrease after 120 sec. The observed $Sn3d_{5/2}$ peak at 486.8 eV is attributed to either oxidation states of the bound Sn or oxidized Au-Sn alloy.[34] The observed $Sn3d_{5/2}$ peaks during 80-140 sec are well matched with the reported Sn peak at ~486.5 eV after Sn sensitization. Previous literature reports distinguished SnO and SnO_2 via the O1s core level XPS spectra

assigning 529.9 and 529.7 eV for SnO and 530.3 and 530.5 eV for SnO_2. The BE of $Sn3d_{5/2}$ from oxidized Au-Sn alloys is basically similar to the oxidation of metallic Sn because a thin Sn oxides skin preferentially forms in oxidation of Au-Sn alloys.[34] Whole CF-EL deposition was performed in open environmental condition. Specifically, Sn sensitization was performed by dropwise deposition to reduce possible Au deposition inside of flow tubes of CF-EL plating system and then the Sn sensitized substrate was installed in CF-EL plating system. During this brief time, surface oxidation of the bound Sn and unbounded residual Sn on the glass substrate is likely to occur due to exposure to air and water containing dissolved oxygen. Thus, two forms of Sn, oxidized Au-Sn alloys and SnO_2 may be present in heterogeneous mixing condition at the interface layer which was reached after 80 sec Ar sputtering. The adjacent peak appearing at ~498.0 eV was assigned to Na which may be a component of soda lime silica substrate.

Various Ag forms exist in surface and internal thin film. The Ag $3d_{5/2}$ spectrum at the surface, 0 min sputtering, in Figure 4.3.4(B) show a peak at ~367.80 eV -- a value lower than BE of bulk elemental Ag (368.2 eV) that could assigned to AgO_x (367.3-368.0 eV),[30] which may be due to exposure to air. However, the internal Ag after 20~80 sec are 368.0, 368.1, 368.0 and 368.0 eV which are close to bulk elemental Ag. The previous study reported that in Ag activation, deposited Ag is bound to the surface as metallic silver, not through an oxygen atom to Sn. The real-time transmission spectra show galvanically replaced Ag NPs temporarily form Au-Ag alloy state. Therefore, the appearance of metallic Ag during 0–80 sec of depth profiling could be attributed to continuous bulk displacement of Ag NPs from upstream by the hydraulic conditions and subsequent deposition to form a mixture of Ag and Au during film growth. Interestingly, no observable Ag peaks were found at 100 sec and 120 sec when the sputtering reached to the

interface between Au and silicate glass. It suggests that the galvanic displacement completely removes Ag at the interface and then forms a Au and Sn interface.

Si indicates the thickness of as deposited EL Au film. The Si2p XPS spectrum, shown in Figure 4.4.5(D), suggests information about EL deposited Au film thickness by indicating the boundary between Au and SiO_2 glass substrate. After 100 sec of sputtering, a peak at 103.7 eV, corresponding to Si2p in SiO_2 (~103.5 eV) appeared. Based on this observation and a sputtering rate of Au (0.3 ~ 0.7 nm/sec), the Ar sputtering reached the interface after 80 sec and the corresponding thickness is between about 30 and 70 nm. This observation corresponds to other depth profiling, which shows a sudden decrease in Au peak intensity and Ag peak disappearance at 80 sec.

Quantitative XPS analysis allows identifying CF effect and deposition time. Figure 4.3.5 compares the quantitative atomic percent composition of CF-EL and BI-EL film during intermittent 20 sec depth profiling for a total of 150 sec. For CF-3-5, as shown in Figure 4.3.5(C), at the surface (0 min sputtering), the Au content is ~15.2 %, 50.2% of C due to organic carbonate and 24.8% of O, 1.6% of Ag. After 20 seconds sputtering, the Au concentration dramatically increased to 83.7 %, whereas C and O contents decrease to 9.9 and 4.1%, respectively. The further 40 second sputtering exhibited improved Au content to 89.7 % with further decrease to 5.5% of C and 3.5 % of O, which represents the chemical composition of internal structure of EL Au film. After 60 seconds, the Au content decreased to 81.5% due to increase in oxygen content to 7.9% which may originate from metal oxides such as Au, Ag (0.8%) and Sn (3.4%). The Sn content was suddenly increased from 0.3 % at 40 second of sputtering. No Si was detected at this sputtering step. At 80 second, the Au content decrease to 44.7 %, while O, Si and Sn increase 34.0%, 10.4% and 4.6%, respectively. After 100 seconds, the content of O(59.5%) and Si(20.4%)
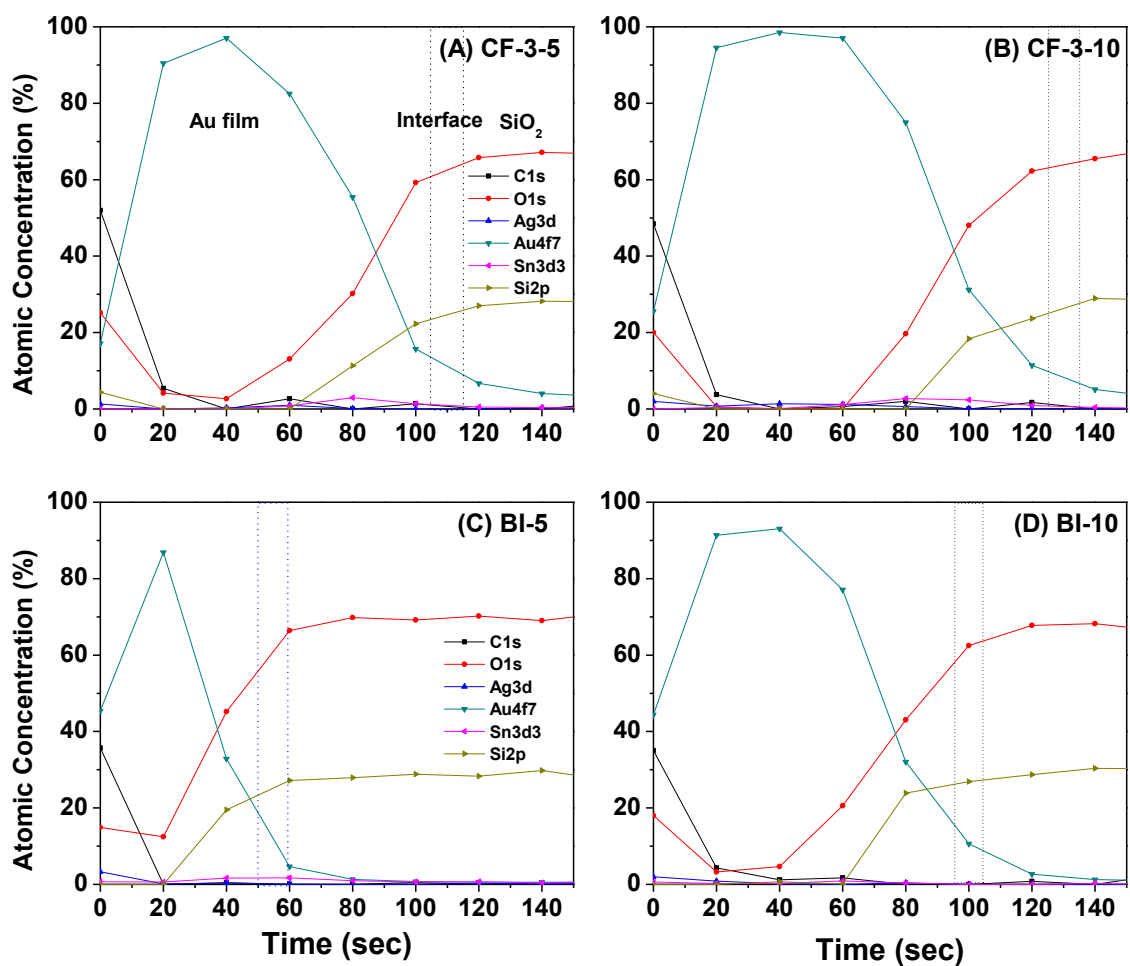
Figure 4.3.5 Quantitative chemical component characterization of XPS depth profile of two different CF and BI deposited film for 5 and 10 min. Target chemical components are C1s, O1s, Ag3d, Au4f7, Sn3d3 and Si2P.

exceeded the Au content (14.6%). Interestingly, the Sn content decreased to 2.5 %. Based on this observation, the interface of the CF-3-5 film may be revealed after 80 ~ 100 second of Ar sputtering. The interface area is indicated by dot box in Figure 4.3.5(C). After 120 seconds, the O, Si, and Na content are stabilized at 64.4 ± 0.9%, ~27.3 ± 0.2%, and 2.3± 0.3% until 240 seconds. These three main components are contributed to soda lime silica glass substrate.

Other EL film's atomic concentration profile also exhibit similar pattern for distinguishable structural features such as surface, internal structure of Au film, interface and SiO_2 substrate. However, the interface locations or film thickness are dependent on different Au mass transferred amount induced by varying deposition time and hydrodynamic conditions. Considering main components distribution, Au, O and Si, the location of interface composition was assigned to below 10% of Au and more than 30% and 15% of O and Si. Based on this standard the interface of BI-5, BI-10, CF-3-5 and CF-3-10 are assigned to ~55, ~100, ~110 and ~130 sec. The hydrodynamic comparison clearly shows that the thickness of CF-EL films is higher than BI-EL films at the same deposition time. The increased mass transfer rate and steady higher average local concentration during CF increase the deposited amount relative to batch immersion, resulting in thicker films.

4.3.3.5   Mechanism of EL Au thin film growth

Novel EL Au film growth mechanism. Figure 4.3.6 describes a new physicochemical EL Au film growth mechanism based on time-resolved T-UV spectra and XPS characterization. Specifically, new physical transformation procedures at equilibrium hydrodynamic condition, diffusion and corresponding driving force are included in the new scheme. The growth mechanism could be categorized as followed: Sn sensitization [3], self-limited Ag activation[6], instant Ag NP formation[9], galvanic displacement of Ag by Au[10], transitory Au/Ag alloy

formation during displacement [11], autocatalytic Au thin film deposition[12]. In step [12], the gray dots between Au NPs and internal Au film indicate displaced Ag clusters whose existence confirmed by XPS profiling.

4.3.4 Conclusion

Time resolved spectroscopic plasmon resonance measurements extend the description of Ag disposition during EL deposition to include formation of EL Ag nanostructures including island film, NPs, and nucleated NPs based on exposure to broadband light and exogenous reductant. These kinetic data show that such Ag nano-architecture may be self-assembled onto planar ceramic substrates without energy intensive control processes that have been used previously. Kinetic monitoring of plasmon profiles during EL Ag and Au deposition reveals previously unrecognized transitory physicochemical Ag states that include self-limited Ag activation, temporary Ag NP aggregation by HCHO, transitional Ag-Au alloy formation during galvanic displacement, and autocatalytic uniform Au film growth after Ag replacement. XPS depth profiling provides corresponding surface, internal and interface physicochemical structural characterization of Ag disposition after EL Au deposition that supports optical characterization of EL Au film growth mechanisms. These new methods enhance understanding of dynamics and disposition of metal ions during EL plating and improve control over particle nucleation and coalescence as well as morphology and continuity of ultra-thin films at the atomic scale.
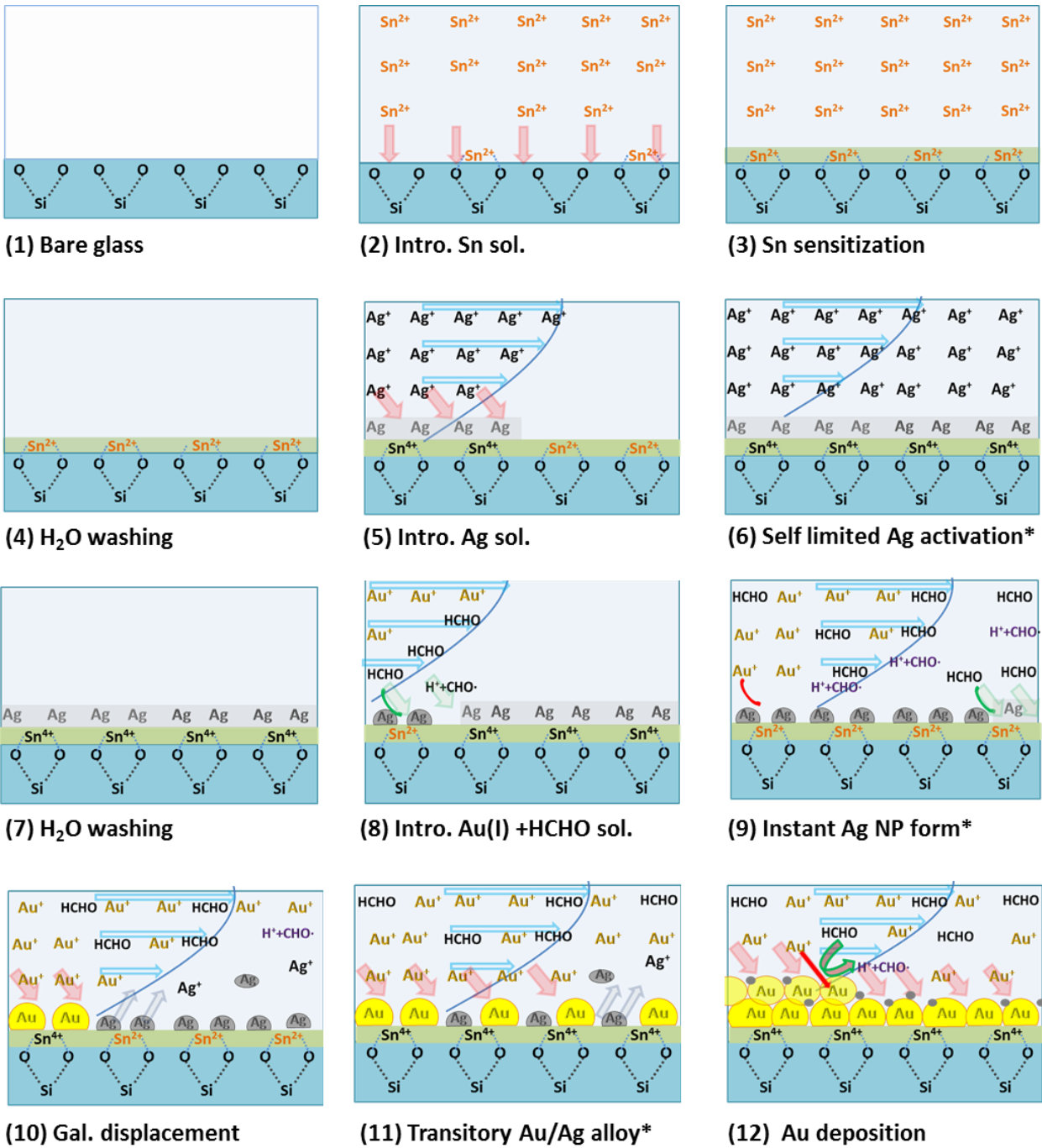
Figure 4.3.6 The physicochemical procedure of CF-EL Au deposition on silicate substrate: Sn sensitization, Ag activation on Sn, galvanic displacement of Ag by Au, Au film growth. Star marks(*) indicate revealed transitional physicochemical reactions from this work.

4.3.5 References

(1) Yasutake, Y.; Kono, K.; Kanehara, M.; Teranishi, T.; Buitelaar, M. *Appl. Phys. Lett*. **2007**, *91*, 203107.

(2) Hu, X.; He, Q; Lu, H.; Chen, H. *J. Elec. Chem.* **2010**, *638*, 21-27.

(3) Wu, J.; Bai, H-J.; Zhang, X-B.; Xu, J-J.; Chen. H-Y. *Langmuir* **2010**, *26(2),* 1191-1198.

(4) Ko, J.; Koo, H.; Kim, D.; Seo, S.; Kang, T.; Kwon, Y.; Yoon, J.; Cheon, J.; Kim, Y.; Kim, J.; Park, Y. *J. Electrochem. Soc*. **2010**, *157(1),* D46-D49.

(5) Martin, P. M. In *Handbook of Deposition Technologies for Films and Coating-Science, Applications and Technologies*, 3nd ed.; Elsevier : 2010; Chapter 12

(6) Okinaka, Y., In *Electroless Plating of Gold and Gold Alloys. In Electroless Plating: Fundamentals and Applications*,; Mallory, G. O.; Hajdu, J. B. Eds.; American Electroplaters and Surface Finishers Society: Orlando, FL, 1990; pp 401-420

(7) Ahn, W.; Taylor, B.; Dall'Asén, A. G.; Roper, D. K. *Langmuir*, **2008**, *24*, 4174-4184.

(8) Jang, G.G.; Roper, D. K. *J. Phys. Chem. C* **2009**, *113*, 19228-19236.

(9) Kaiser, N. *Appl. Opt.* **2002**, *41(16),* 3053-3060.

(10) Singer, R. R.; Leitner, A.; Aussenegg, F. R. *J. Opt. Soc. Am. B*, **1995**, *12*, 220-228.

(11) Baba, K.; Okuno, T.; Miyagi, M. *Appl. Phys. Lett.* **1993**, *62(5),* 437-439.

(12) Park. H.; Zhang, X.; Choi, Y.; Kim, H.; Park, H.; Hill, R.H. *J. Cera. Soc. Japan*, **2010**, *118(11),* 1002-1005.

(13) Jang, G.G.; Roper, D. K. *Anal. Chem.* **2011**, *83*, 1836-1842.

(14) Koura, N. Electroless Plating of Silver. In *Electroless Plating: Fundamentals and Applications,* Mallory, G. O.; Hajdu, J. B. Eds.; American Electroplaters and Surface Finishers Society: Orlando, FL, 1990; pp 441-462

(15) Yang, J.; Chen, S. *Appl. Spectrosc.* **2001**, *55(4),* 399-406.

(16) Kortenaar, M. V.; Kolar, Z. I.; Goeij, J. J. M.; Frens, G. *J. Electrochem. Soc.* **2001**, *148(8),* E327-E335.

(17) Seader, J. D.; Henley, E. J. In *Separation Process Principles*. 2nd ed.; John Wiley and Sons, Inc.: New York 2006.

(18) Roy, S.; Caprodossi, S. In *Electrochemical Technology Application in Electronics III.* 1999, Proceedings of the Symposium on Electrodeposition, PV 99-34, Honolulu, Hawaii, Fall 1999;

Osaka, T.; Madore, C.; Romankiw, L.T.; Yamazaki, Y. Eds. The Electrochemical Society, Pennington, NJ, USA, 2000; pp145-151.

(19) Osaka, T.; Kodera, A.; Misato, T.; Homma, T.; Okinaka, Y.; Yoshioka, O. J. Electrochem, Soc. 1997, 144(10), 3462-3469.

(20) Craig, F.B.; Donald, R.H. Absorption and Scattering of Light by Small Particles; Wiley-VCH: New York, 1998.

(21) Chen, X.; Jia, B.; Saha, J. K.; Cai, B.; Stokes, N.; Qiao, Q.; Wang, Y.; Shi, Z.; Gu, M. *Nano Lett*. **2012**

(22) Electroless Deposition. *Kirk-Othmer Encyclopedia of Chemical Technology* [Online]; Wiley & Sons, Published online July 20, 2004. http://onlinelibrary.wiley.com/doi/10.1002/0471238961. 0512050311182112. a01.pub2/full (access Apr 19, 2012)

(23) Wilcoxon, J. *J. Phys. Chem. B* **2009**, *113*, 2647-2656.

(24) Link, S.; Wang, Z. L.; El-Sayed, M. A. *J. Phys, Chem. B* **1999**, *103*, 3529-3533.

(25) Sancho-Parramon, J.; Janicki, V.; Loncaric, M.; Zorc, H.; Bubcek, P.; Bernstorff, S. *Appl. Phys. A* **2011**, *103*, 745-748.

(26) Figueired, N.M.; Carvalho, N.J.M.; Cavaleiro, A. *Appl. Surf. Sci.* **2011**, *257*, 5793-5798.

(27) Tang, W.; He, A.; Liu, Q.; Ivey, D.G. *Acta Materialia* **2008**, *56*, 5818-5827.

(28) Huang, H.; Zhang, S.; Qi, L.; Yu, X.; Chen, Y. *Surf. Coat. Technol.* **2006**, *200*, 4389-4396.

(29) Hu, J.; Li, W.; Chen, J.; Zhang, X.; Zhao, Z. *Surf. Coat. Technol.* **2008**, *202*, 2922-2926.

(30) Wagner, C.D.; Riggs, W.M.; Davis, L.E.; Moulder, J.F.; Muilenberg, G.E. *Handbook of X-ray photoelectron Spectroscopy*, Perkin-Elmer Corporation, Minnesota, 1978

(31) Rao, C.N.R.; Vijayakrishnan, V.; Aiyer, H. N.; Kulkarni, G. N.; Subbanna, G. N. *J. Phys, Chem.* **1993**, *97*, 11157-11169.

(32) Mason, M.G. *Phys, Rev. B* **1983**, *27*, 748-762.

(33) Magkoev, T.T.; Christmann, K.; Moutinho, A.M.C.; Murata, Y. *Surf. Sci.* **2002,** *515*, 538-552.

(34) Taylor, J. A.; Merchant, S.M.; Perry, D.L. *J. Appl. Phys.* **1995**, *78(9),* 5356-5361.

(35) Buene L.; Falkenberg-Arell, H.; Tafto, *J., Thin Solid Films*, 1980, *67*, 95-102.

4.4 Prediction of EL Au deposition on silicate surface at unsteady and steady condition

4.4.1. Significance of this work

A kinetic study of EL noble metal deposition on silica surfaces at unsteady and steady conditions measured using real-time T-UV spectroscopy, SEM and XPS shows consistency with metal ion Fickian diffusion predicted in batch immersion and CF flow channel systems. The time-resolved kinetic transmission profiles enable to characterize time frame of heterogeneous physicochemical regimes during EL Au film deposition and validate possible CF (steady) and batch immersion (unsteady) mass transfer models. The developed correlations between models and kinetic optical features, decreasing slope and transmission drop of profile, predict precise deposition rates and specific deposition amounts in scalable flow cell substrates. Good correspondence between film thickness measured by XPS depth profiling and SEM cross-section analysis with computed values for 5 min and 10 min deposition in scalable flow cells suggest the rate limiting step of EL Au film thickness growth is limited by flow-enhanced diffusion for deposited thicknesses ≤ 100 nm.

4.4.2. Characterization Results and Discussion

4.4.2.1. Mass transfer limited EL Au deposition

Mass transfer description predicts thin film thicknesses ≤ 100 nm. The total deposited amount of Au ions was predicted using mass transfer coefficients, a diffusivity of Au(I) sulfite complex of 0.6×10^{-5} cm^2/s, eqn (2.2)-(2.8) and mass flux correlation eqn (2.11). This quantity was converted to thickness values using Au's density and the area of deposition. The predicted values were compared to actual thicknesses measured by cross sectional SEM image analysis and XPS depth profiling.
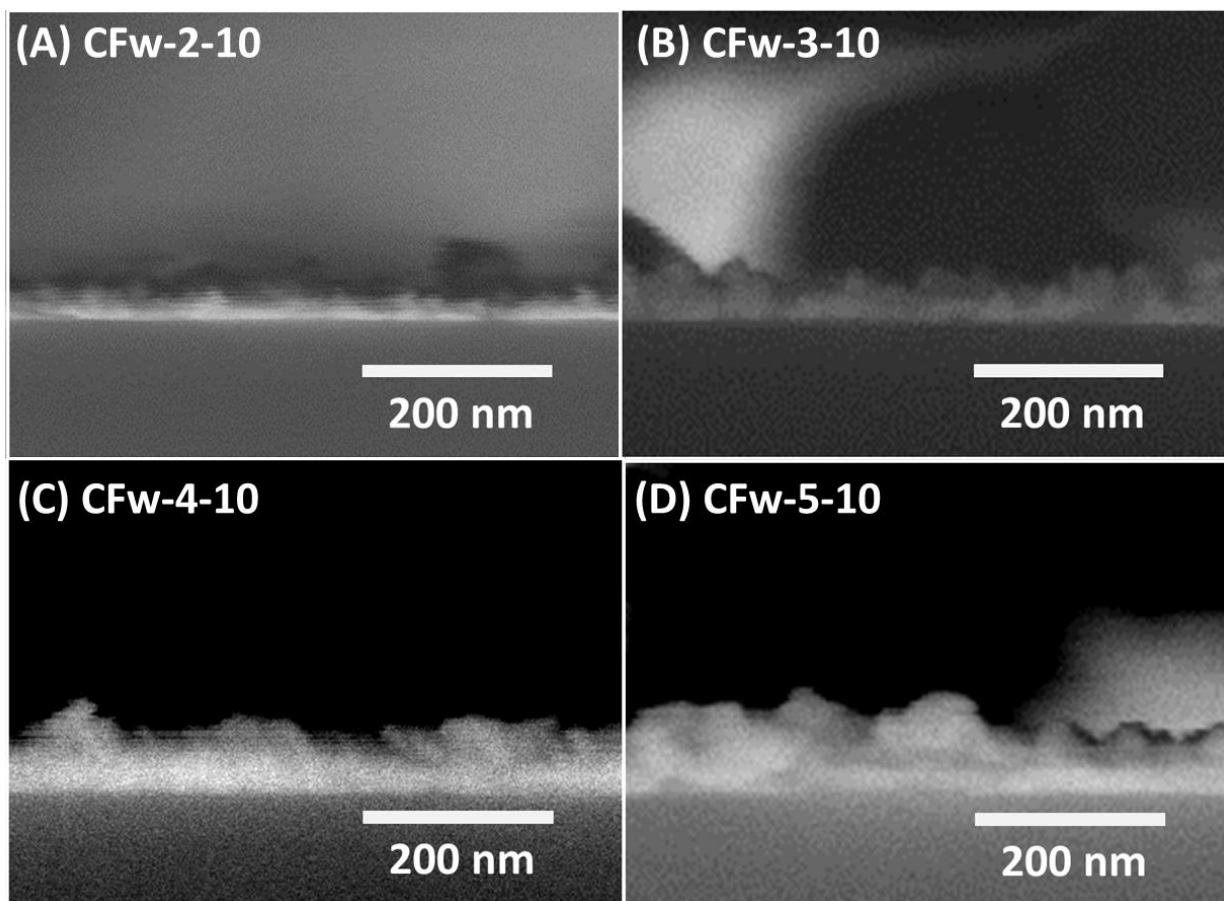
Figure 4.4.1. Cross-sectional SEM image of wide flow channel CF-EL films (CF$_w$) deposited with increasing flowrates from 2 mL/hr to 5 mL/hr for 10 min. (A) CF$_w$-2-10, (B) CF$_w$-3-10, (C) CF$_w$-4-10, (D) CF$_w$-5-10.

CF-EL Au films were deposited with increasing flowrates between 2 and 5 mL/hr for 10 min in a 0.3-cm-wide flow channel (designated to CF_w-(flow rate)-10, wide channel). Figure 4.4.1 shows SEM images of the cross sections of deposited CF_w-EL Au films: (A) CF_w-2-10, (B) CF_w-3-10, (C) CF_w-4-10, (D) CF_w-5-10. The backscattered electron detector represents the Au thin film as brighter than the silicate substrate due to higher atomic number. The deposited EL Au film thickness increased with increased flowrate. The average thicknesses of four samples, CF_w-2-10, CF_w-3-10, CF_w-4-10 and CF_w-5-10, were measured as 46.0±8.6, 58.0±14.7, 69.2±10.5 and 88.9±23.1 nm, respectively. The average thickness (n=50) was obtained from individual thickness measurements at ~30 nm-intervals along a 2 μm length of film in each SEM image.

Figure 4.4.2(A) shows the final theoretical thickness profile calculated using the empirical film model (eqn (2.8)-(2.11)) as a function of Reynolds number after a 10 min deposition time. These profiles were evaluated for narrow (w × h × l = 0.2×0.08×2.8 cm^3; CF) and wide (w × h × l = 0.3×0.08×2.8 cm^3; CF_w) flow channel geometries to represent the flow cell dimensions used. The dimensionless Reynolds number ($N_{Re}=Qd_H/(\nu A_c)$), can be used to determine dynamic similitude between different experimental cases. Based on each actual CF_w flow channel dimension (black square), Reynolds numbers are 0.31, 0.50, 0.60 and 0.90 with increasing flow rate 2 to 3 to 4 to 5 ml/hr. Reynolds number for CF-3-10 (red circle) is 0.66, because of the narrower channel width (~0.2 cm). Details of the cell dimensions and hydraulic conditions for calculation of Reynolds numbers are available in Table 4.4.1. As Reynolds number increases, the predicted thickness profiles increase. Significantly, it is shown that measured thicknesses for CF samples match well with the profiles of predicted thickness values.

Figure 4.4.2(B) exhibits the predicted thickness profile for BI-EL deposition, semi-
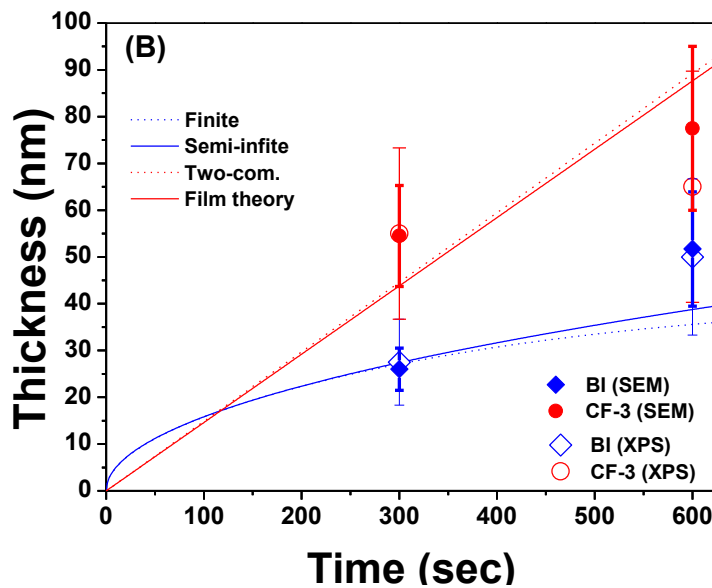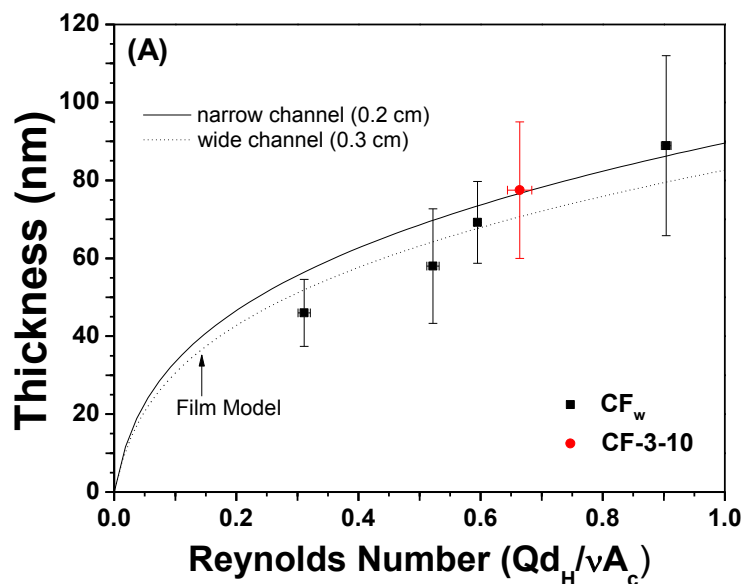
Figure 4.4.2. Measured (data points) and predicted (lines and dots; film theory) thickness profile of EL Au deposition. (A) CF-EL deposited films with varying Reynolds numbers. (B) Comparison between BI and CF EL deposited films with varying time. The prediction was calculated based on a flowrate of 3 mL/hr and the flow cell dimension (0.08 x 0.2 x 3.2 cm^3)

Table 4.4.1. A summary of cell dimensions, deposition conditions, Reynolds numbers and optical observation from each CF-EL deposition.

	CFw-2-10	CFw-3-10	CFw-4-10	CFw-5-10	CF-3-10
Cell dimension (W×H×L, mm^3) (measured width)	2.7×0.8×31.2 (2.76/2.65/2.82/2.82)	2.3×0.8×31.8 (2.35/2.35/2.41/2.35)	2.8×0.8×31.5 (2.88/2.94/2.94/2.88)	2.3×0.8×31.2 (2.23/2.23/2.29/2.29)	1.8×0.8×32.0 (1.64/1.71/1.70/1.76)
Flowrate (Q, ml/hr)	2	3	4	5	3
Re (Qd$_H$/νA$_c$)	~0.311 (0.306~0.321)	~0.500 (0.495~0.505)	~0.595 (0.592~0.601)	~0.904 (0.895~0.913)	~0.664 (0.64~0.68)
Slope(%/s) of transmission profile at 495nm (10~610s)	-0.084 (R^2=0.995)	-0.090 (R^2=0.996)	-0.094 (R^2=0.974)	-0.121 (R^2=0.963)	-0.112 (R^2=0.922) (26~626s)*
Slope(%/s) of transmission profile at 495nm (50~300s)	-0.089 (R^2=0.993)	-0.099 (R^2=0.993)	-0.127 (R^2=0.993)	-0.160 (R^2=0.993)	-0.143 (R^2=0.995) (70~300s)*
Drop(%) of transmission at 495nm (10~610s)	45.9	53.0	59.3	69.7	64.9 (26~626s)*
Slope(%/s) of transmission profile at 425nm (10~610s)	-0.098 (R^2=0.992)	-0.107 (R^2=0.996)	-0.120 (R^2=0.966)	-0.147 (R^2=0.956)	-0.120(R^2=0.925)
Drop(%) of transmission at 425nm (10~610s)	51.0	56.8	64.2	76.2	60.5 (26~626)*

Teflon tape is compressible with the range of h= 0.70~0.85 mm, Kinematic viscosity(ν) of diluted Au solution is assumed to be 0.01004 cm^2/s

* For CF-3-10, the estimated time regime of Au related deposition is between 25 and 625 sec.

infinite (eqn (2.2)) and finite unsteady state diffusion model (eqn. (2.4)) and CF-EL deposition, two-compartment (eqn (2.5)) and film theory (eqn (2.8)), as a function of deposition time. These EL Au films were deposited on narrow channels. The predicted profiles of the CF-EL models, exhibit a linear thickness increase as a function of deposition time, while the growth of BI-EL models shows a less rapid, non-linear increase. The CF-EL profile of two compartment and effective rate model (red solid line) corresponds to empirical film model (red dot line). For our system, both the finite (blue dot line) and semi-infinite (blue solid line) models show consistency. For CF-EL deposited films, the thickness of CF-3-5, and CF-3-10 measured by SEM analysis (red solid circles) and XPS depth profiling (red empty circles), indicated in next square brackets, are 54.5±10.8 nm [55.0±18.3 nm] and 77.5±17.5 nm [65.0±24.7 nm]. For BI-EL deposition, SEM and XPS thickness, indicated in square brackets, of BI-5 and BI-10 (blue solid and empty diamonds) are 26.5±4.5 nm [27.5±9.2 nm] and 51.7±12.2 nm [50.0±16.7 nm], respectively. The thickness measured by XPS depth profiling corresponds with SEM image analysis. Predicted deposition rates based on flow-enhanced Fickian diffusion in Figure 4.4.2(B) are consistent with measured deposition rates. This agreement suggests that EL Au thin film growth under these hydraulic conditions is mass transfer limited and that the description developed for continuum, microscopic systems may be extended to nano-scale EL thin films with a thicknesses less than 100 nm.

4.4.2.2. Quantitative kinetic characterization in EL Au plating reaction

Kinetic profiles distinguish sequential physicochemical reactions of EL Au deposition. Au ion deposition has been correlated to optical plasmon transmission variations (opacity, peak position and peak height).[11] Real-time measurement of dynamic transmission features at specific wavelengths provides information about the rate of accumulation of various forms of metal on

transparent surfaces. From this information, the rates of metal ion diffusion and its successive reduction to metallic Au film could be inferred in the absence of confounding transmission features. In general, transmission at a particular wavelength during EL Au deposition cannot be attributed solely to Au deposition or Au(I) diffusion because of potentially overlapping optical effects due to prior EL mechanisms such as HCHO driven Ag NP formation or formation of Ag-Au alloy during galvanic displacement of Ag by Au, or subsequent mechanisms such as autocatalytic uniform Au film formation.[27] Accurate inference of metal ion diffusion rates requires distinguishing particular time frames during EL Au deposition in which Ag NP formation and Ag-Au alloy formation occur in order to isolate dynamic transmission features relevant to Au deposition and diffusion rate.

Figure 4.4.3 shows kinetic profiles which consist of discrete measures of transmission at 425 nm (dotted lines) and 495 nm (solid lines) corresponding to the known Ag LSPR and Au PL feature, taken in real time during EL Au deposition. Blue and red lines correspond to plating by batch immersion for 10 minutes (BI-10) and by continuous flow plating at 3 mL/min for 10 minutes (CF-3-10), respectively. Each temporally discrete measure of transmission was obtained from a real-time spectra from 330 to 750 nm obtained *in situ*. For both CF-3-10 and BI-10, Ag was deposited for 2 min onto Sn-sensitized silicate glass (during which spectra not shown were obtained at 30-sec intervals) and washed for 5 min with H_2O before initiating EL Au deposition at time 0 sec. BI-10 plating was performed in the same system as CF-3-10 by displacing the entire system volume of 0.5 mL in 1 sec with Au plating solution. Each kinetic profile consists of the period of 30 sec H_2O washing before Au solution injection, consecutive 600 sec Au deposition and subsequent 100 sec H_2O washing and incubation for 100 sec. Particularly, the observed longer profile of CF-3-10 than BI-10 is due to lateral diffusion of Au (I) ions and

114

HCHO ions in continuous flow during a lag time. There was a volumetric holdup of ~72 μL in the injection system between glass syringes containing Au solution and the spectroscopic flow cell. At 3 mL/hr flowrate, this resulted in a theoretical lag of ~87 seconds.

SEM images in Figure 4.4.3 show representative morphologies of CF-EL thin metal films corresponding to time regimes of EL deposition at -10 sec (I), 27 sec (II) and 670 sec (III), respectively, or in other words 10 sec before Au deposition began, 27 sec after Au deposition began, and 70 sec after Au deposition ended. Representative images I and II are 2 min Ag activated film and HCHO driven Ag NP which were produced in separate Ag activation and post HCHO exposure experiments with the same hydraulic conditions. Image III is a 10 min EL Au deposited film. Figure 4.4.3 inset contains representative spectra for CF-3-10 at time points indicated by arrowheads on the profile in the main figure. The dot and solid lines in the inset indicate 425 nm (Ag LSPR feature point) and 495 nm (Au PL feature point) wavelengths, respectively. At time point I (-10 sec) in the CF-3-10 profile, transmission at 495 nm is ~90 %. This point corresponds to the inset transmission spectra at -10 and 0 sec (black) which exhibits a broad valley with a minimum at ~495 nm, attributable to deposition of thin metallic Ag island film which shows a broad absorption peak at ~500-520 nm.[3] At time point II in the CF-3-10 profile, transmission at 495 nm is ~69%. This point corresponds to the inset transmission spectra at 27 sec (pink), attributable to reduction of Ag thin film to Ag NP resulting from 2.7× faster diffusive flux of methylene glycol (hydrated HCHO) to the Ag surface, relative to the diffusion of Au(I) sulfite complex. Formaldehyde (HCHO), an electron donor for EL Au plating, reduces Au(I) to Au(0) and Ag(I) to Ag(0).[1,4] Active Ag ions remaining at the Ag island surface reduce Ag(0) and lead to self-assembled Ag NPs via concomitant reduction from Sn(IV) to Sn(II) at the
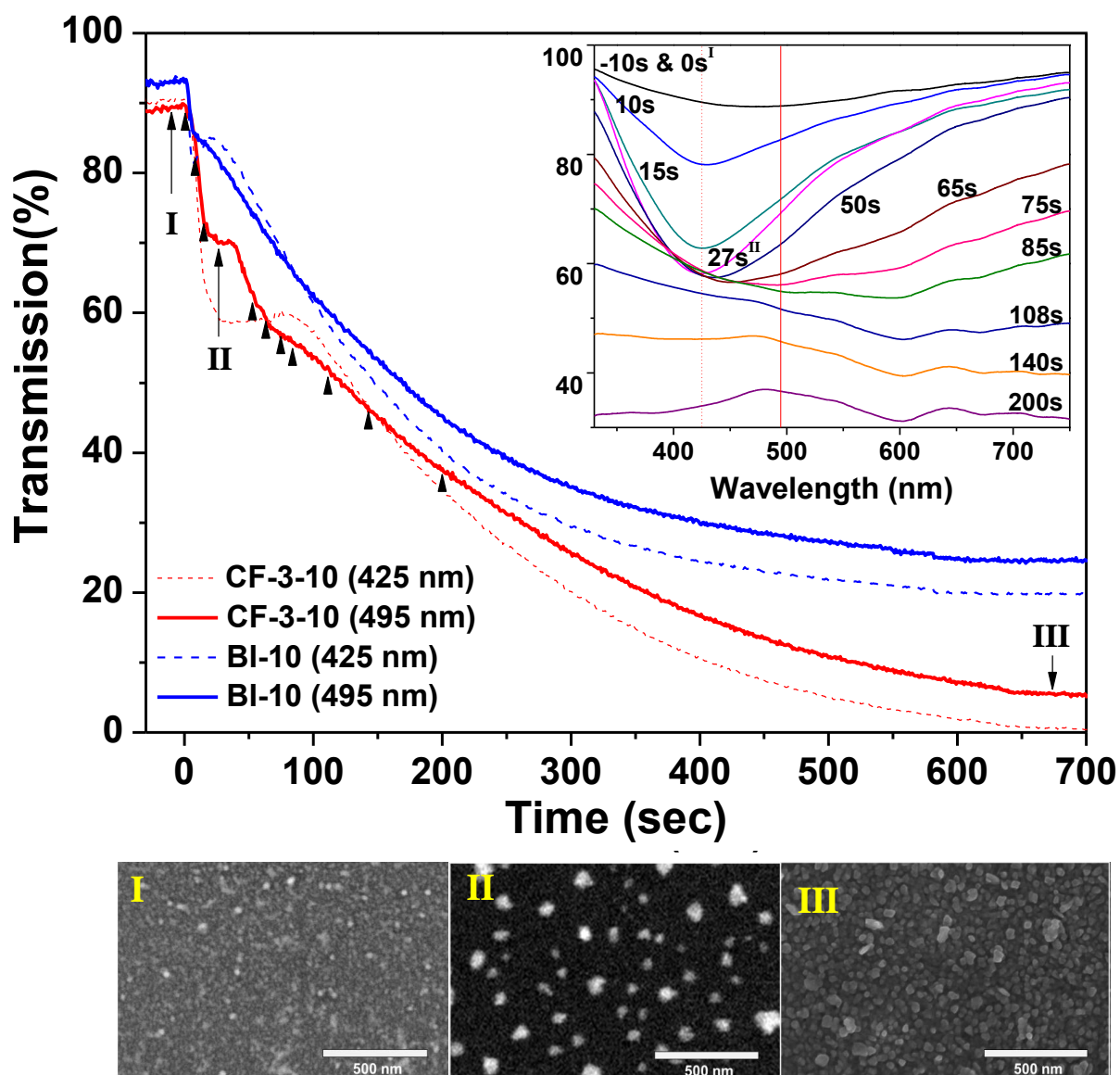
Figure 4.4.3. Kinetic profiles of real-time Ag LSPR and Au PL transmission feature at 425 and 495 nm for CF and BI-EL Au deposition. Inset are transmission CF-EL spectra taken at times indicated by the black arrows in the main figure. Dotted and solid lines in the inset identify 425 nm and 495 nm wavelengths from which profiles in the main figure were derived. SEM images show representative EL metal film morphologies during three steps in EL Au plating: I. Ag cluster deposited film (-10 sec); II. HCHO-driven Ag NP formation (27 sec); III. EL Au deposited film (670 sec))

116

interface between Ag and Sn(IV) wetted substrates.[4] The mass transfer rate calculated by eqn (5) for these hydraulic conditions for methylene glycol ($\sim$6.2$\times$10^{-4} cm^2/s) is 2- fold faster than Au(I) sulfite complex ($\sim$3.2$\times$10^{-4} cm^2/s). At time point III (670 sec), transmission at 495 nm is $\sim$5%. The corresponding transmission spectra exhibit a peak at $\sim$495 nm, similar to the feature observed at 200 sec. Continuous Au films have a characteristic photoluminescence (PL) transmission peak near 500 nm.[1,6]

Analysis of characteristic profile features such as slope fluctuations allows the time-scales of discrete EL film growth regimes to be identified and quantified. Similar kinetic profile trends, as shown in Figure 4.4.3, are observed during initial EL plating period (0$\sim$100 sec) for both CF-3-10 and BI-10. For CF-3-10, this period is characterized by a rapid decrease in transmission profiles at 495 nm (0$\sim$15 sec), followed by a steady decrease (16$\sim$36 sec), and finally another deep decrease of profiles (36$\sim$100sec). The transmission profile at 425 nm also shows three fluctuations such as a rapid drop (0$\sim$27 sec), a steady increase (28$\sim$84 sec), and a final decrease (85$\sim$100 sec). Similar fluctuation patterns are observed in the BI-10 transmission profile. The profile at 495 nm (blue) exhibits a rapid drop (0$\sim$5 sec), a steady decrease (6$\sim$20 sec) and another deep drop (21$\sim$100sec). For the profile at 425 nm, BI-10 also follows the trends of CF-3-10 which are characterized by drop, increase and another decrease during initial 100 sec deposition. These three distinctive fluctuations are indicative of three successive EL Au film formation regimes: HCHO driven Ag NP aggregation, Ag and Au alloy formation via galvanic displacement of Ag by Au and autocatalytic Au film growth.

For CF-3-10, the kinetic transmission profiles at 425 nm and at 495 nm include Ag and Ag-Au alloy LSPR feature for 0 to 85 sec and Au PL feature after 85 sec. The transmission

profile at 425 nm decreases more rapidly than the transmission profile at 495 nm for 0 to 27 sec, the first regime, because of the appearance of an Ag LSPR absorption peak induced by Ag NP formation via HCHO reduction, as shown in Figure 4.4.3 SEM image II. Figure 4.4.3 inset shows the transmission spectra rapidly changed from an Ag film feature with a broad valley at circa 500 nm at 0 sec to an LSPR absorption feature of Ag NPs with a narrower, more intense valley at 425 nm at ~27 sec. During the second regime, between 28 sec and 85 sec, the transmission profile at 425 nm slowly increases and the transmission profile at 495 nm decreases with different slopes. The corresponding inset transmission spectra at 50 sec, 65 sec, and 75 sec indicates a redshift in the Ag LSPR absorption valley to 507 nm with broadening. This redshift and broadening of the Ag plasmon feature are attributed to Ag-Au alloy formation during galvanic displacement of Ag by Au.[7] Clear indications of galvanic displacement termination is accompanied by a simultaneous rise in the Au PL peak at ~480 nm, as shown in the inset transmission at 85 sec. After this point, the transmission profile at 495 nm is indicative of a characteristic Au PL feature. The third regime, autocatalytic Au film growth, began with a smooth transmission profile decrease. The Au PL feature became distinguishable at a wavelength of ~480 nm and the overall valley feature dramatically transformed to peak feature at 108 sec. From this time, growth of the Au island film structure eventually results in island coalescence which creates a continuous path for electrons throughout the Au network, resulting in significant changes in the optical and electrical film properties.[8] Further increases in deposition time resulted in a redshift of the Au PL peak to 495 nm with an increasing peak height, which is consistent with growth of an Au island film structure.[6] At 108 sec, a peak appeared at 650 nm which has been attributed to surface plasmon polaritions (SPPs) due to increased film thickness up to 50 nm.

The kinetic profiles of BI-10 exhibit similar trends to those of CF-3-10, albeit within a shorter time period for the first (0-5 sec) and second (6-20 sec) regimes, suggesting the deposition mechanism is the same for both EL plating methods. The shorter time regime in BI-10 is due to instant solution injection prior to 10 min incubation. Instant injection induces a brief CF effect, which leads to a faster initial mass transfer rate of HCHO and Au complex ions than for constant injection flow in CF-3-10. This results in faster HCHO-driven Ag NP formation and successive galvanic displacement of Ag by Au.

Different hydraulic conditions affect initiation of EL deposition. Differences in the diffusion rate between CF and BI-EL samples affect the rates of reaction throughout the plating process. The shorter initial fluctuation period of BI-10 relative to CF-3-10 may be due to less activated Ag amount, which can be inferred by higher transmission value at 0 sec in Figure 4.4.3 for BI-10, and faster mass transfer rate during the initial instantaneous Au solution injection in 1 sec. Figure 4.4.4 compares three different kinetic profiles of Ag LSPR transmission at 425 nm, CF-3-HCHO (square), CF-3-HCHO+Au (CF-3-10, circle) and BI-HCHO+Au (BI-10, triangle) to characterize hydraulic and chemical components effect during the early stages of EL deposition. For the CF-3-HCHO profile, HCHO treatment of a Ag activated substrate with a flow rate of 3 ml/hr for 5 min, shows three distinctive regimes which may be ascribed to Ag NP aggregation, Ag NP ripening and photosensitive Ag NPs erosion. The profile was captured between 0 and 80 sec for clarity. In complete dark treatment, the transmission reduced to 60 % after 5 min HCHO treatment. Light sensitive Ag ions are photochemically reduced to metallic Ag clusters in the presence of trace halides with UV exposure. UV exposure in wideband spectra light induces reduction of light sensitive Ag ion in bulk solution, which interferes with aggregation into larger particles on the surface. Therefore, the transmissivity of CF-3-HCHO recovered due to removal
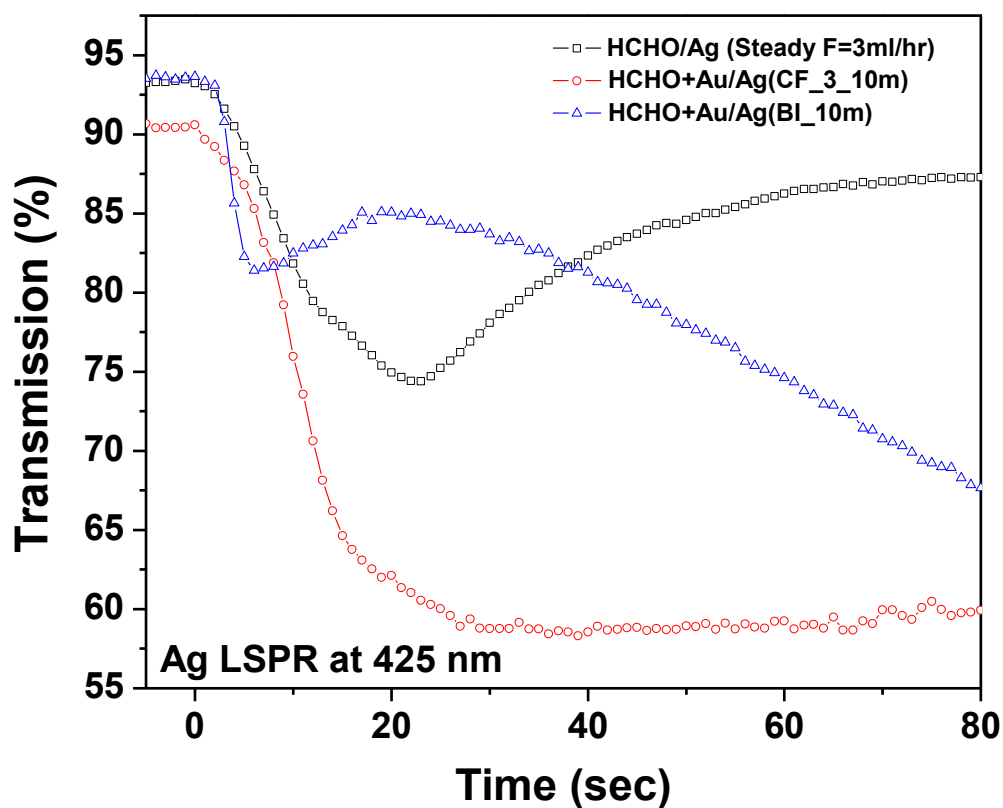
	Ag NP aggregation	Ag NP ripening	Photosensitive displacement	Galvanic replacement
HCHO/Ag (steady, 3ml/hr)	**-1.24** (R^2=0.98) **[0-12s]**	**-0.48** (R^2=0.97) **[13-23s]**	**0.39** (R^2=0.97) **[24-50s]**	**--**
HCHO+Au/Ag (steady, CF-3-10)	**-1.85** (R^2=0.95) **[0-15s]**	**-0.43** (R^2=0.98) **[16-27s]**	**0.02** (R^2=0.52) **[28-80s]**	
HCHO+Au/Ag (Unsteady, BI-10)	**-2.78** (R^2=0.94) **[0-6s]**	**--**	**0.31**(R^2=0.96) **[7-20s]**	**-0.31** (R^2=0.99) **[21-80s]**

Figure 4.4.4. Optical characterization of heterogeneous physicochemical reactions during initial EL Au deposition with varying diffusion conditions. The initial reaction may be categorized to Ag NP aggregation, Ag NP ripening, photosensitive displacement of Ag NP and galvanic replacement of Ag by Au.

of aggregated larger Ag NPs via UV-exposure and concomitant washing flow and leaving behind smaller particles associated to the surface. The CF-3-HCHO+Au profile exhibits similar trends to CF-3-HCHO with analogous slopes during the first two regimes. For the CF-3-HCHO+Au system, the reductant, HCHO, may contact reduced Ag film in advance of Au(I) complex ion due to the lower mass transfer rate of the latter ion through a stagnant boundary layer of H_2O. From calculated diluted HCHO and Au(I) complex diffusivity, the theoretical mass transfer rate of $CH_2(OH)_2$, a hydration form of HCHO (6.2×10^{-4} cm/s), is ~2 times higher than Au(I) complex (3.2×10^{-4} cm/s) in the CF-3-HCHO+Au system. During the fast Ag aggregation regime via fast HCHO contact, the slope of CF-3-HCHO+Au (-1.24 %/sec) is similar to that of CF-3-HCHO deposition (-1.85 %/sec). For the ripening of Ag NP regime, the slope of CF-3-HCHO+Au (-0.48 %/sec) is again comparable to the slope of CF-3-HCHO (-0.43 %/sec). The increased duration of the second regime for CF-3-HCHO+Au is due to an increased amount of activated Ag than the CF-3-HCHO sample. After the second regime, the successive Au(I) complex ions contact the Ag activated surface and initiated galvanic displacement of Ag by Au. The Ag and Au alloy formation results in a stable transmissivity for 60 sec.

However, the profile of BI-HCHO+Au, which is governed by unsteady state diffusion, exhibits a sharper drop and faster upshift of transmission relative to CF-3-HCHO+Au and CF-3-HCHO without a Ag NP ripening regime. The slope of Ag aggregation in BI-10 is -2.78 %/sec, which is ~1.5 times lower than CF-3-10. This is due to a faster mass transfer rate of HCHO induced by the near-instantaneous injection (~1 sec). For hydraulic condition of unsteady state diffusion for desired 10 min deposition, the 0.5 ml total mixture of Au solution and reducing agent was first injected into the flow cell for 1-sec and then incubated for 10 min. Due to rapid injection, the BI-EL mass transfer model needs to be modified to consider the instantaneous CF

effect at the early stage of EL deposition. In CF-EL deposition, as flowrate increases, the continuous laminar or turbulent bulk flow decreases the stagnant boundary layer adjacent to the wall, resulting in an increased mass transfer rate. In principle, the instantaneous injection (F=0.5 ml/sec) at the beginning of BI-EL deposition induces an initially thinner stagnant boundary layer relative to CF-3-HCHO+Au (F=8.3× 10^{-4} ml/sec). This thinner boundary layer of BI-HCHO+Au, results in faster initial diffusion of the HCHO and Au(I) complex ions than for the CF-3-HCHO+Au condition. The mass transfer coefficients of Au(I) and HCHO for instantaneous injection are $2.7×10^{-3}$ cm/sec and $5.3×10^{-3}$ cm/sec, which are ~8.5 times faster than in CF-3-HCHO+Au deposition ($3.2×10^{-4}$ cm/sec and $6.2×10^{-4}$ cm/sec). The instantaneous injection of Au(I) thus resulted in a galvanic displacement of Ag by Au earlier than that observed in CF-3-HCHO+Au. The instantaneous injection may also displace some weakly bound Ag NPs and unbounded reduced Ag resting on the surface.

Overall kinetic profile of CF-EL exhibits steady state deposition. The overall kinetic Au plasmon transmission profile in Figure 4.4.3, supports that the mass transfer rate of CF-EL deposition is consistently higher than BI-EL. BI-EL Au mass transfer is a time dependent diffusion model, because of species depletion over time. In principle, BI-EL deposition rate decreases exponentially as deposition time increases (see finite and semi-infinite BI profile in Figure 4.4.2(B)). The kinetic transmission profile at 425 nm and 495 nm of BI-10 clearly exhibit non-linear regressions corresponding with the BI mass transfer models. For the transmission profile at 425 nm, linear regression yields a decreasing slope between 6 and 606 sec of -0.105 %/sec (R^2 = 0.827). The first Ag LSPR feature regime (0~5 sec), specifically HCHO driven Ag NP formation region, was excluded from the regression. The second regime (6~20 sec), Ag and Au alloy regime via galvanic displacement, was included in the regression because

of Au involvement. The linear slope between 6 and 606 sec in transmission profile at 495 nm was assigned to a Au PL feature profile which exhibits a similar value of -0.094 (R^2 = 0.851). However, the kinetic profile of CF-3-10 is different from that of BI-10. The mass transfer rate for CF-EL Au deposition is steadily higher than BI-EL deposition due to adjacent, continuous laminar flow for 600 sec. This flow decreases the stagnant boundary layer thickness adjacent to the wall and provides a time-invariant Au concentration. Theoretically, the total deposited amount of Au ions is linearly increasing during Au deposition due to constant deposition rate (see the red line and dot in Figure 4.4.2(B)). The kinetic profiles of CF-3-10 at 425 nm and 495 nm (Au PL) exhibit a more linear nature than BI-10 resulting in 425 nm transmission profile slope of -0.122 (R^2=0.919) and an Au PL profile slope of -0.112 (R^2=0.922) between 26 and 626 sec. Similar to the BI samples, the HCHO driven Ag formation (0~25 sec) was excluded from the regression while the Ag and Au alloy regime (26~85 sec) was included These more linear and steeper slopes for CF-3-10 profiles appear to correlate with the proposed mass transfer model for CF-EL systems.

The nonlinearity of CF-EL profile in the latter time zone (~350-626 sec) relative to the early time zone (26-350 sec) may be due to thickness and surface roughness dependent Au PL enhancement feature. PL intensity at ~500 nm increases in "very thin" (6.6, 9.9 and 19.5 nm) Au sputtered films with increasing thickness.[9] Moreover, as the Au film surface roughness increases, the PL peak height increases. In our system, an increase in roughness of CF-EL Au film was observed with increased thickness at longer times in Figure 2(B); however, PL enhancement is a thickness limited feature. In separate work, the PL also linearly increased with increasing thickness in films ≤ 70 nm, but exhibited saturation at 90 nm on glass substrates.[10] For thicker Au film, PL intensity of a 130 nm thick-film decreased ~3-fold when compared with a 60 nm

thick-film.[11] In the system discussed herein, deposition times above 350 sec increase the thickness of EL film $> \sim 60$ nm (Figure 4.4.2 (B)). The nonlinearity of transmission profile in the latter time zone may correlate with the variation of PL enhancement feature above a certain limited thickness (~60 nm). The PL enhancement resulting from surface roughness may be offset by an increase in thickness. Other possible interpretations include the transition of deposition kinetics from galvanic displacement to autocatalytic deposition as well as concomitant decrease of effective catalytic site area for autocatalytic reduction with increasing thickness. For EL Au plating via galvanic replacement, once the substrate surface is covered with deposited film, the galvanic displacement is halted and the continuation of film growth relies on autocatalytic process. The autocatalytic plating is a deposition of a metallic coating by controlled chemical reduction which is catalyzed by the metal being deposited.[4] For this system, the galvanic displaced Au nucleation site plays a role of catalyst for HCHO driven Au reduction.[4] The effective surface area (ratio of surface area to volume) of EL Au thin film decreases with film growth from discrete nucleation, through discontinuous islands, to continuous films. This kinetics transition combined with a simultaneous decrease of effective catalytic surface area may be responsible for the non-linearity observed at longer deposition times.

The linearity of transmission profile is related with the linearity of PL intensity profile. Figure 4.4.5 exhibits a comparison of kinetic transmission profiles at 495 nm (upper) and PL intensity profiles (lower) with increasing flowrates. The PL intensity profile is calculated as the transmission difference between 495 nm and 330 nm during EL deposition. Figure 4.4.6 (A-D) are time resolved transmission spectra of CF_w-2-10, CF_w-3-10, CF_w-4-10 and CF_w-5-10. In order to compare EL Au deposition profiles, the onset of EL Au plating for each profile was adjusted to a value of 100% transmission. In this experiment, Sn sensitization time was reduced to 5 min
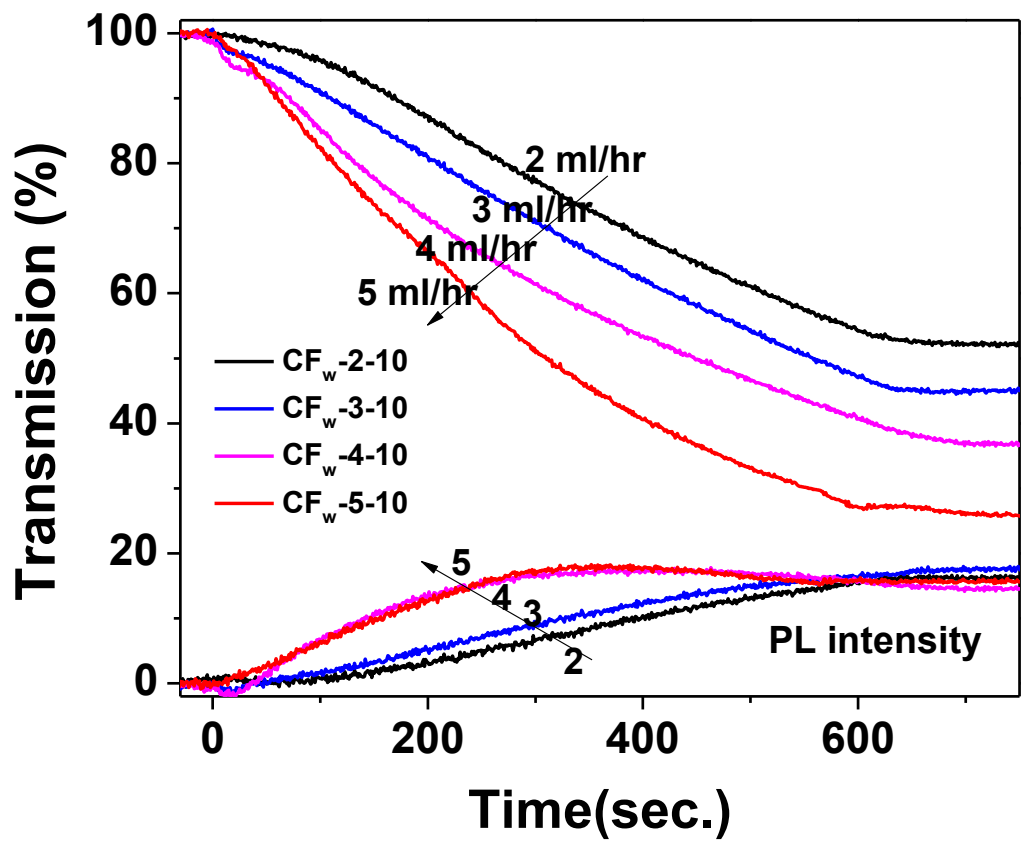
Figure 4.4.5 Comparison of CF_w-EL transmission kinetic profiles at 495 nm (upper) and PL transmission difference profile (lower) relative to transmission at 330 nm with increasing flowrate.

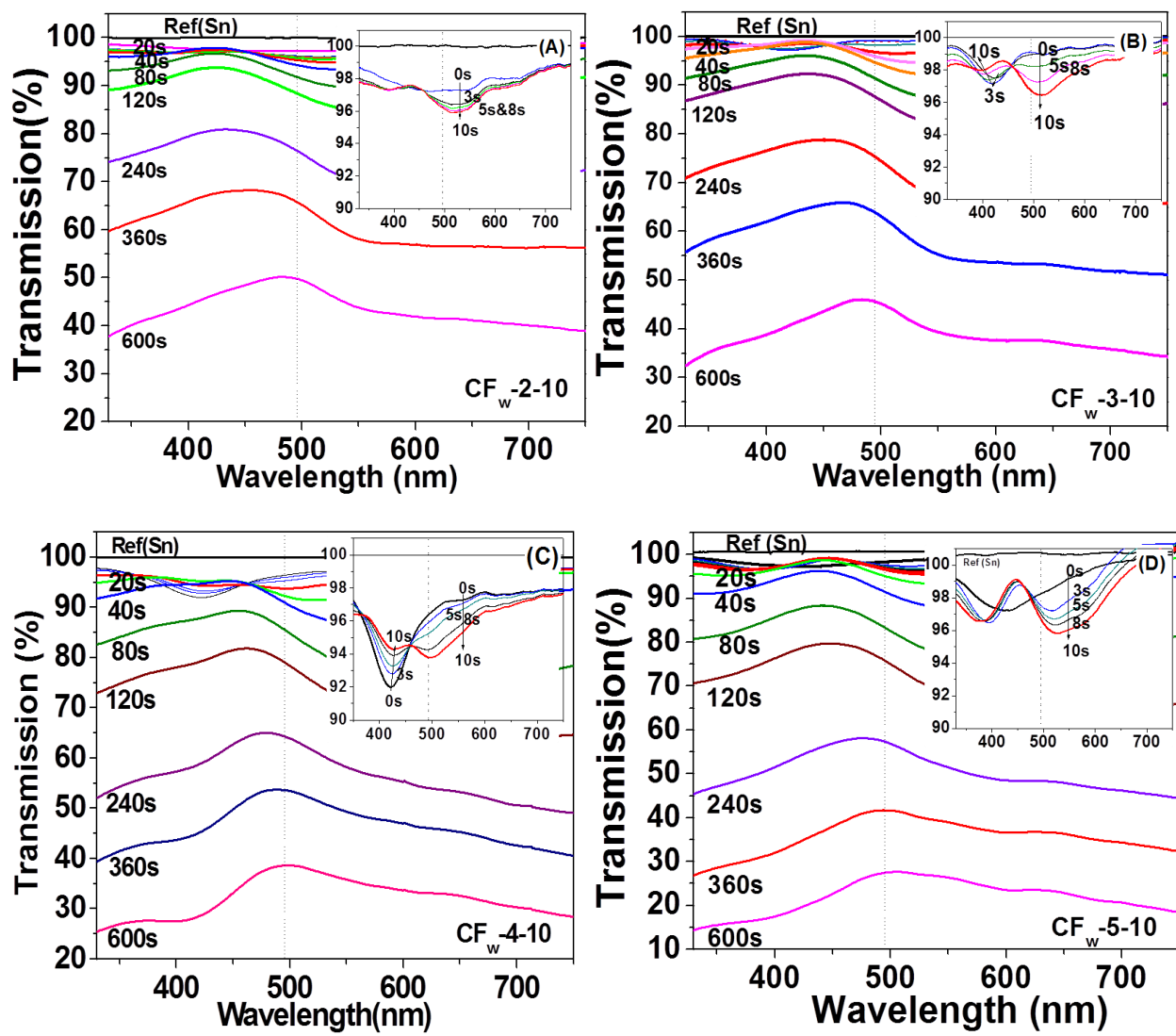**Figure 4.4.6** Time resolved transmission spectra during an entire plating of (A) CF$_w$-2-10, (B) CF$_w$-3-10, (C) CF$_w$-4-10 and (D) CF$_w$-5-10. Dotted lines indicate 495 nm position used for calculations. Inset is a close-up spectra between 0 s and 10 s.

to minimize heterogeneous Ag morphology formation such as black aggregated particles and their dark spots, during Ag activation which may contribute to longer Ag related regimes, Ag NP formation and Ag–Au alloy formation, in CF-3-10. Interestingly, the time period of convoluted Ag related regimes (Ag NP and successive Ag-Au alloy formation), as shown in Figure 4.4.6 (A-D), are shortened by ~10 sec. For instance, for CF_w-3-10, Ag LSPR appears to be enhanced via HCHO driven Ag NP formation at ~3 sec and the Ag LSPR intensity decreased with blue shifting and concomitant Au PL feature near ~457 nm arose at 8 sec. The Au PL peak intensity (~0.7%) exceeded the Ag LSPR (~0.6%) at 8 sec. For CF_w-4-10, the Ag activation formed Ag nucleated particles with a peak at ~421 nm on Sn substrate and then Ag-Au alloy formed as soon as Au solution contacted. The Ag-Au alloy peak red-shifted to ~429 nm with decreasing peak intensity for 10 sec. The Au PL peak arose at ~460 nm with intensity of 0.7% at 8 sec. All transmission spectra exhibit clear Au PL features near 460 nm at 10 sec (in inset) which red-shifts with further deposition. Figure 4.4.5 shows low flow rate samples, CF_w-2-10 and CF_w-3-10, exhibit better linearity for the overall profile during Au deposition relative to CF-3-10 in Figure 4.4.3. For CF_w-2-10 and CF_w-3-10, these Au PL profiles linearly decreased between 10 sec and 610 sec at a rate of -0.084 %/sec (R^2=0.995) and -0.090 %/sec (R^2=0.997) and then stabilized to transmissivity values of ~52.2% and 45.3 %, respectively, as Au deposition completed. However, the profiles of CF_w-4-10 and CF_w-5-10, *i.e.* high flow rates samples, exhibit distinctively less linear regression for overall profiles than the low flow rates. For CF_w-4-10 and CF_w-5-10, these Au PL profiles decreased between 10 sec and 610 sec at a rate of -0.094 %/sec (R^2=0.973) and -0.121 %/sec (R^2=0.966) and then stabilized to transmissivity values of ~36.8% and 25.8 %, respectively. The decreased linearity, decrease of R^2 values, for the faster flow rate samples is attributed to the latter time zone (300~600 sec) where Au deposition produces a Au film more

than 50 nm thick. It is observed that the thicker film formation decreases PL intensity with increasing film thickness. PL intensity profiles, as shown at the bottom of Figure 4.4.5, exhibits that PL intensity of low flow rate samples steadily increases until completion of 10 min plating whereas PL intensity of these high flow rate samples more rapidly increase in the early time zone between ~50 and 300 sec and then saturate and slightly decreased in the latter time zone.

Interestingly, for high flow rate samples, the linear increase of PL intensity profile regime (50 sec~300 sec) corresponds to the regime of linear transmission profile at 495 nm; while the saturated PL intensity regime (300 sec~600 sec) corresponds to the non-linear regime. The time resolved transmission of CF_w-3-10 in Figure 4.4.6(B) shows that the PL maxima red-shifted to 490 nm for 600 sec. However, the PL maxima of CF_w-4-10 in Figure 4.4.6(C) red-shifted to 495 nm at 360 sec and appears to further red-shifted to ~500 nm at 600 sec. These optical features correspond to PL intensity saturation regimes in high flowrate samples. These kinetic features indicate that for high mass transfer rate samples, the deposition increases PL enlargement up to a certain limited thickness with a linear decrease of Au PL transmission, but further deposition over the limited thickness decreases PL intensity in a non-linear fashion. The better linearity of the transmission profile in the early time zone may represent the mass transfer feature during EL deposition. As flow rates increase from 2 to 3 to 4 to 5 mL/hr, the slopes of CF_w in the early time zone (50 sec~300 sec) are 0.089 (R^2=0.993), 0.099 (R^2=0.993), 0.127 (R^2=0.993) and 0.160 (R^2=0.993).

4.4.2.3. Optical correlations for prediction of EL Au deposition

Correlation of transmission profile and model predicted features. In a typical BI-EL metal deposition system, deposition rate kinetics are correlated with solution constituents, pH,

and mechanical operating condition.[12,13] The film growth rate limiting step in EL Au deposition is a complex interaction of mass transfer to the substrate and local reduction potential. For the system under consideration herein, dynamic optical feature variations during film growth depend on the amount of Au mass transferred to the substrate. Figure 4.4.7 and 4.4.8 show the correlation between mass transfer models and time-resolved optical features as a function of Reynolds number. The specific amount of Au deposition profile and mass transfer coefficient profile as a function of Reynolds number were predicted using a two compartment and rate model (red) and empirical film model (black). These profiles were evaluated for both narrow (CF: solid line) and wide (CF_w: dot line) flow channel geometries to consider scalable flow cell dimensions. The mass transfer coefficients and specific amounts of Au deposited calculated by the two compartment and effective rate model are slightly higher than those of the film model because effects due to the geometry of the rectangular flow cell are considered. The applied optical features for correlations in Figure 4.4.7 are a drop in transmissivity at 495 nm for CF-EL transmission profiles during 600 sec Au related deposition and a decreasing slope of dynamic transmission profile at 495 nm as in the range of 10-610 sec. In Figure 4.4.8, the optical features, a drop and a decreasing slope, are determined in the range of 50-300 sec.

Figure.4.4.7(A) exhibits the profile of the specific amount of Au ion deposited as a function of Reynolds number correlates with the Au PL transmission drop. The correlation also suggests that the dynamic transmission drop in the range of 40–80 % represents the specific amount of Au ion deposited in the range of $1.00–2.25 \times 10^{-4}$ g/cm^2 for 10 min deposition, which easily converts to film thickness, during plating. BI-10, as indicated in the Figure 4.4.7(A), theoretically deposits $\sim 1.00 \times 10^{-4}$ g/cm^2 of Au amount (~ 40 nm thick film) in our system.

Figure 4.4.7 Correlations between coefficients of mass transfer model and dynamic optical features as a function of Reynolds number: (A) Correlation between specific deposition amounts and Au PL transmission drop values during 10 min Au plating; (B) Correlation between mass transfer coefficients and slopes of Au PL profiles during 10 min Au plating.
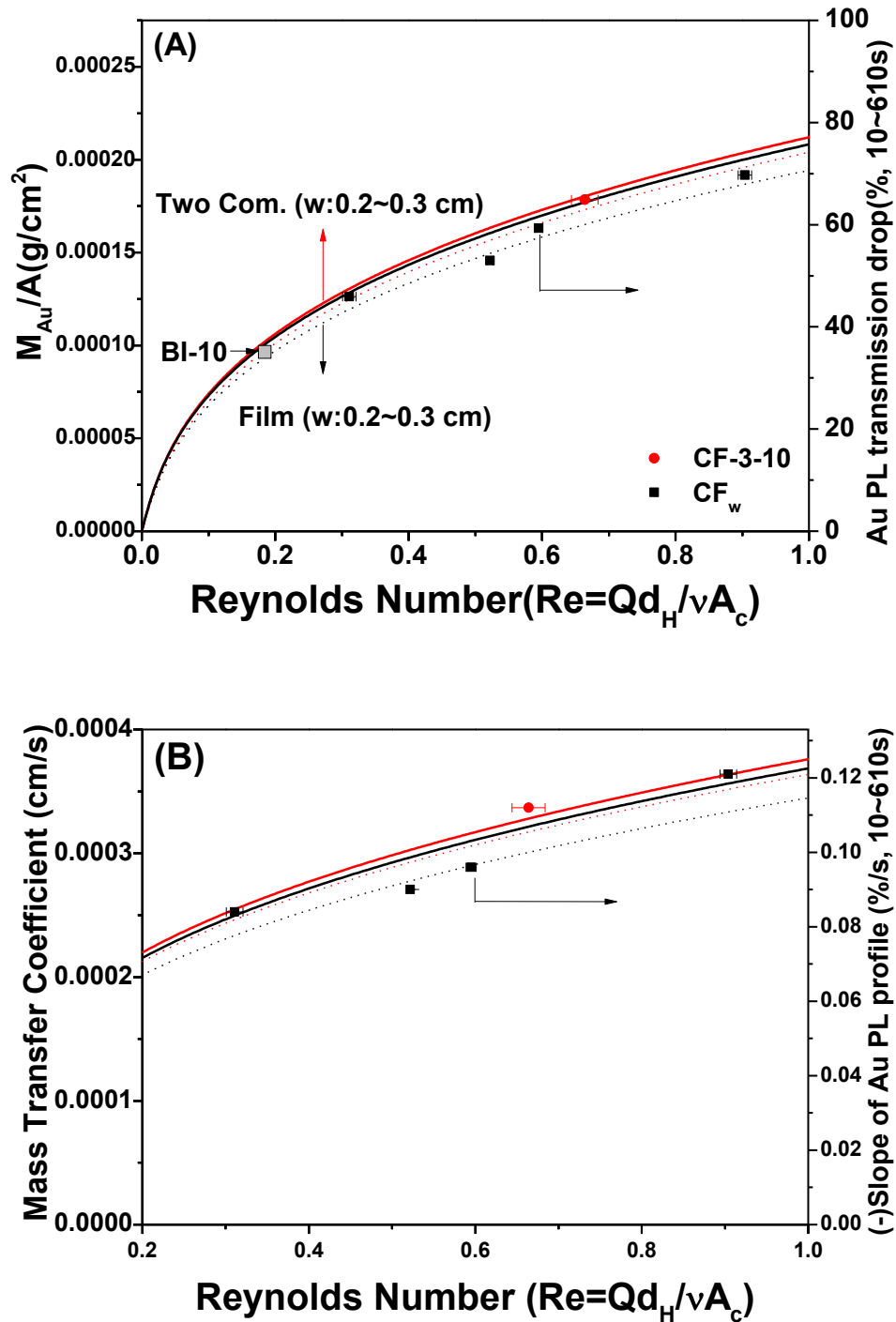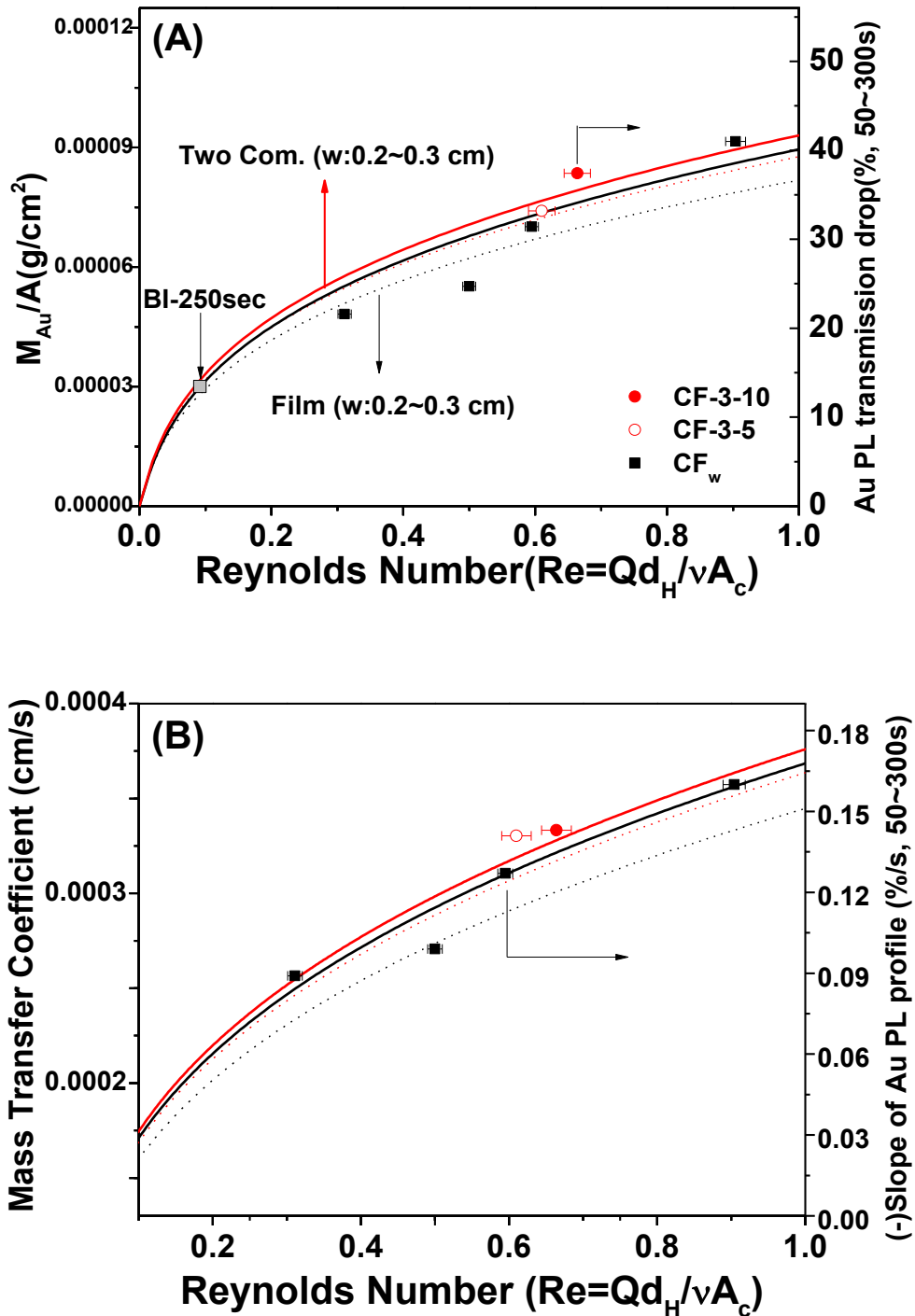
Figure 4.4.8 Correlations between coefficients of mass transfer model and dynamic optical features as a function of Reynolds number: (A) Correlation between specific deposition amounts and Au PL transmission drop values between 50 s and 300 s; (B) Correlation between mass transfer coefficients and slopes of Au PL profiles between 50 s and 300 s.

Based on these correlations and calculations, the rate of thickness growth during 10 min CF-EL deposition with increase of flow rate between 2 and 5 mL/hr are evaluated to ~6.0 – 10.5 nm/min. Both correlations indicate that the time-resolved optical features of CF-EL Au plating are dependent on Au ion mass transfer. The linear profiles represent the mass transfer of Au deposition. Figure 4.4.7(B) shows that the predicted mass transfer coefficients increase with increasing Reynolds number from 0.0 to 1.0. Interestingly, the correlation of negative slopes of Au PL profiles in the range of 0.00 – 0.13 %/s is well fitted for the profile of mass transfer coefficients in the range of 0.0 – 3.8×10^{-4} cm/s for both models.

Figure.4.4.8(A) exhibits the Au PL transmission drop in the specific range of 50 sec -300 sec, the early time zone, also represent the specific amount of Au ion deposition. The correlation also suggests that the dynamic transmission drop in the range of 0–40 % represents the specific amount of Au ion deposited in the range of 3.00–9.00×10^{-5} g/cm^2 for 250 sec deposition. BI-250 sec, as indicated in the Figure 4.4.8(A), theoretically deposits ~3.00×10^{-5} g/cm^2 of Au amount (~25 nm thick film) in our system. The linear profiles in the early time zone represent the mass transfer of Au deposition. Figure 4.4.8(B) shows that the predicted mass transfer coefficients increase with increasing Reynolds number from 0.1 to 1.0. The correlation of negative slopes of Au PL profiles in the range of 0.03 – 0.18 %/s is well fitted for the profile of mass transfer coefficients in the range of 1.0×10^{-4} – 3.7×10^{-4} cm/s for both models. This suggests that the negative slope of Au PL profiles can be used to accurately represent mass transfer coefficients in CF-EL deposition. The abscissa error-bars are due to variations in flow cell dimension.

Correlation of optical features with deposited mass and mass transfer rate as a function of Reynolds number provides a quick and facile means to confirm mass transfer rate and overall

deposited film thickness for scalable substrates. Quantifying mass transfer based on the Au PL profile slope allows for design and manufacture of EL metal deposition process equipment that can meet specified film requirements, in particular the final film thickness as a function of flow rate and substrate dimensions. The correlation between transmissivity profile drop and the amount of Au deposited suggests that real-time optical monitoring provides a fast, non-destructive means of characterizing the deposited mass of Au and film thickness.

4.4.3   Conclusion

The kinetic transmission profiles *in situ* measured by real-time T-UV spectroscopy allow quantification of complicated heterogeneous chemical reactions and physical transformations, including previously unrecognized time-dependent transitory regimes of EL Au plating. The time frames of these regimes, which affect the final thin film morphology, was controllable by controlling of hydraulic conditions. Moreover, the developed correlations between mass transfer models and the optical features of the kinetic profiles validate that growth of EL Au plating is mass transfer-limited deposition. The actual Au film thickness measured by SEM image analysis and XPS depth profiling corresponds to the predicted thickness via unsteady and steady diffusion rate models. Significantly, the developed mass transfer correlations provide design guides of CF-EL plating to control EL Au thin film growth ≤ 100 nm in scalable systems.

4.4.4. References

(1) Jang, G.G.; Roper, D. K. *J. Phys. Chem. C* **2009**, *113*, 19228-19236.

(2) Singer, R. R.; Leitner, A.; Aussenegg, F. R., J. Opt. Soc. Am. B, **1995**, *12*, 220-228.

(3) Baba, K.; Okuno, T.; Miyagi, M., Appl. Phys. Lett. **1993**, *62(5*), 437-439.

(4) Electroless Plating: Fundamentals and Applications, Mallory, G. O.; Hajdu, J. B. Eds.; American Electroplaters and Surface Finishers Society: Orlando, FL, 1990;

(5) Jang, G.G.; Roper, D.K. Anal. Chem. **2011**, *83*, 1836-1842.

(6) Ahn, W.; Taylor, B.; Dall'Asén, A. G.; Roper, D. K. Langmuir, **2008**, *24*, 4174-4184.

(7) Sancho-Parramon, J.; Janicki, V.; Loncaric, M.; Zorc, H.; Bubcek, P.; Bernstorff, S. *Appl. Phys. A* **2011**, *103*, 745-748.

(8) Kaiser, N. *Appl. Opt.*, **2002**, *41(16),* 3053-3060.

(9) Siegel, J.; Lyutakov, O.; Rybka, V.; Kolska, Z.; Svorcik, V. *Nano. Res. Lett*. **2011**, 6:96

(10) Serrano, A.; Rodriguez de la Fuente, O.; Garcia, M.A., *J. App. Phys*. **2010**, *108*, 074303

(11) Kim, J. H.; Moyer, P.J., *Opt. Exp.* **2006**, *14*, 6595-6603

(12) Ali, H.O.; Christie, I.R.A. *Gold Bull.* **1984**, *17(4),* 118-127

(13) Plana, D.; Campbell, A.I.; Patole, S.N.; Shul, G. ; Dryfe, R.A.W. *Langmuir*, **2010**, *26(12)*, 10334-10340.

CHAPTER 5

Concluding Remarks

In this work, I developed a novel CF-EL plating system that provides the advantages of EL plating, such as more uniform surface morphology, and overcomes the disadvantages by using a scalable, continuous process and controllable deposition rate. Throughout this work, modeling, fabrication and characterization of this novel CF-EL plating method were performed to achieve an ultimate purpose: developing a reliable, inexpensive wet chemical process for controlled metal thin film and nanostructure fabrication. Opto-physically uniform EL Au thin films and NPs were fabricated by this novel wet-chemical process. As a part of the project, a spectrophoto- metric method for quantitative analysis of metal ion was developed that improves the limit of detection relative to conventional instrumental analysis. A method to achieve the time-resolved optical profile of EL Au plating was devised and provided a new transitional EL Au film growth model which validated mass transfer model prediction of the deposited thickness of ≤100 nm thin films.

In Section 5.1 these important achievements are summarized according to the three research objectives presented in Chapter 1. Areas of future work for the development of more efficient scalable CF-EL plating and its application are suggested in Section 5.2

5.1 Summary

5.1.1 Modeling

Developed mass transfer models for EL plating predict metal ion deposition amounts. EL synthesis of metal films exposes a substrate to a series of solutions containing metal ions that may be covalently bound to the surface or to existing metals via redox reaction without

application of external electrical energy. EL plating rates are affected by the rate of reduction of the dissolved reducing agent and the dissolved metal ions which diffuse to the catalytic surface of the object being plated. In the scalable EL Au plating system, I found the EL plating, specifically Au, is a diffusion-limited deposition. Two categorized mass transfer models are suggested to describe conventional BI-EL plating and novel CF-EL plating. For BI-EL Au deposition, Au ions in a stagnant medium diffuse toward and deposit onto the substrate wall during incubation. Thus, the deposition rate model of BI-EL can be described as unsteady-state molecular diffusion, resulting from the depletion of species with respect to time in a unit volume through which the specie is diffusing. In CF-EL plating, these metal ion solutions are continuously injected into a confined rectangular substrate channel to produce a higher, time-invariant Au deposition rate via a higher, steady concentration driving force across a narrower stagnant boundary layer adjacent to the surface. Using models and mass balance correlations, the deposited thickness and metal ion concentration are predicted.

5.1.2 Fabrication

In the initial research phase, EL Au thin films and NPs were fabricated by a prototype CF-EL plating system which consists of an injection syringe, a flow pump, a micro needle, and an optical capillary as a target substrate. In particular, this forced-diffusion system allowed uniform coating on challenging structures such as nonconductive planar substrates, internal surfaces of micro-capillaries and three dimensional tips which are not possible via top-down sputtering and evaporation. The deposited thin films can be thermally transformed to hemi-spherical random Au NP arrays. In order to achieve continuous processing and *in-situ* characterization, the automated, scalable CF-EL plating system integrated with real-time T-UV spectroscopy was developed. This system is capable of depositing scalable thin films and

simultaneously probing the surface morphology and deposition. As an application of CF-EL plating for engineered nanostructures, ordered Au NP arrays with varying patterns and sizes were fabricated by EL plating on electron-beam lithographed ITO glass. Ordered nano-disk and spherical NP arrays were successfully fabricated.

5.1.3 Characterization

1) Opto-physical uniformity enhanced EL Au thin film

The uniform and continuous CF-EL Au thin films with improved physical and optical properties were examined by microscopic and spectroscopic measurements. CF-EL films deposited with different flow-rates were compared with BI-EL films fabricated by increasing immersion times. AFM analysis showed that the CF-EL films are more uniform than BI-EL films due to steady state diffusion. PL features revealed by T-UV spectra showed that CF-EL films are more opaque and less dispersive than BI-EL films in spite of shorter plating times. The extinction spectra of NP ensembles, transformed from CF films by successive heating, exhibit enhanced LSPR extinction peaks compared to BI-ELs. SEM image analysis of NP sizes and particle densities of the ensembles shows that CF-EL NP ensembles exhibit more monomodal particle size distribution, resulting in enhanced LSPR extinction spectra compared to BI-EL NP ensembles. A mathematical model for mass transfer in CF-EL plating shows steady state deposition driven by the higher transport driving force increases the total number of Au ions accumulated on the substrate, which correlates with improved film morphology and optical features including PL, SPR, and LSPR spectra.

2) Quantitative detection of Au(I) concentration for EL Au deposition

A novel direct spectrophotometric method was developed to quantitatively determine Au(I) concentration in acidic aqueous solutions by balancing redox activities of a strong reductant (HCHO) and a strong oxidant (NBS). The reductant and oxidant are added successively, in varying amounts, to a solution of Au(I), which is then exposed to an oxidizable color reagent (TMB). At low reductant levels, NBS oxidizes Au(I), which linearly suppresses subsequent oxidation of TMB by NBS to its distinctive blue charge-transfer complexes of diamine and diimine. At high initial HCHO reductant levels, Au(I) is reduced to Au(0), then subsequently oxidized to Au(III) by NBS. Upon addition of TMB, Au(III) is reduced to Au(0) accompanying oxidation of TMB to its spectrophotometrically detectable blue complexes, facilitated by the high HCHO level. This identifies levels of reductant, oxidant, and colorimetric agent and allows quantitative measurement of Au(I) to LOD of 0.0025 and 0.05 mgL^{-1} using low and high levels of reductant, respectively. Defining this straightforward spectroscopic method that uses commercially available redox reagents to measure Au(I) without surfactants or organic solvents permits rapid, accurate, and sensitive detection of Au ions for applications such as EL plating, catalysis, and *in vivo* therapies

3) Metal disposition and dynamics during EL metal thin film synthesis

Optical and physical transitional regimes throughout EL metal thin film growth at kinetic and equilibrium hydraulic conditions were evaluated *in situ* by real-time T-UV spectral measurement and time-resolved XPS depth profiling. Au and Ag thin films exhibit unique optical properties due to SPR which change with film morphology and refractive index. For example, T-UV spectra have shown PL of EL Au film which is directly correlated with thickness and surface morphology. These unique geometric and dielectric-dependent optical features allow

138

real-time T-UV spectral measurements to provide a fast, effective analytical method to evaluate surface morphology and chemistry during EL deposition of metal thin films. Specifically, the quantitative, real-time optical measurements first described distinguished four transitional physicochemical regimes during EL Au plating: self-limited Ag activation; Ag NP formation; Au-Ag alloy formation during galvanic replacement of Ag by Au; and uniform surface morphology formation during autocatalytic Au film growth. These kinetic features were correlated with time-resolved SEM microscopy and XPS depth profiling of the surface, internal and interface structure between metal films and silicate substrate.

4) Prediction of EL Au deposition on silicate surface at unsteady and steady conditions

The kinetic transmission profiles *in situ* measured by real-time T-UV spectroscopy allowed quantification of complicated heterogeneous chemical reactions and physical transformations including previously unrecognized time-dependent transitory regimes of EL Au plating. The time frames of these regimes, which affect on the final thin film morphology, were controllable by controlling of hydraulic conditions. Moreover, the developed correlations between mass transfer models and the optical features of the kinetic profiles validate that growth of EL Au plating is mass transfer-limited deposition. The actual Au film thickness measured by XPS depth profiling corresponds to the predicted thickness via unsteady and steady diffusion rate models. Significantly, the developed mass transfer correlations provide universal design guides of CF-EL plating for controllable scalable EL Au thin film with ≤ 100 nm thickness.

5.2 Future Work

(1) Further expand the application of the CF-EL plating to create challenging plasmonic designs: plating inside micro-size capillary for nano ring and uniform thin coating on nano tips, nano ring array using dewetting mechanism.

(2) Plans are underway to evaluate why Au(I), with a higher measured reduction potential than Au(III), appears unable to oxidize TMB in the absence of HCHO or NBS at the conditions studied. The extent to which such interferences impact use of this method for analyzing Au(I) as re-oxidized Au(III) is the subject of future work. Rigorous statistical validation of the method, including influence of foreign ions, interferences, matrix effects, sensitivity analysis, spike testing, and recovery testing is also the subject of future work. This would allow, for example, Au(I) determination in catalyst fabrication and EL Au plating and applications in cancer biology

(3) Apply our thin film and NP architectures to high throughput plasmonic devices such as optical antennae, biological sensors, plasmonic solar cells, surface enhanced Raman scattering (SERS) substrates, and near-field scanning optical microscopy based fabrication of nano-structures.

(4) Develop a scalable all-in-one CF-EL metal plating system combined with a metallic solution recycling system.